12-2013

Magneto-Optical Properties of Complex Oxides

Peng Chen
University of Tennessee - Knoxville, pchen@utk.edu

To the Graduate Council:

I am submitting herewith a dissertation written by Peng Chen entitled "Magneto-Optical Properties of Complex Oxides." I have examined the final electronic copy of this dissertation for form and content and recommend that it be accepted in partial fulfillment of the requirements for the degree of Doctor of Philosophy, with a major in Chemistry.

Janice L. Musfeldt, Major Professor

We have read this dissertation and recommend its acceptance:

Jon P. Camden, Adriana Moreo, Ziling Xue

Accepted for the Council:

Carolyn R. Hodges

Vice Provost and Dean of the Graduate School

(Original signatures are on file with official student records.)

Magneto-Optical Properties of Complex Oxides

A Dissertation Presented for the

Doctor of Philosophy

Degree

The University of Tennessee, Knoxville

Peng Chen

December 2013

Acknowledgments

First and foremost I wish to thank my advisor, Professor Janice L. Musfeldt, for her support, insight, guidance, and encouragement at all times. Thank you for introducing me to the wonderful world of spectroscopy. Your enthusiasm and drive is always an inspiration to me.

I am grateful to Professors Jon P. Camden, Adriana Moreo, and Ziling Xue for serving on my committee, as well as for all of their interest and help.

I wish to acknowledge all the members of our research group: Luciana Vergara, Xiaoshan Xu, Tatiana Brinzari, Jessica White, Qi Sun, Özge Günaydın-Şen, Brian Holinsworth, Ken O'Neal, Dipanjan Mazumdar, Michael Yokosuk, Henok Mikre, Lakenzie Crawford, and Joshua Bleu Wright for their help, encouragement, and collaboration. I am especially acknowledge Xiaoshan Xu for useful discussions and assistance. I am grateful to all the faculty and staff of the Chemistry Department who shared their knowledge with me and helped in variety of ways during my graduate program.

I would also like to thank Sang-Wook Cheong, Nara Lee, Stephen A. McGill, Christopher Koenigsmann, Alexander C. Santulli, Stanislaus S. Wong, Ramamoorthy Ramesh, Darrell G. Schlom, Nikolas J. Podraza, Venkatraman Gopalan, Robert J. Cava, Ya-Qi Wang, Bernd Lorenz, Gavin Lawes, Craig V. Topping, John Singleton, and Eun Sang Choi for the excellent collaboration during these years.

Finally, I thank my parents for always supporting and believing in me. Last but not least, I thank my wife and daughter for their support and encouragement throughout

my study.

Abstract

Complex oxides give rise to rich physics and exotic cross-coupled electronic and magnetic properties. This is because of the competing interaction between charge, structure, and magnetism in the materials. In this dissertation I present a spectroscopic investigation of several model complex oxides under external stimuli of magnetic field and temperature. The compounds of interest include $BiFeO_3$ [bismuth ferrite] nanoparticles and tetragonal film, $Bi_{1-x}Nd_xFeO_3$ [neodymium doped bismuth ferrite], α-Fe_2O_3 [hematite], $Ni_3V_2O_8$ [nickel vanadate], and $R In_{1-x}Mn_xO_3$ [manganese doped rare earth indium oxide]. These materials are attractive systems for investigating optical band gap tunability, lattice and charge dynamics, spin charge coupling, and magnetochromic effect. Systematic intensity and frequency trends in selected vibrational modes show that the paraelectric phase is Pm-$3m$ and the lowest frequency A_1 feature is the soft mode that drives the first order transition. Finite length scale effects are also evident in the electronic structure. It turns out that band gap red shifted $\sim$0.3 eV in the nanoscale particles and blue shifted $\sim$0.4 eV in the tetragonal film. With Nd^{3+} substitution, critical field of cycloid $\rightarrow$ homogenous (canted antiferromagnet) ordering transition decreases in $Bi_{1-x}Nd_xFeO_3$. Spiral magnetic order is quenched when $x\sim$0.2. Furthermore, we discovered that α-Fe_2O_3 appears more red in applied magnetic field, an effect that is amplified by the presence of the spin flop transition. Analysis of the exciton pattern reveals $C2$ monoclinic symmetry in the high field phase. Our measurements show field-induced blue shifts of the band gap in $Ni_3V_2O_8$ that are much

larger than those driven by temperature, anticipating a more greenish appearance in the fully polarized state. This change found to emanates from charge density differences around the Ni and O centers in high field. The result on $R\mathrm{In}_{1-x}\mathrm{Mn}_x\mathrm{O}_3$ shows a large magnetochromic effect in TbInO_3. The f electron excitations in DyInO_3 change dramatically in the field, a result from the Zeeman effect. When doped with Mn ions, magnetic response of the material is increased, and Mn d-d excitations emerge in the visible range. These findings advance our understanding of spin charge coupling and motivates fundamental research on other functional complex oxides under extreme conditions.

Table of Contents

List of Tables

List of Figures

Chapter 1

Introduction: Exotic Electronic and Magnetic Properties in Complex Oxides

Complex oxides have long been known as hosts for electronically and magnetically rich and useful properties including novel magnetism and emerging optical properties. It is because of the interactions between the metal and oxygen ions over multiple length, energy, and time scales. Even the simplest complex oxides exhibit a broad range of behaviors from insulating to metallic, showing phenomena such as ferroelectricity, magnetism, and superconductivity. The more complex ternary and higher-order oxides possess even more exotic properties such as multiferroic behavior, charge and spin frustration, colossal magnetoresistance, and high-temperature superconductivity (Fig. 1.1). Furthermore, combining the properties of different oxides into a system can create exciting multifunctional materials. [1–5]

The interplay between charge, structure, and magnetism is at the heart of this rich physics and chemistry. Competition in complex oxides includes spin-spin interac-

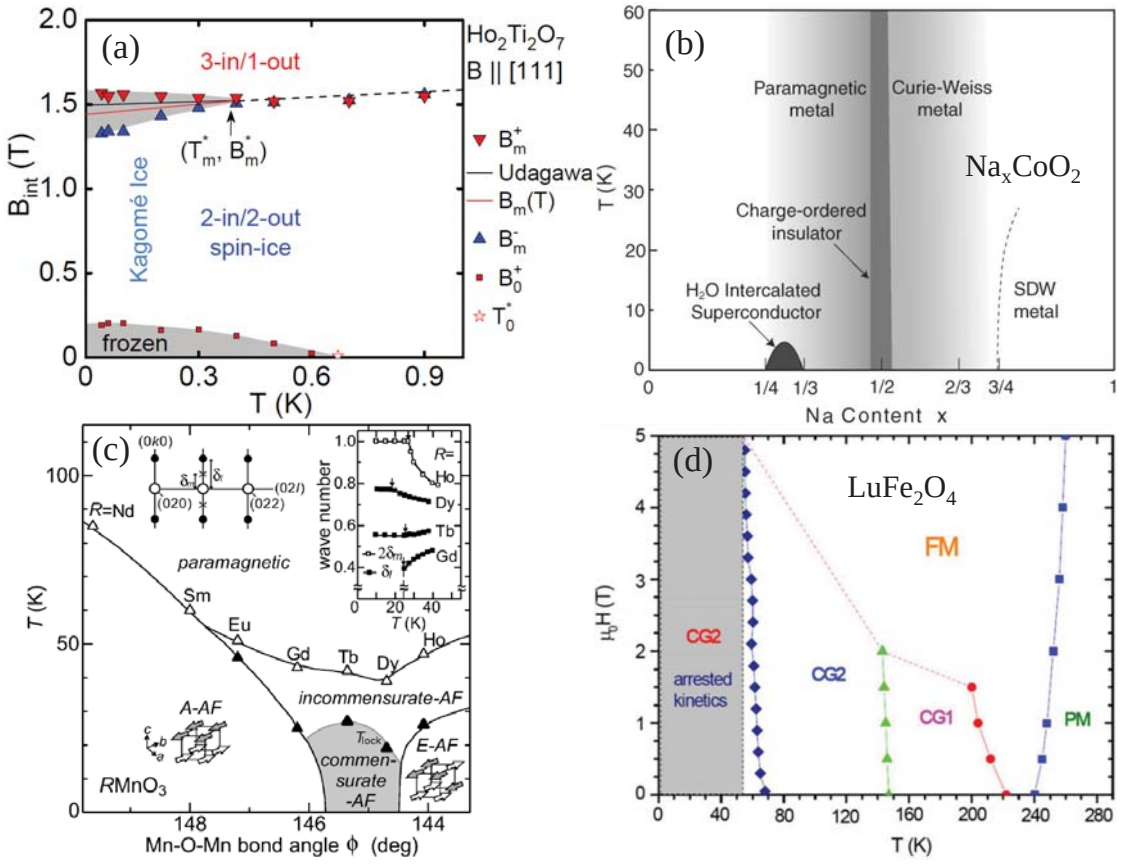

Figure 1.1: (a) Magnetic phase diagram of $Ho_2Ti_2O_7$ for magnetic field parallel to [111]. With respect to B = 0 strong freezing and hysteresis emerges in the magnetization below 0.67 K. At high fields a line of first order metamagnetic transitions terminates in a critical endpoint. The metamagnetic transition separates Kagom'e ice behaviour from a three-in/one-out configuration when going from below to above B_m. (after Ref. [1]) (b) The phase diagram of nonhydrated Na_xCoO_2. the charge-ordered insulating state at 1/2 is sandwiched between the paramagnetic metal at 0.3 and the Curie-Weiss metallic state at 0.65-0.75. The superconducting state is obtained on intercalation with H_2O. (after Ref. [2]) (c) Magnetic phase diagram for $RMnO_3$ as a function of Mn-O-Mn bond angle ϕ. Open and closed triangles denote the Neèl and lock-in transition temperatures, respectively. (after Ref. [3]) (d) A paramagnetic to ferrimagnetic (PM-FM) transition in $LuFe_2O_4$ at ∼240 K is followed by a re-entrant cluster glass transition (CG1 state) at ∼225 K and further by a second CG transition (CG2 state) below 170 K, partial kinetic arrest below 65 K and complete arrest below 55 K. (after Ref. [4])

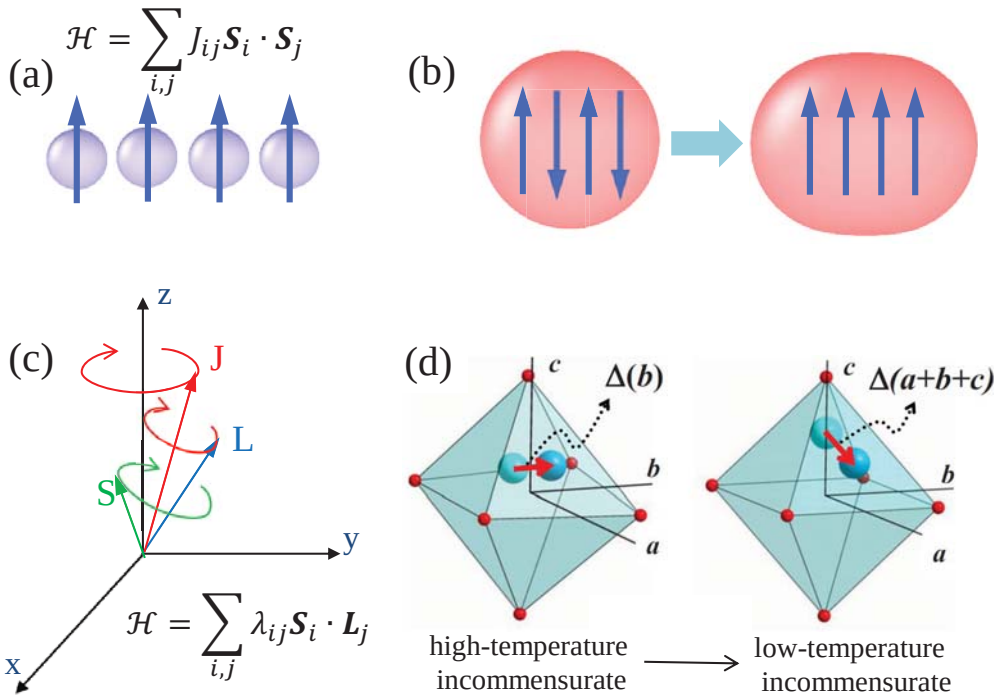

Figure 1.2: Schematic diagrams of (a) Spin-spin interaction, (b) spin-charge coupling-spin order change induced charge density change, (c) spin-orbit coupling, and (d) spin-lattice coupling and the change in local structure with spin orders (after Ref. [6]).

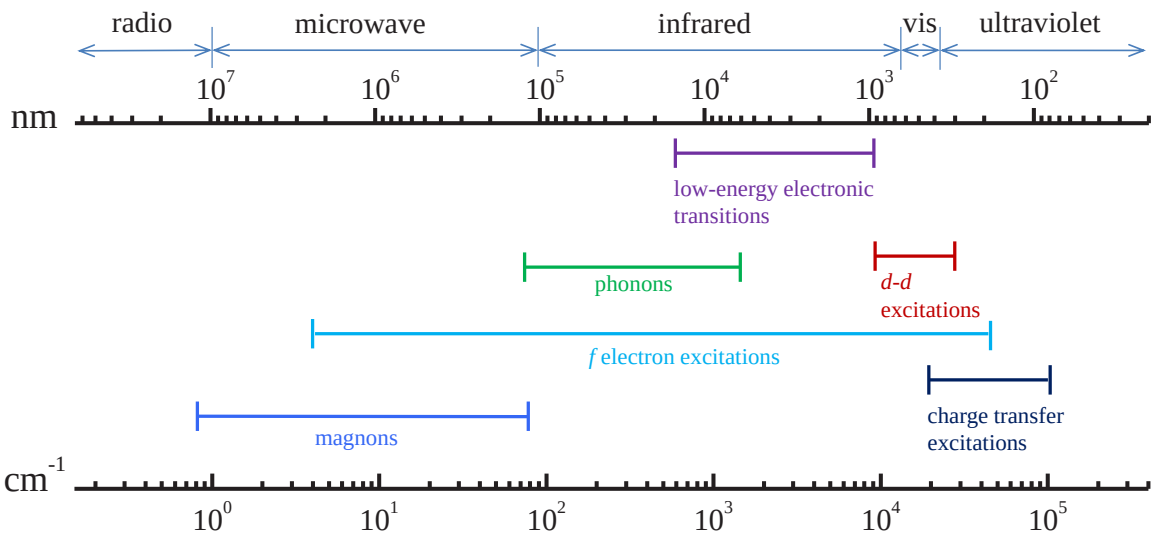

Figure 1.3: Typical energy ranges of various optically accessible excitations of complex oxides.

tion, spin-charge coupling, spin-orbit coupling, and spin-lattice interaction, as shown in Fig. 1.2. Probing and controlling these interactions is fundamental to the design of new functional materials and devices that emanate from this kind of research. Various responses of the materials are measured to reveal the mechanisms underlying the functionalities. Static properties like *dc* magnetization, resistivity, and Hall coefficient are measured to investigate spin-spin and spin-orbit couplings. Spectroscopy is widely used to investigate the various excitations (Fig. 1.3) as well as spin-charge, spin-orbit, and spin-lattice coupling effects. [6, 7] Understanding and controlling these interactions is critical to fabricate multifunctional complex oxides.

The electromagnetic radiation covers the wide regions from radio, microwave, infrared, visible, to ultraviolet with different photon energy, as shown in the Fig. 1.3. Optical spectroscopy is a local and microscopic probe of the nature of chemical bonding, hybridization, and among many other properties [8]. All the excitations studied by optical spectroscopies are dipole-allowed. In the low frequency range, infrared and Raman spectroscopies can be employed to detect magnetic excitations and vibrational

modes (phonons), which play a major role in thermal and electrical conductivities [7]. Combined with lattice dynamical calculations and group theory analysis, phonon behavior can be used to understand the local structure environment and symmetry. [9] Moreover, phonons can interact with charge and magnetic excitation to create defect states like a polaron or spin-phonon coupling. In multiferroics, the lattice dynamics are connected with ferroelectric order by a soft mode or modes, so direct measurement of phonon modes can reveal the displacive nature of ferroelectric phase transitions. [10]

In the higher frequency range, metal $d \rightarrow d$ on site and charge transfer excitations are evident in the absorption spectrum due to the hybridization of chemical bonding. Charge transfer excitations determine the band gap of the oxides, and they are the results from oxygen $2p$ to metal element $3d$ transitions. First-principles electronic structure calculations provide insight into the electronic structure like density of states, band gap of functional materials and can be used to compare with the optical results. [8, 14]Collective excitations like excitons, and magnon sidebands can be revealed by optical spectroscopy. They are induced by exchange coupling and very sensitive to variations in magnetic order, [11–13] making them sensitive probes of magnetic ordering transitions. [14]

To control the physical properties of a material, tuning techniques including temperature, pressure, finite size, and chemical substitution are broadly employed. [15–17] This is because the chemical bonding, charge, and magnetism are very sensitive to extreme conditions [14, 18]. Several examples of color properties tuning are displayed in Fig. 1.4, illustrating the color change with temperature [15], pressure [16] and chemical substitution [17], respectively. These changes are due to different mechanisms. For instance, with increasing temperature, the intensity of charge transfer excitation in yellow color range is reduced in 1,3-diamino-4,6- dinitrobenzene and causes the crystal to appear more yellowish in high temperature. [15] $BiFeO_3$ becomes black in high

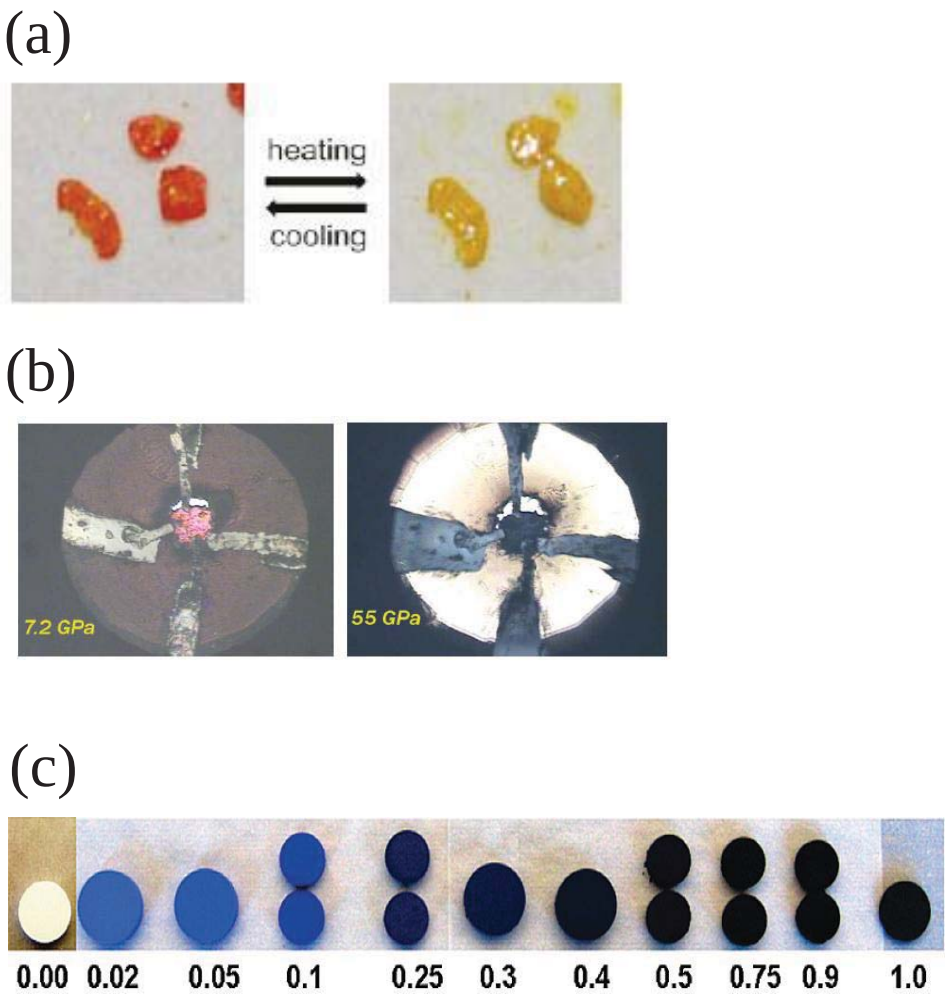

Figure 1.4: (a) Optical image of 1,3-diamino-4,6- dinitrobenzene showing the color change from orange to yellow when the temperature is increased from room temperature to 120°C. (after Ref. [15]) (b) In the image, $BiFeO_3$ sample becomes opaque because of the transition into the metallic state in the high pressure. (after Ref. [16]) (c) Colors of pellets and powders at selected compositions. With increasing Mn composition, the color darkens until eventually $YMnO_3$ is found to be black (after Ref. [17])

pressure because the band gap is closed above 50 GPa. [16] The color of $YIn_{1-x}Mn_xO_3$ gradually tunes from white, to blue, and finally to black with increasing Mn ion concentration. [17] Despite intensive study by traditional methods, there is less effort on how magnetic field induces optical properties changes, particularly those in visible range (380 – 760 nm). In this work, I focus on how magnetic field tunes the optical properties of complex oxides. I am especially interested in the color properties.

As already discussed, spin-lattice-charge coupling underpin much of the rich properties in multifunctional oxides. Magnetic field can change this coupling by driving into new phases with different magnetic order. For instance, the field-induced charge density distortion will modify the electronic structure and as a consequence, it induces band gap shift. The band gap is one of the most important electronic energy scales in a solid. It determines a variety of physical properties including *dc* resistivity, and it is vital to a number of applications like light harvesting. [19, 20] The band gaps of a Mott insulator and charge transfer type insulator are determined by *d*-*d* and charge-transfer excitations, respectively. The spin-charge coupling effect on these excitations will result in the band gap shift of oxides. [21, 22] Field can also cause an intensity change and peak position shift in collective excitations. When the excitations like *d*-*d* and charge transfer transitions emerge at visible range, the material will show a different color in the field and give rise to magnetochromic effect. [14, 23]

In this dissertation, I discuss the use of optical spectroscopy to investigate several model complex oxides under condition of high magnetic field and low temperature. Compounds of interest include $BiFeO_3$ nanoparticles and tetragonal film, $Bi_{1-x}Nd_xFeO_3$, α-Fe_2O_3, $Ni_3V_2O_8$, and $RIn_{1-x}Mn_xO_3$, where R is a rare earth center like Gd, Tb, and Dy. The scientific questions focus on lattice and charge dynamics and spin-charge interactions in these materials. We learned that key electronic energy scales like the charge gap can be tuned to a surprising extent with external stimuli. Our findings are

summarized in Table 1.1.

$BiFeO_3$ attracted our attention as a single phase room temperature multiferroic. Despite intensive study by traditional methods that employ temperature, applied pressure, or epitaxial strain to drive the paraelectric to ferroelectric transition, there was no consensus on the mechanism. We exploited the availability of different sizes of $BiFeO_3$ nanoparticles and employed infrared vibrational spectroscopy, group theory, and complementary lattice dynamics calculations to uncover the displacive nature of the ferroelectric transition. Intensity trends in selected phonon modes reveal that the paraelectric phase is cubic ($Pm\bar{3}m$), and A_1(TO1) mode softening with decreasing size points to a displacive mechanism.

The optical band gap of rhombohedral $BiFeO_3$ is 2.7 eV which is determined by the 3.2 eV charge transfer excitation. We pursued several band gap tuning strategies including using a new tetragonal phase stabilized by the compressive strain [24–26] and a set of $BiFeO_3$ nanoparticles. As a result, the band gap red shifted $\sim$0.3 eV in the nanoscale particles and blue shifted $\sim$0.4 eV in the tetragonal film. The familiar 3.2 and 4.5 eV electronic bands, assigned as minority channel dipole-allowed charge transfer excitations, [8, 27] split into multiplets in nanoparticles. These results can be understood as the strain-induced distortions of the local Fe^{3+} crystal field and shifts in the O $2p$ states.

Chemical substitution is an effective method for tailoring the physical properties of functional materials. We incorporate rare earth element Nd^{3+} into $BiFeO_3$ to achieve simultaneous ferroelectric and ferromagnetic ordering. With magnetic field-induced changes in the underlying magnon sideband as our probe of spin spiral behavior, we find that the critical field, which induced cycloidal spiral $\rightarrow$ antiferromagnetic phase transition, decreases with Nd^{3+} substitution, an effect that can be understood in terms of a larger anisotropy constant, longer spiral wavelength, and increased magnetic sus-

Table 1.1: Scientific problems and important findings in this dissertation

Model Compound	Scientific Problem	Our Findings
$BiFeO_3$ nanoparticles and tetragonal film	• Ferroelectric phase transition • Finite length scale effects on phonon modes • Optical band gap tuning with compressive strain and particle size	• The paraelectric phase in small size is $Pm\bar{3}m$ • Identify the soft mode that drives the first order ferroelectric transition • Blue-shifted band gap ($\sim$0.4 eV) in tetragonal film and red-shifted band gap ($\sim$0.3 eV) in nanoparticles compared with those of the rhombohedral film
$Bi_{1-x}Nd_xFeO_3$	• Chemical tuning • Spin cycloid order • Magnetic anisotropy	• Cycloid $\rightarrow$ homogenous ordering transition when $x\sim$0.2 • Critical field decreases with Nd^{3+} substitution • Magnetic anisotropy changes with chemical substitution and temperature
α-Fe_2O_3	• Magnetochromic effect • Exchange couplings in magnetic field • High field magnetic symmetry	• Hematite appears more red in applied magnetic field • Ferromagnetic couplings increase, whereas antiferromagnetic couplings decrease in the field • Revealed $C2$ monoclinic symmetry in the high field phase
$Ni_3V_2O_8$	• Magnetic field effect on optical band gap • Magnetochromic effect • Spin-charge coupling	• Optical band gap shift $\sim$50 meV at 37 T • $Ni_3V_2O_8$ appears more green in applied magnetic field • Charge density changes by $\approx\pm$3% around O center and by $\approx\pm$1.5% around Ni centers in the field
$RIn_{1-x}Mn_xO_3$	• Magnetochromic effect • Chemical doping • Spin-glass behavior	• $TbInO_3$ appears less orange in magnetic field • Doped magnetic ion introduces the Mn *d-d* excitation in the visible range and increases magnetochromic effect • Spin glass transition behavior shows that $TbInO_3$ is ferromagnetic, whereas $GdInO_3$ and $DyInO_3$ are antiferromagnetic

ceptibility. Spiral magnetic order is quenched when $x \sim 0.2$ and results in a weak ferromagnetism. Compared with non-magnetic impurities like La^{3+}, Nd^{3+} is a stronger quencher and yields non-linear B_C–x behavior.

α-Fe_2O_3 is the parent compound from which other complex oxides derive. It attracted our attention as a model antiferromagnet with large exchange couplings that result in well-separated excitations and experimentally-realizable critical fields for magnetic structure modification [28–30]. We combine optical spectroscopy with high magnetic field techniques, complementary numerical calculations, and an appropriate symmetry analysis to study magnetochromism in α-Fe_2O_3. The intensity of *d*-*d* excitation is reduced with field through spin flop transition. As a consequence, α-Fe_2O_3 appears more red in high field. This chameleonic effect arises because the Fe^{3+} on-site excitations are intrinsically coupled to magnetic ordering, an effect amplified by the presence of the spin flop transition. Analysis of the exciton pattern superimposed on the color band reveals monoclinic $C2$ symmetry in the high field phase, providing a powerful and general illustration of how this type of analysis can be used for magnetic symmetry determination.

$Ni_3V_2O_8$ gained our attention because of its small exchange interaction, high frustration, and a rich phase diagram. These intrinsic characteristics make the critical field for saturation of the magnetization realizable. We employed the optical spectroscopy with applied field up to 45 T and combined with electronic structure calculations to investigate the field-induced electronic structure change in $Ni_3V_2O_8$. As a result, the optical band gap shifts from 2.35 eV to 2.40 eV at 37 T in the low temperature. This field-induced shift makes the crystal appears more green. We verify this picture with direct photographic images and discuss the transition in terms of coupling-induced modifications to the charge density. Strikingly, the field-induced modification of the gap edge below the critical field ($\approx$1.4 meV/T) is larger than the temperature-induced

shift (≈0.2 meV/K = 0.3 meV/T), and it exceeds what might be expected from the Zeeman effect (4.8 meV at 37 T; 0.13 meV/T) by a considerable amount. This implies that field is a more effective tuning parameter than temperature in $Ni_3V_2O_8$. These findings reveal that dynamic spin-charge coupling makes field so effective in driving the electronic structure change in the field and it is larger than the static analog.

Ferroelectric $R\mathrm{In}_{1-x}\mathrm{Mn}_x\mathrm{O}_3$ is promising for large spin-charge coupling effect because of the enormous spin-orbit coupling of rare earth elements, high frustration, and presence of the magnetic chromophore. We employed the magneto-optical spectroscopy to investigate spin-charge coupling in these materials. The result shows a large change in the absorption spectrum with applied field in $TbInO_3$. Moreover, the f electron excitations in $DyInO_3$ change dramatically in the field, a result of the Zeeman effect. When doped with Mn ions, the magnetic response of the material is increased, and Mn d-d excitations emerge in the visible range and give rise to the green and blue color to $TbIn_{0.997}Mn_{0.003}O_3$ and $DyIn_{0.99}Mn_{0.01}O_3$, respectively. These findings improve the fundamental understanding of the impact of rare earth element and frustration on large spin-charge coupling.

The remainder of the dissertation is organized as follows: Chapter 2 presents a literature survey of model complex oxides with a focus on the systems of interest here, Chapter 3 discusses the basics of infrared and optical techniques, interaction of light with solids, and the sample preparation and characterization. Chapter 4 presents our optical investigation and results on $BiFeO_3$ tetragonal film, nanoparticles, and the Nd doped materials, focusing on ferroelectric transition, optical band gap, and cycloid magnetic ordering. Chapter 5 is devoted to collective excitations and magnetochromism in α-Fe_2O_3. Chapter 6 details field induced band gap shift and spin charge coupling in $Ni_3V_2O_8$. Chapter 7 shows the magneto-optical properties of $R\mathrm{In}_{1-x}\mathrm{Mn}_x\mathrm{O}_3$, with the goal of understanding the interplay between magnetism and electronic structure.

Chapter 8 summarizes my work.

Chapter 2

Literature Survey of Complex Oxides

2.1 Complex oxides: multiferroicity and frustration

Complex oxides span a wide range of crystalline structures and an variety of physical phenomena. They are ideal for the study of electron correlations because of the interaction between the metal d or f electrons and oxygen p electrons. These electron correlations induce a local entanglement of the charge, spin, lattice, and orbital degrees of freedom. These interactions give rise to a variety of new physics including multiferroics, frustration, quantum critical transitions, symmetry breaking, and superconductivity, as shown in Fig. 2.1. In recent years, there has been great interest in manipulating these phenomena, as well as to create new properties. [3, 31–34]

Multiferroic materials possess simultaneous functionalities including ferromagnetism, ferroelectricity, ferrotoroidicity, and ferroelasticity in a system. [35] Coupling between ferromagnetic and ferroelectric order parameters can lead to magnetoelectric effects–

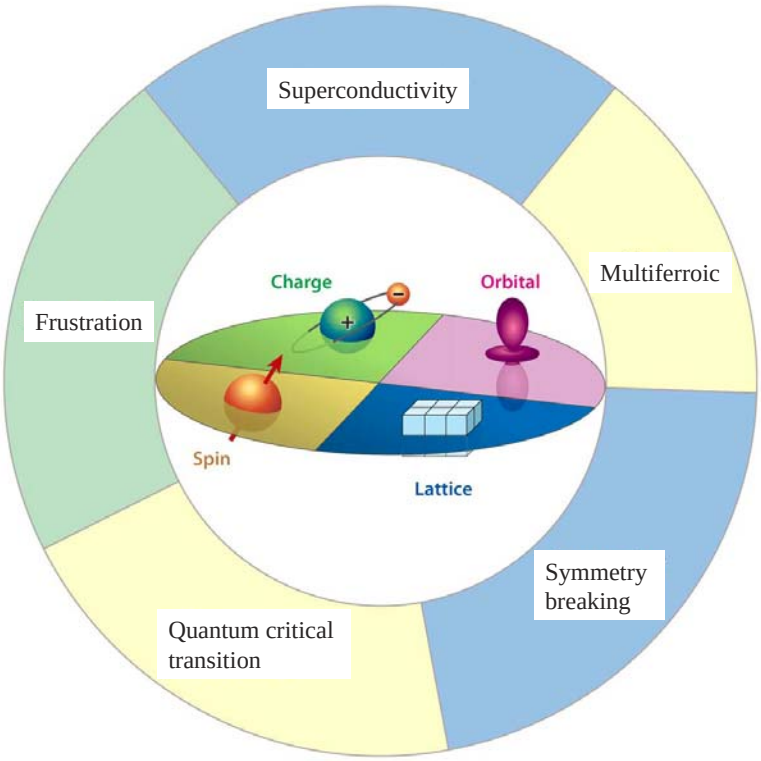

Figure 2.1: The rich physics of complex oxides including multiferroicity, frustration, superconductivity, quantum critical transition, and symmetry breaking arise from the interactions between their charge, orbital, spin, and lattice degrees of freedom. (after Ref. [5])

induction of magnetization by an electric field or of polarization by a magnetic field. This effect can be quantified from the expansion of the free energy of a material,

$$F(E,H) = F_0 - P_i^S E_i - M_i^S H_i - \frac{1}{2}\epsilon_0\epsilon_{ij}E_iE_j - \frac{1}{2}\mu_0\mu_{ij}H_iH_j - \alpha_{ij}E_iH_j \\ -\frac{1}{2}\beta_{ijk}E_iH_jH_k - \frac{1}{2}\gamma_{ijk}H_iE_jE_k - ... \tag{2.1}$$

Polarization and magnetization can be obtained by differentiating equation 2.1 to E and H, respectively.

$$P_i(E,H) = P_i^S + \epsilon_0\epsilon_{ij}E_j + \alpha_{ij}H_j - \frac{1}{2}\beta_{ijk}H_jH_k + \gamma_{ijk}H_iE_j - ..., \tag{2.2}$$

$$M_i(E,H) = M_i^S + \mu_0\mu_{ij}H_j + \alpha_{ij}E_i + \beta_{ijk}E_iH_j + \frac{1}{2}\gamma_{ijk}E_jE_k - ..., \tag{2.3}$$

where E and H are the electric field and magnetic field vector, respectively. P^S and M^S denote the spontaneous polarization and magnetization, whereas ϵ and μ are the electric and magnetic susceptibilities. The tensor α corresponds to induction of polarization by a magnetic field or of magnetization by an electric field. It is designated as the linear magnetoelectric effect. β and γ are the high order magnetoelectric effect tensors. [36] The large magnetoelectric coefficients have been observed for $LiCoPO_4$ (α_{yx} = 30.6 ps m^1), yttrium iron garnet films (30 ps m^1) and $TbPO_4$ (α_{aa} = 36.7 ps m^1). [37–39] Because of the potential of the cross-correlation between the magnetic and electric properties for technical applications, magnetoelectric coupling attract intense experimental and theoretical work. [36, 40, 41]

Single phase multiferroics have been particularly challenging to realize. This is because of the mutually exclusive mechanisms for these two properties: standard ferroelectricity in cubic perovskites requires empty d orbitals whereas ferromagnetism derives from partially filled d orbitals [32, 46]. Recently, a few multiferroics including $LuFe_2O_4$, $Ni_3V_2O_8$, and RMnO$_3$ (R = rare earth) have been identified. [3, 32–34]

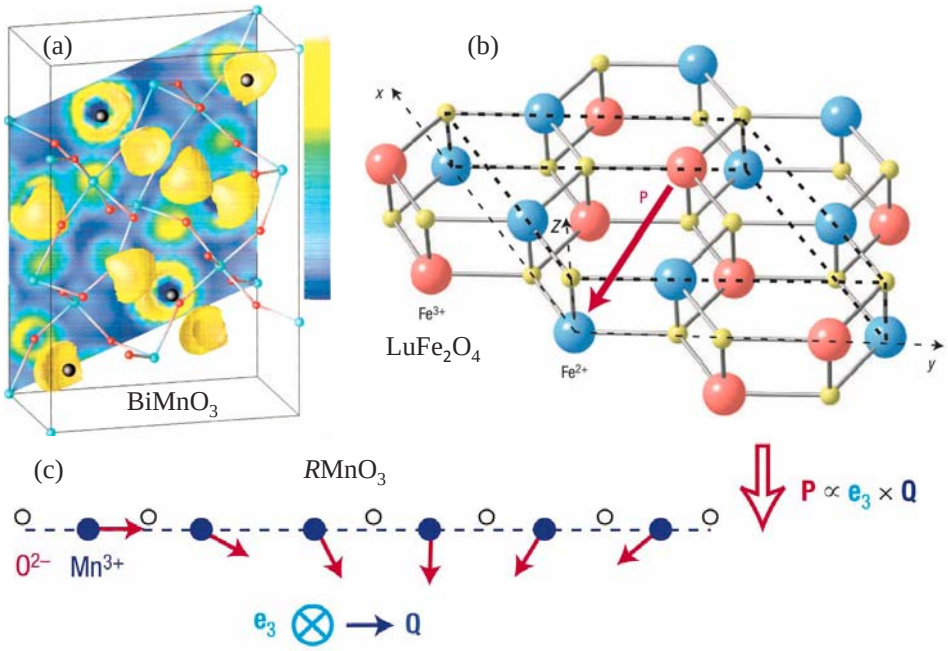

Figure 2.2: (a) Isosurface (at a value of 0.75) of the valence electron localization functions of monoclinic $BiMnO_3$ projected within a unit cell. Blue corresponds to almost no electron localization, and white corresponds to complete localization. (after Ref. [42]) (b) Charge ordering in bilayered $Lu(Fe^{2.5+})_2O_4$ with a triangular lattice of Fe ions in each layer. The charge transfer from the top to bottom layer gives rise to net electric polarization. (after Ref. [32]) (c) (weak) ferroelectricity can be induced by the exchange striction in a magnetic spiral state, which pushes negative oxygen ions in one direction transverse to the spin chain formed by positive transition metal ions. (after Ref. [32])

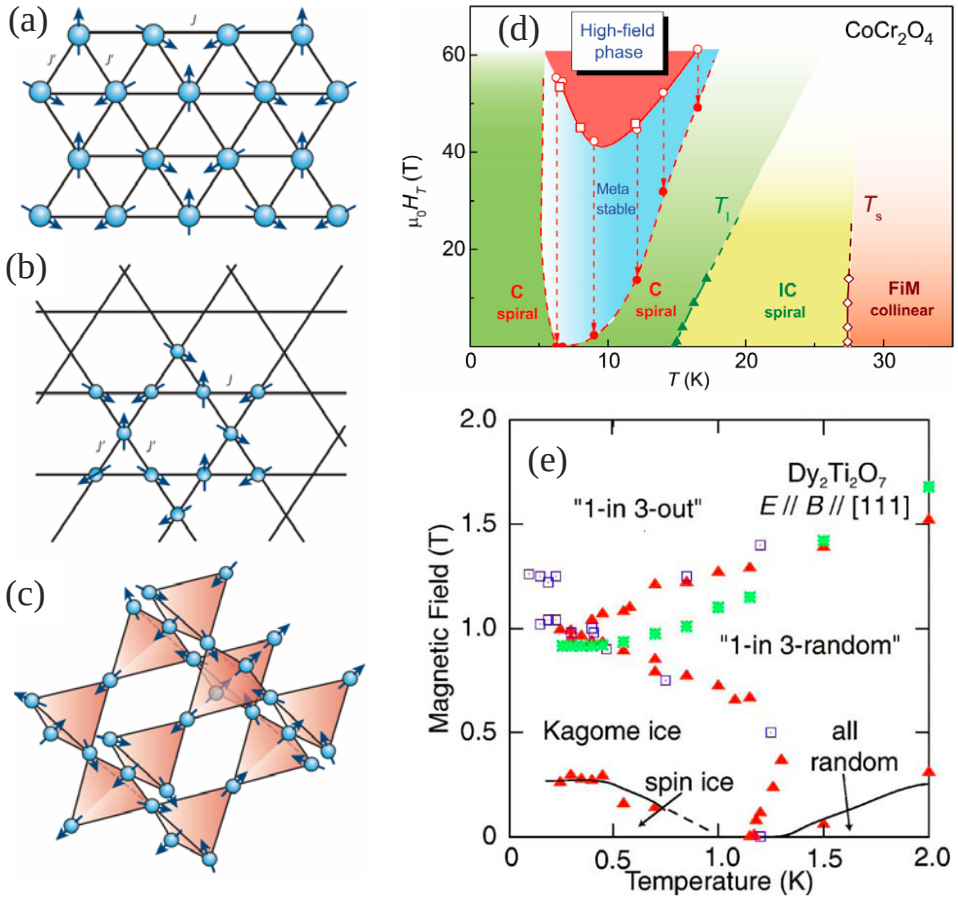

Figure 2.3: Two types of 2D lattice are depicted: (a) a triangular lattice (b) and a kagomé lattice. (c) The 3D lattice depicted is a pyrochlore lattice. (after Ref. [43]) (d) Schematic low-temperature phase diagram of $CoCr_2O_4$. The phase boundaries between the metastable phase and the helical C phase detected in the pulsed experiments are shown by dashed lines. The arrows connect the boundaries observed in increasing fields (open symbols) and decreasing fields (solid circles). The open squares and circles refer to the ultrasound data measured in the pulsed fields applied along the <001> and <111> directions, respectively (after Ref. [44]) (e) Field-temperature phase diagram of $Dy_2Ti_2O_7$ for the [111] field direction. Closed triangles indicate the peak position in the dielectric loss, open squares the peak in the specific heat, and asterisks the peak in the magnetostriction. (after Ref. [45])

$BiFeO_3$ is the only known room temperature single-phase multiferroic. [27, 31, 47] The ferroelectricity arises in $BiFeO_3$ and $BiMnO_3$ because Bi ion with two electrons on the 6s orbital (lone pair) that moves away from the centrosymmetric position in its oxygen surrounding, as shown in Fig. 2.2(a). [42] These materials are proper ferroelectrics since structural instability towards the polar state is the main driving force of the ferroelectric transition. Whereas, in improper ferroelectrics, polarization is only a part of a more complex lattice distortion or appears as an accidental by-product of some other ordering like structural transition and magnetic ordering. [32] As an example, charge ordering in $LuFe_2O_4$, crystallizing in a bilayer structure with Fe^{2+}:Fe^{3+} ratios of 2:1 and 1:2, induces electric polarization [Fig. 2.2(b)]. Furthermore, ferroelectricity induced by spiral magnetic ordering is the inverse effect, resulting from exchange striction in orthorhombic RMnO$_3$ (R = La-Gd). It involves the antisymmetric Dzyaloshinskii-Moriya interaction, as displayed in Fig. 2.2(c).

Frustration is the presence of competing forces that cannot be simultaneously satisfied. Frustrated magnetic systems, where competition often leads to exotic physical properties of materials, are particularly interesting. Geometric frustration occurs in systems of spins on lattices that involve triangular motifs, in which the nearest-neighbour interactions favour anti-aligned spins [Fig. 2.3(a)-(c)]. An empirical quantity of frustration is given by a frustration index: $f = |\theta_{CW}|/T_C$, where θ_{CW} is the Curie-Weiss temperature and T_C represents a cooperative-ordering transition temperature. [48] Complex magnetic structures and phase diagrams are observed in frustrated systems in which competing interactions between spins preclude simple magnetic orders, as shown in Fig. 2.3(d). Highly correlated state has no static order and the spins in the triangular antiferromagnet form a spin liquid, or spin ice [Fig. 2.3(e)]. In very low temperature, energy k_BT becomes too small and classical fluctuations cease, the quantum mechanical uncertainty principle produces zero-point motions comparable to

the size of the spin itself and results in a quantum spin liquid. [43]

2.2 Collective excitations in complex oxides

Optical response of an oxide is dominated by its electronic structure. Therefore, optical spectroscopy is a fundamental probe of charge and bonding in solids. [8, 13, 52] When charge, spin, and lattice degrees of freedom are strongly coupled, it is also sensitive to magnetic excitations, spin order, and lattice transitions.

Phonons are collective excitations in a periodic arrangement of atoms or molecules in condensed matter. They can be revealed by direct measurements of infrared spectrum. When phonon modes coupled with electronic excitations like *d*-*d* on site transition, the center of inversion is removed and formally forbidden transition becomes allowed. The relaxed selection rule results in the small absorption coefficient [Fig. 2.4(b) inset]. [8] The temperature dependent of oscillator strength in this *d*-*d* excitation range is an exponential function and described by $f = f_o(1 + \exp(-\theta/\mathrm{T}))$, where θ represents the energy of this phonon mode. [53, 54]

An exciton is a bound state of an electron and a hole which are attracted to each other by the Coulomb interaction. [55] It form when an electron is excited from the valence band into the exciton levels in conduction band. The electron in the conduction band is then attracted to a localized hole left by the electron. Consequently, the exciton has slightly less energy than the unbound electron and hole. A typical optical absorption spectrum of exciton is shown in Fig. 2.4(c) A hydrogenic model well describes the energy level distributions of exciton, $E(n) = E_g - \frac{R^*}{n^2}$, where E_g and R^* are the band gap and the effective Rydberg constant. [56]

Magnons are quantized Bosonic excitations of the periodic magnetic order of a material. [57] Magnons typically have lower energies as compared to phonons, since the energy scale of the magnetic interactions is often lower. Unlike phonons, magnons

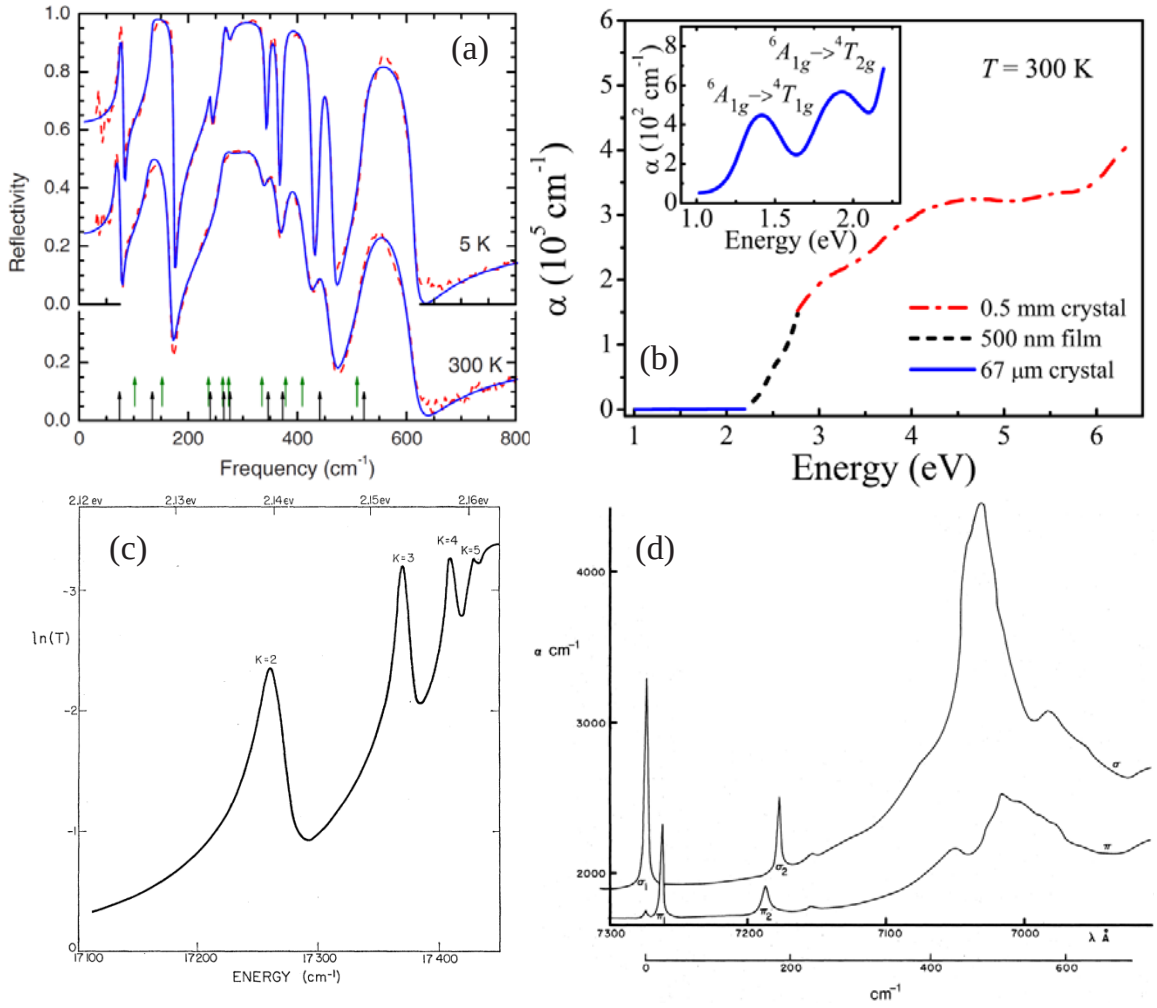

Figure 2.4: (a) In-plane (electric field of light E⊥z) infrared reflectivity of a $BiFeO_3$ single crystal at 5 and 300 K. (after Ref. [49]) (b) 300 K absorption coefficient α(E) as a function of energy. Inset: closeup view of *d-d* excitations (after Ref. [8]) (c) The logarithm of the transmission of a Cu_2O sample as 77 K, showing the details of the yellow series of excion lines. (after Ref. [50]) (d) Polarized magnon sideband in Cr_2O_3 at 2 K. (after Ref. [51])

are typically invisible in the optical spectrum because of the spin forbidden selection rule. The symmetry can be broken when an exciton is coupled with a magnon, which is magnon sideband, as shown in Fig. 2.4(d). In this absorption process, the exciton and magnon have equal and opposite wave vectors k and -k. The magnon sideband frequency can be expressed as $\omega = \omega_e + \omega_m$ [58], where ω_e is the exciton frequency, and ω_m is the magnon frequency. Its intensity is dependent upon (i) exciton + magnon joint density of states and (ii) collinearity of the magnetic structure. [12, 13] The magnon sideband density of states $\rho_{e-m}(\omega)$ is defined as [51]

$$\rho_{e-m}(\omega) = \sum_{\overrightarrow{k},u,v} \delta[\omega - \omega_e(-\overrightarrow{k}, u) - \omega_m(\overrightarrow{k}, v)], \tag{2.4}$$

where ω_e is the exciton frequency, ω_m is the magnon frequency, δ is Dirac delta function, and u and v represent exciton and magnon branches, respectively.

Optical methods are typically non-intrusive, and can be performed with other experimental variables such as magnetic fields, temperatures and pressures. With these stimuli, optical spectroscopy provides foundational microscopic insight into the electronic and magnetic structures of complex oxides.

2.3 Multiferroic $BiFeO_3$

Bulk $BiFeO_3$ is ferroelectric (T_C∼1100 K) and antiferromagnetic (T_N∼640 K) at 300 K. The structure is a rhombohedrally distorted perovskite [59] with space group $R3c$. The primitive cell contains two formula units that can be described by (i) the displacement of Fe^{3+} and Bi^{3+} cations along the pseudocubic [111] direction which causes the ferroelectric polarization, and (ii) an accompanying antiphase rotation of the neighboring FeO_6 octahedra. Each Fe^{3+} center is coordinated by six O^{2-} ions [Fig. 2.5], although the distortion along [111] yields a quasi-octahedral arrangement. The large polarization

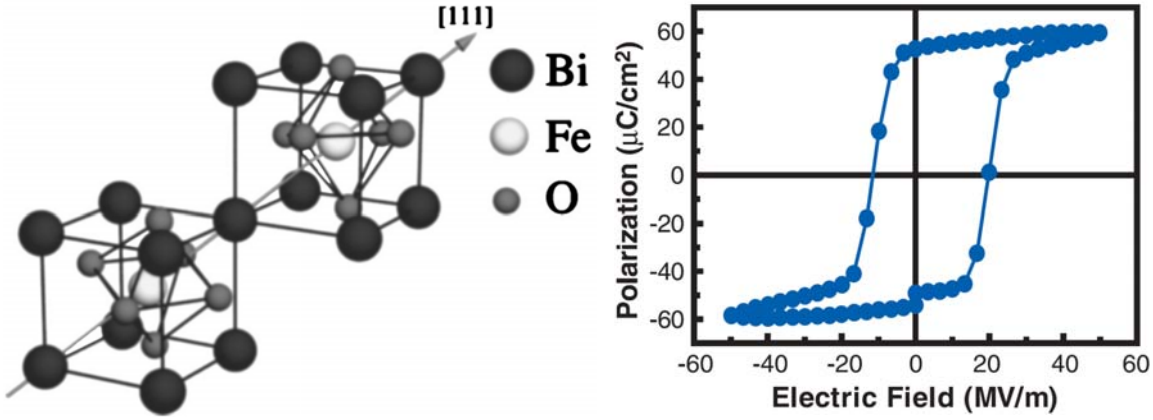

Figure 2.5: (Left) Structure of $R3c$ $BiFeO_3$. (after Ref. [27]) (Right) Polarization of a $BiFeO_3$ epitaxial thin film. The ferroelectric hysteresis loop shows that the film is ferroelectric with $P_r \sim 55\mu C/cm^2$. (after Ref. [31])

(50-90 μ C/cm^2) was first found in epitaxial film measurement [Fig. 2.5]. [31] It was also found in single crystal and ceramics. [60,61] The theoretical calculations predict a polarization 90-100 μ C/cm^2 along the [111] direction, in agreement with experiment measurements. [27]

At low temperature, magnetic order in $BiFeO_3$ shows G-type canted antiferromagnetism, in which all neighboring magnetic spins are oriented antiparallel to each other. Along $[110]_{hex}$, the order is modulated by a cycloidal spiral propagating with a period of $\sim$620 $\AA$, as shown in Fig. 2.6(a). [62,63] This spiral order can be suppressed by magnetic field ($H_C \sim$20 T) [8,64] resulting in a canted antiferomagnetic structure [65], and the domain structure can be modified with uniaxial strain [66]. Field induced polarization work indicates a 10 T critical field with 10% Nd^{3+} replacement [67], demonstrating that chemical substitution impacts spin spiral order as well. In $BiFeO_3$, the features like dielectric constant and magnon are very sensitive to variations in magnetic order and can be used to reveal the magnetic order transition. The dielectric constant was measured as a function of temperature and frequency for single crystals [Fig. 2.6(b)]. The results show that the transition near 200 K is strong elastic coupling, while those

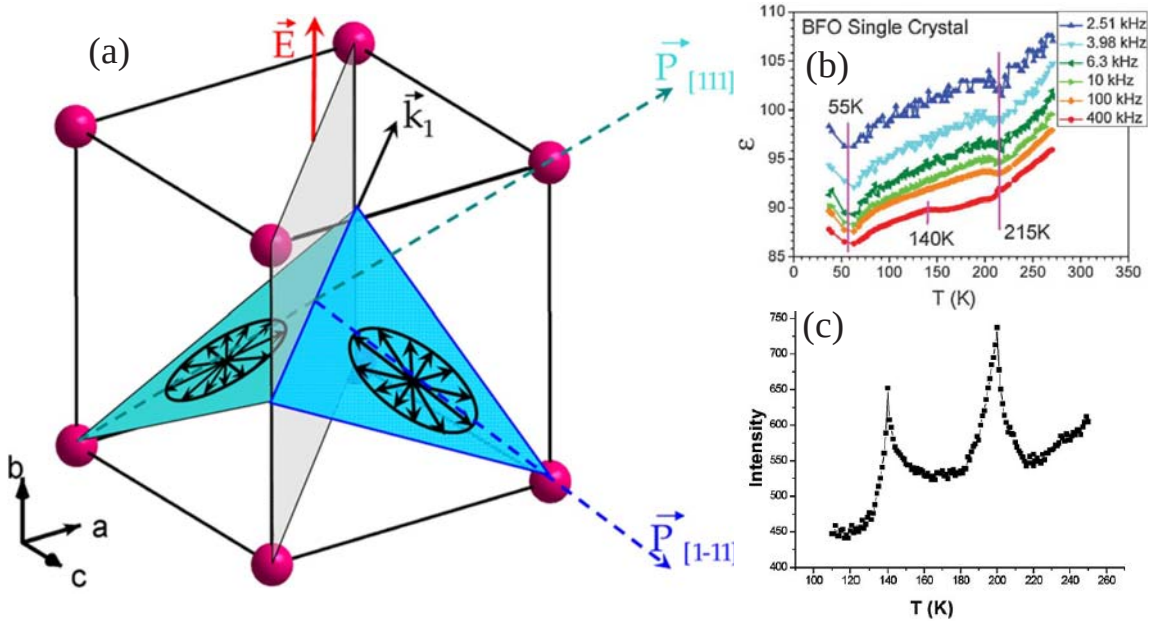

Figure 2.6: (a) Relationship between the magnetic easy plane containing the spins, the vector of ferroelectric polarization, and the vector of cycloid propagation. [63] (b) Anomalies in the dielectric constant (ε). (after Ref. [68]) (c) Intensity of magnon peaks in the Raman spectra as a function of temperature. These show clear phase transitions at 140 K and 200 K, which are tentatively attributed to spin reorientations. (after Ref. [47])

at 50 and 140 K are fundamentally magnetic. [68] Temperature dependent magnon intensity in the Raman spectra also show anomalies at ∼140 K and ∼200 K, which are interpreted as spin reorientations. [47]

Various optical measurements have been used to probe the electronic structure of $BiFeO_3$. [8,52] The direct band gap is extracted as 2.70±0.005 eV at 4 K and 2.67±0.005 eV at 300 K, as shown in Fig. 2.7. [52] The gap softens with increasing temperature. There are two anomalies at 380 K and T_N=640 K, the former of which correlates with second harmonic generation effects observed in films. [69] As temperature increases further, optical band gap becomes zero abruptly at ∼1200 K, signaling a temperature-driven metal-insulator transition. [70] At ∼1200 K, the structure becomes cubic via a second-order transition and the system becomes paraelectric. [71] Applied pressure

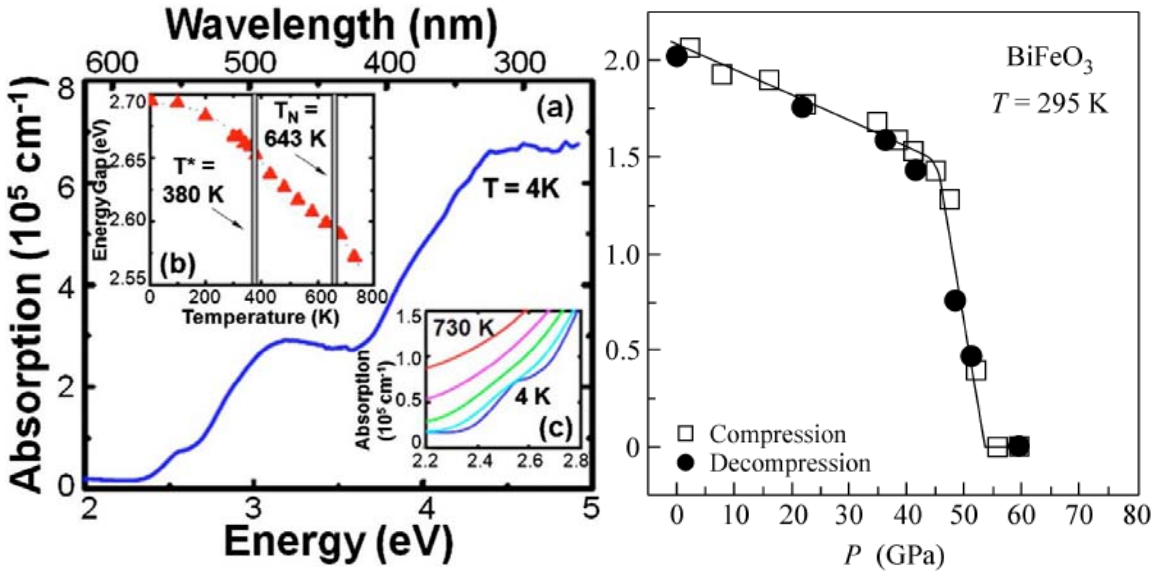

Figure 2.7: (Left) Optical absorption of a $BiFeO_3$ film at 4 K. Energy gap as a function of temperature and close-up view of the shoulder at 2.5 eV at selected temperatures 4, 300, 430, 580, and 730 K data are shown in the insets. (after Ref. [52]) (Right) Optical bandgap of $BiFeO_3$ as a function of pressure at room temperature in the (squares) compression and (circles) decompression regimes. (after Ref. [72])

also closes the band gap in $BiFeO_3$. As shown in right panel of Fig. 2.7, the optical gap is reduced with increasing pressure, and it collapses at ∼50 GPa. In high pressure, the conduction behavior suggests that holes in the e_g shell are the charge carriers. [72]

Other optical features like *d-d* on site excitations, spin wave, and magnon sideband were studied in high magnetic field. [8] Spin-orbit coupling, relaxes the spin selection rule, giving rise to the small oscillator strengths observed in *d-d* excitation. Terahertz measurements on $BiFeO_3$ indicate the modes soften close to the critical field of 18.8 T along the [001] (pseudocubic) axis, where the cycloidal structure changes to the homogeneous canted antiferromagnetic state and a new strong mode with linear field dependence appears that persists at least up to 31 T, as shown in Fig. 2.8(a). [73] Magnon sideband formation is controlled by exchange coupled pairs and therefore very sensitive to variations in magnetic order. [12, 12] A magnetic field–temperature phase diagram of $BiFeO_3$ was created by the behavior of magnon sideband in the

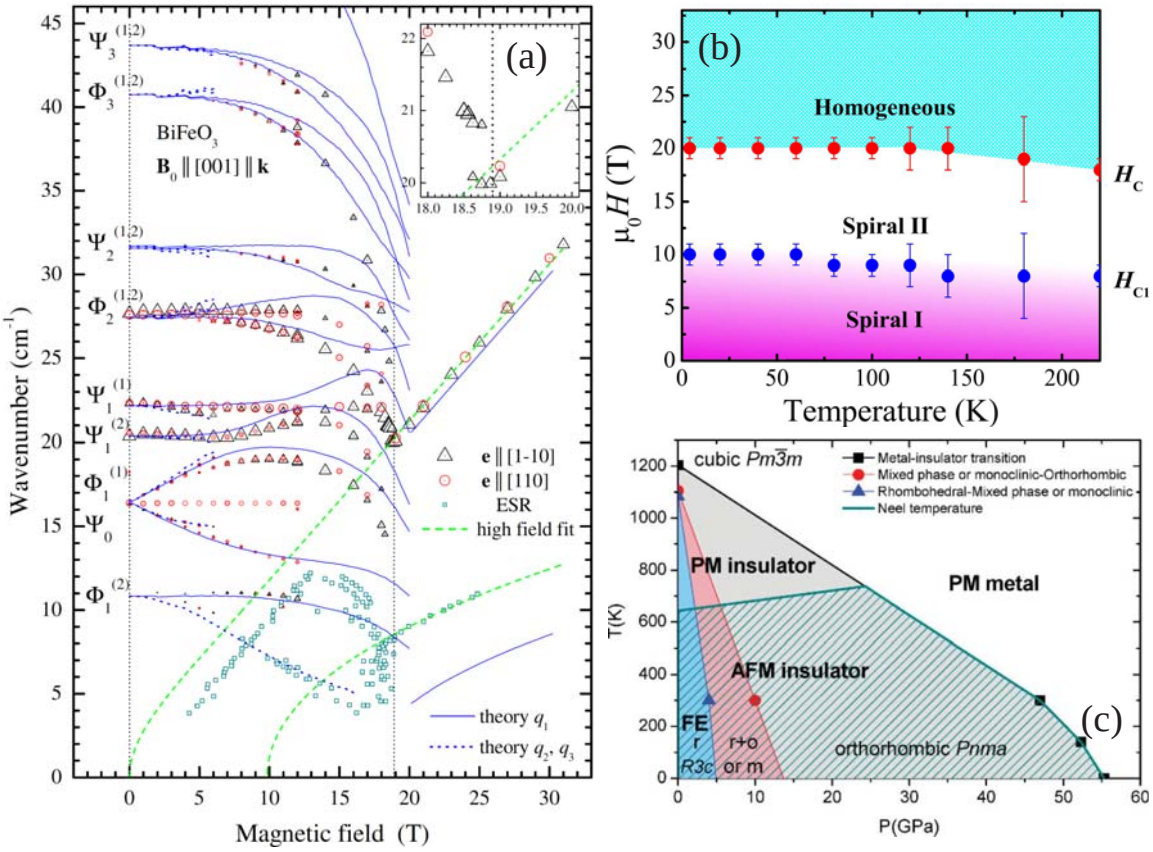

Figure 2.8: (a) Magnetic field dependence of spin wave modes in the terahertz absorption spectrum of $BiFeO_3$ at low temperature. (after Ref. [73]) (b) Sketch of a possible phase diagram as a function of pressure and temperature. Solid points are experimental data, the lines are only a visual guide. (after Ref. [47]) (c) H-T phase diagram of $BiFeO_3$. (after Ref. [8])

magnetic field [Fig. 2.8(b)]. Two critical fields (H_{C1}∼10 and H_C∼20 T) at 4.2 K are observed. The magnitudes of both critical fields decrease with temperature because increased temperature weakens magnetic order. H_C corresponds to the transition from spin spiral antiferromagnetic to homogeneous antiferromagnetic phase. And H_{C1} was proposed to be related to the rotation of the spiral plane. [8] A temperature-pressure phase diagram is proposed by Catalan *et al.* based on the pressure/doping effects and the known behavior of the magnetic transition in orthoferrites. [47] The ground state is rhombohedral and it evolves into a coexistence of rhombohedral and orthorhombic phases between 5 and 15 GPa and becomes orthorhombic above 15 Gpa. At critical pressure 50 GPa, a metal-insulator transition (T_{MI}) occurs. This transition delocalizes the electrons and induces a Pauli paramagnetic state so that the magnetic-ordering temperature, T_N, is forced to track down T_{MI}. These results indicate the flexibility of magnetic and electronic properties of $BiFeO_3$ under stimuli including temperature and pressure.

2.4 α-Fe_2O_3

α-Fe_2O_3 is commonly known as hematite. It is one of the worlds oldest and most ubiquitous antiferromagnetic materials. Although chemically and structurally simpler than many other transition metal oxides, the fundamental interactions that give rise to competing ground states and coupled properties are present in abundance. Moreover, it is the parent compound of other functional oxides like multiferroic $BiFeO_3$ and $LuFe_2O_4$. Therefore, understanding of the fundamental physical properties of α-Fe_2O_3 is critical for fabricating new complex oxides.

α-Fe_2O_3 crystallizes in the rhombohedral corundum structure ($R\bar{3}c$) at ambient conditions [74]. The system is antiferromagnetic below the 260 K Morin transition (T_M) [75], with spins lying along the [111] axis of the trigonal unit cell (left panel,

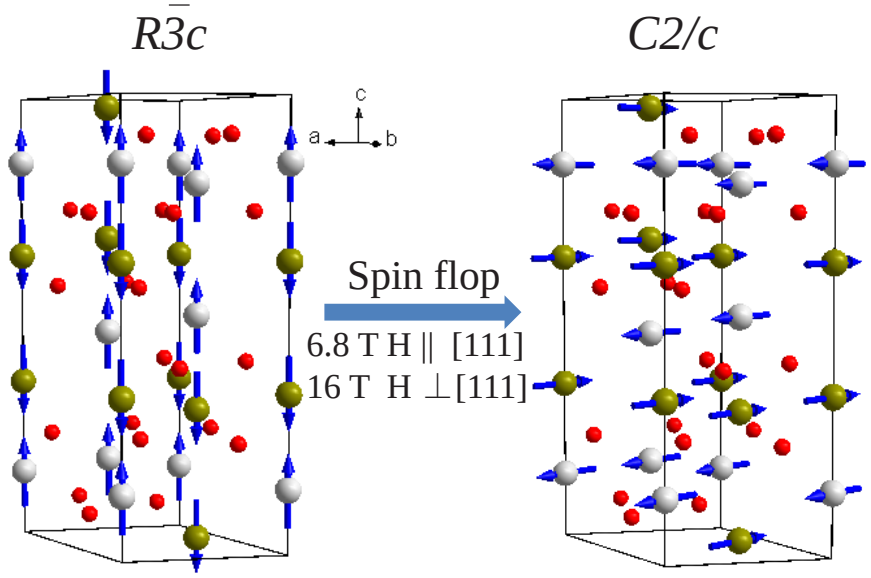

Figure 2.9: (Left) Hexagonal lattice and low temperature four sublattice spin structure ($R\bar{3}c$). [77, 80] (Right) After a spin flop to the basal plane, the symmetry becomes $C2$. [14]

Fig. 2.9). Both temperature (T_M) and magnetic field [29, 30, 76] drive a spin flop to the basal plane [77] (right panel, Fig. 2.9), and in the high temperature/field phase, α-Fe_2O_3 is weakly ferromagnetic due to a slight ($\sim 10^{-4}$ degree) spin canting [78, 79].

Figure 2.10 shows the differential magnetic moment measurements. When H$\|z$, the critical field $H_{C\|}$=68.4±0.1 kG and changes by less than 0.5 kG up to 77 K. Approaching Morin temperature, $H_{C\|}$ varies rapidly and disappears above the 260 K Morin temperature [Fig. 2.10(a)]. For H$\|y$, the differential magnetic moment shows $H_{C\perp}$=160±3 kG and is constant to within 1 kG up to 77 K. Both transitions ($H_{C\|}$, $H_{C\perp}$) show first order characters. [29] These critical fields were also traced by ultrasonic attenuation and Mössbauer measurements. [30, 81] The results are in good agreement with the differential magnetic moment data. [29]

Surface strain induced by the finite size effects provides the opportunity to tune magnet order and electronic structure. This is because surface effect becomes more and more important as the particle size decreases, due to the increase of the surface

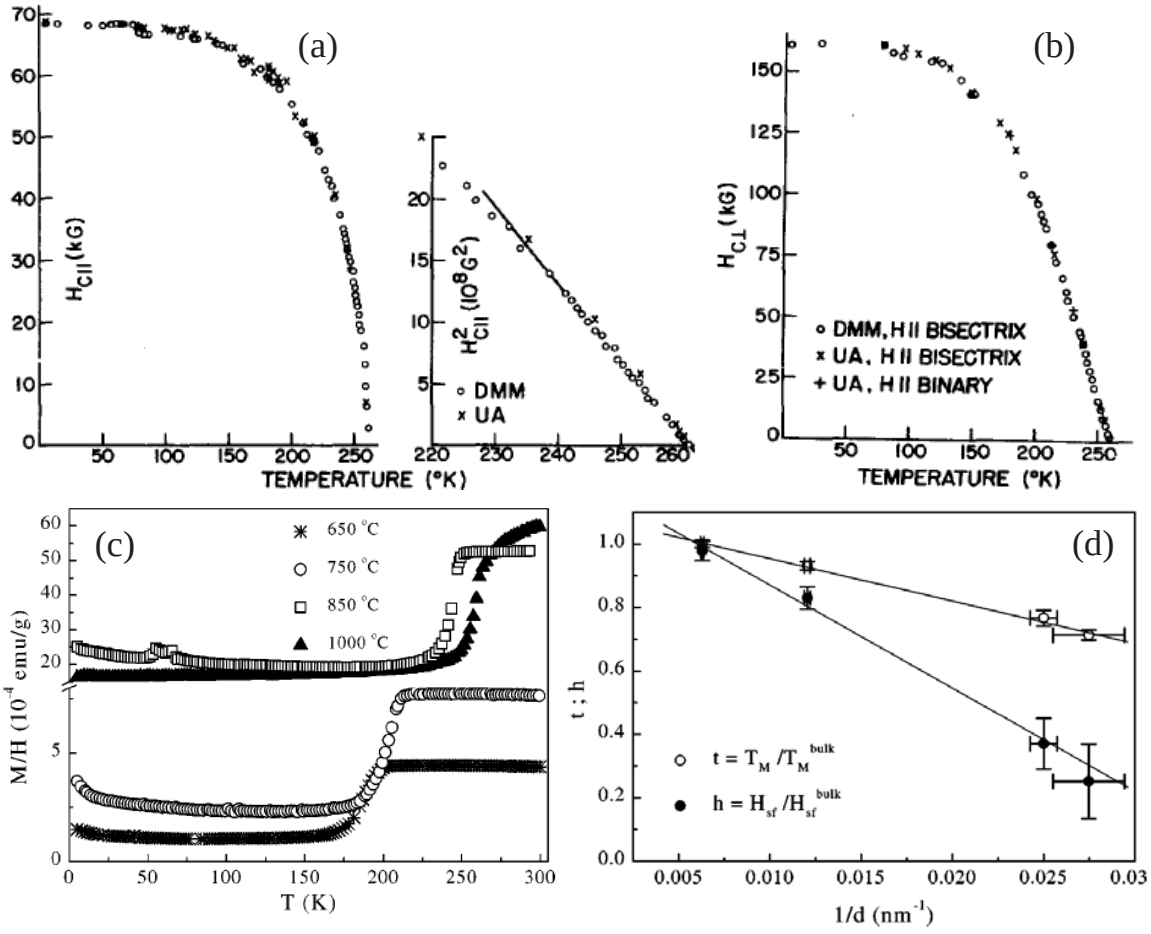

Figure 2.10: Transition critical field as a function of temperature for (a) H$\parallel$z and (b) H$\perp$z determined by the differential magnetic moment measurements. (after Ref. [29]) (c) Magnetization as a function of temperature for α-Fe_2O_3 nanoparticles annealed at different temperatures. (after Ref. [82]) (d) Spin-flop transition field and Morin transition temperature normalized to their respective bulk values [h=H_{sf}(T=0)/H_{sf}^{bulk}(T=0), open symbol; t=T_M /T_M^{bulk} , solid symbol] as a function of the reciprocal of the crystallite size. The solid lines are linear fittings to the data. (after Ref. [82])

to volume ratio. The structural and electronic properties are modified at the surface, resulting in a breaking of lattice symmetry and broken chemical bonds, giving rise to site-specific surface anisotropy, weakened exchange coupling, and surface spin disorder. [82, 83] Magnetization measurement on α-Fe_2O_3 nanoparticles show that the Morin transition increases with the annealing temperature [Fig. 2.10(c)]. [82] This result indicates the increment Morin temperature with the particle size. Figure 2.10 (d) shows both critical field and the Morin transition temperature normalized to their bulk values as a function of the reciprocal of the particle size. The linear behavior for both data sets indicates the surface effect dominates in the change of spin flop transition in nanoparticles. This can be explained by the change of anisotropy and exchange field with particle size. Moreover, the larger slopes in the curve of h versus 1/d indicate that the spin-flop transition field decreases with size at a faster rate than the Morin temperature. This result indicates a stronger sensitivity of critical field to surface effects. [82]

The optical absorption spectrum of α-Fe_2O_3 is shown in Fig. 2.11(a). The transitions at 11560, 12900, 16670 and 1869O cm^{-1} are assigned to ${}^6A_1 \rightarrow {}^4A_2$, ${}^6A_1 \rightarrow {}^4E$, ${}^6A_1 \rightarrow {}^4A_1$, ${}^6A_1 \rightarrow {}^4E$ crystal field transitions, respectively. The crystal field splitting parameter was extracted as dq=1285 cm^{-1}. [54] The transition above 26000 cm^{-1} are the O $2p \rightarrow$ Fe $3d$ charge transfer excitations which is response for the large absorption coefficient in the ultraviolet and visible regions. Oscillator strength of the ${}^6A_1 \rightarrow {}^4A_2$ transition as a function of temperature is given in Fig. 2.11(b). Using the expression $f = f_o(1 + \exp(-\theta/\mathrm{T}))$ to fit the oscillator strength trend, the parameters are extracted as $f_o = 0.85\times10^4$ and $\theta = 200$ K (139 cm^{-1}). θ represents the energy of this normal mode which breaks the center of symmetry and make the excitation allowed. The lowest optical phonon mode found from Raman scattering and from infrared spectroscopy is 247 cm^{-1}. Its energy is considerably higher than the value of θ. [85] Therefore, it can

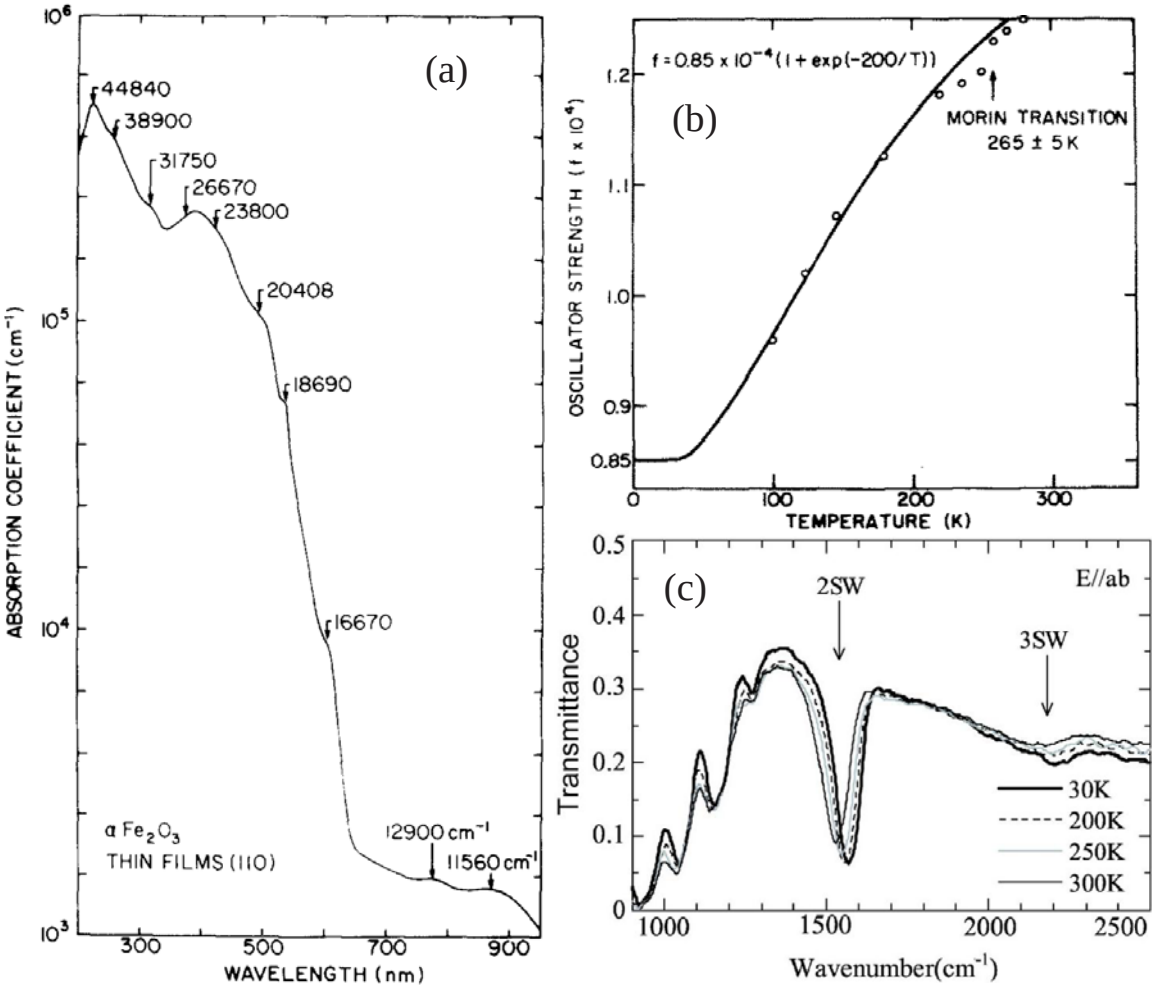

Figure 2.11: (a) Absorption coefficient as a function of wavelength for α-Fe_2O_3 at 298 K. (after Ref. [54]) (b) Oscillator strength as a function of temperature. Solid curve is theoretical fit to data. (after Ref. [54]) (c) The temperature dependence of the transmission spectrum for the polarization E in the *ab* plane. The crystal thickness is 120 μm. (after Ref. [84])

be concluded that an acoustic phonon couples this crystal field transition. Hematite displays additional collective excitations as well. As shown in Fig. 2.11(c), when the light vector E||ab plane, the two-magnon and three-magnon excitations emerge at 1550 and 2200 cm^{-1}, respectively. [84] When temperature decreases, these features blue shift and coincide with the increase of sublattice magnetization. When E||c axis, there is no two-magnon feature in the spectrum, indicating that two-magnon is highly polarized. This result is in agreement with the group theoretical analysis of the two-magnon excitation. [84]

2.5 Frustrated $Ni_3V_2O_8$

$Ni_3V_2O_8$ is a multiferroic frustrated system. The structure is orthorhombic (space group *Cmca*). [87] It is a Kagomé staircase compound with edge sharing NiO_6 octahedra. Two inequivalent Ni^{2+} (S=1) centers (spine and cross tie sites) reside in the staircase planes. Its frustration is characterized by $f = \theta_{cw}/T_N > 5$ [48], where θ_{cw} is the Weiss constant, indicating a strong frustration of the magnetic ordering. Competition between magnetic interactions and anisotropies yields complex spin structures in this system (Fig. 2.12). At zero magnetic field, $Ni_3V_2O_8$ has high temperature incommensurate phase (HTI, T_{PH}=9.1 K), low temperature incommensurate phase (LTI, T_{HL}=6.3 K), and two commensurate spin structures (T_{LC}=3.9 K, $T_{CC'}$=2.2 K) with canted antiferromagnet phases (CAF), as shown in Fig. 2.12 [34, 88]. Interestingly, it has been found that magnetic ordering in $Ni_3V_2O_8$ generates ferroelectricity and results in multiferroic in LTI phase. This is because the lattice structure deviates from the ideal Kagomé geometry which breaks spatial inversion symmetry. [86]

High field magnetization measurements indicate the existence of different high-field states with critical fields ($H_{c1} \sim 3$ T, $H_{c2} = 7$ T, $H_{c3} = 11$ T, $H_{c4} = 18$ T, and $H_{c5} = 22$ T, and $H_{c6} = 28$ T [left panel of Fig. 2.13]. A magnetization plateau is clearly

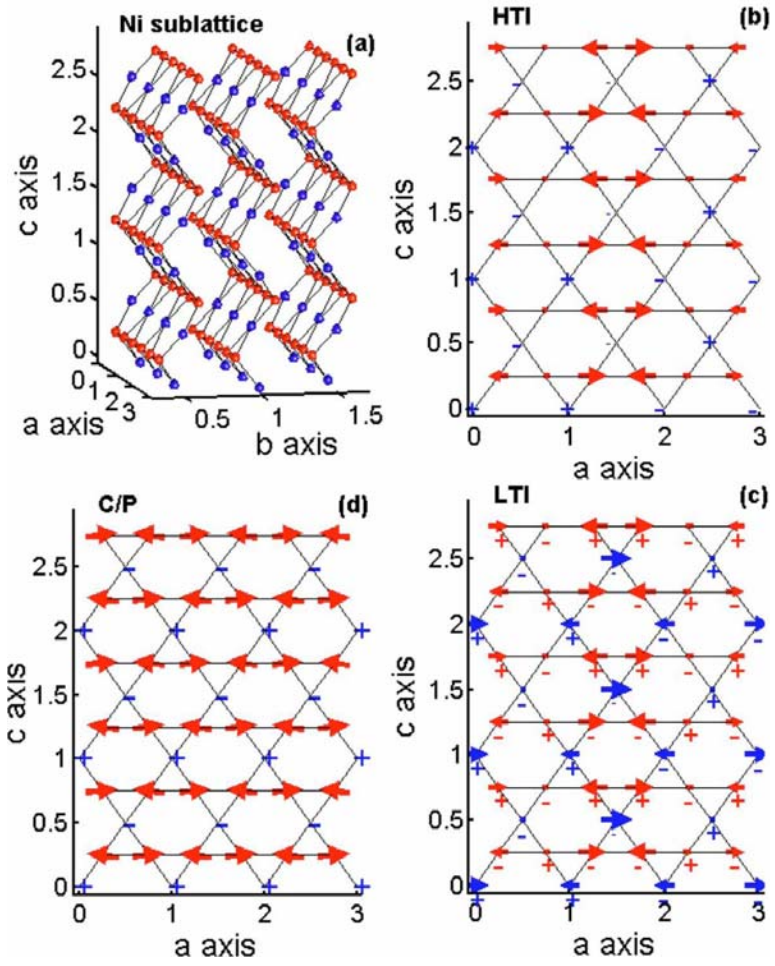

Figure 2.12: (a) Orthorhombic primitive lattice (space group $Cmca$) with blue cross-tie Ni(c) and red spine Ni(s) indicated. (b)-(d) various magnetic structures in $Ni_3V_2O_8$. The size of + and - signs corresponds to the components out of the page and into the page, respectively. In panel (d) the canting of the C phase is exaggerated for clarity. Lattice parameters serve as axis length units. (after Ref. [86])

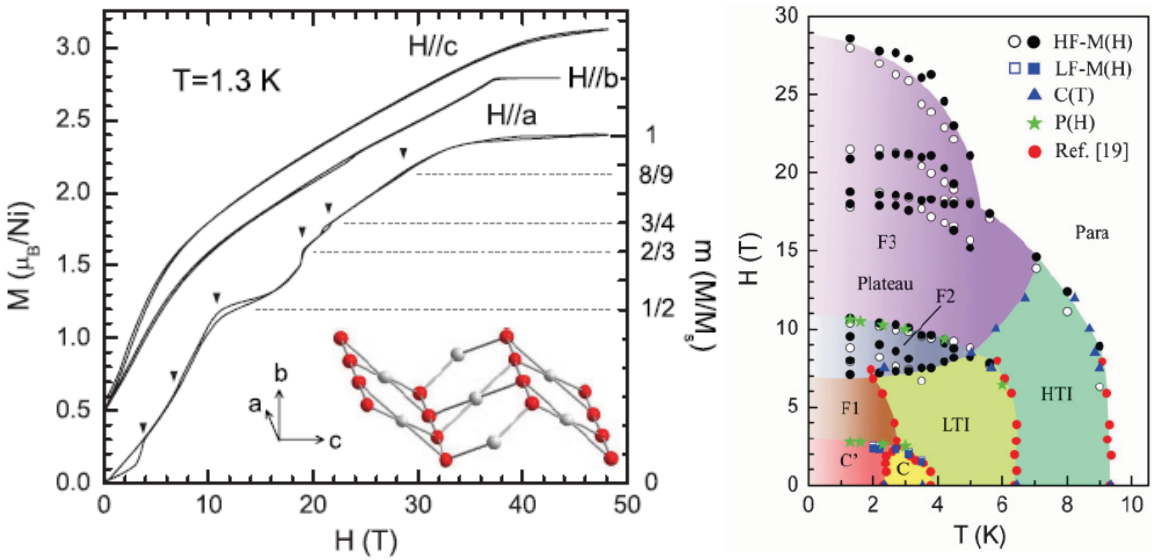

Figure 2.13: (Left) High-field magnetization processes at 1.3 K. The curves for H $\parallel$ b and H $\parallel$ c are lifted by 0.5 μ_B for clarity. Inset: Kagome-staircase plane showing the spine (red/dark gray) and the cross-tie (gray) Ni^{2+} ions. (Right) H-T phase diagram for H $\parallel$ a axis constructed using the high-field magnetization (HF-M), electrical polarization (P), specific heat (C), and low-field magnetization (LF-M) data. Open (solid) symbols are for increasing (decreasing) field. The red (dark gray) circles are reproduced from Ref. [86] for comparison. Several unique magnetic phases are explored in high magnetic fields and are indicated here as F1–F3. (after Ref. [89])

shown between H_{c3} and H_{c4}, which is suggested from an ordered state involving the cross-tie spins. [89] The saturation magnetization Ms is $\sim 2.39 \mu_B$/Ni and is close to the value calculated with a g factor of 2.3. [86] Right panel of Fig. 2.13 shows H-T phase diagram for H $\parallel$ a axis constructed using the high-field magnetization data. Multicritical phenomenon are observed. The F2 phase is an intermediate phase which separates the high- and low-field phases. Two second-order boundary lines meet at a multicritical point. The HTI-LTI phase transition is coupled to the ordering of cross-tie spins which has been determined by neutron diffraction and muon-spin relaxation measurements. [88, 90] The LTI-F2 or HTI-F3 transitions are assumed from the field induced magnetic order of the cross-tie spins and the 1/2-plateau phase is confirmed to has spin correlation with the cross-tie spins. [89]

How can the frustrated spins impact the electronic structure? Frustration plays its role in inducing spatial variations of magnetization and therefore changes the electric polarization. A transition from the paraelectric sinusoidal spin-density-wave state to the ferroelectric spiral state is observed in $Ni_3V_2O_8$ with applied magnetic field. [88] Figures 2.14(a) and (c) show the electric polarization along the b axis with magnetic fields applied along a and c axes, respectively. It is clear that the region in which field-induced polarization appears coincides with the LTI phase region. Figures 2.14 (b) shows that there is no ferroelectric order in the CAF phase at small field when H $\parallel$ a. A spontaneous polarization is produced by increasing field in the LTI phase. when H$\parallel c$, polarization is constant at the applied magnetic field. As field is increased, $Ni_3V_2O_8$ undergoes CAF ordering, which completely suppresses the spontaneous polarization. On decreasing field, polarization returns to the initial value. The field hysteresis is related to the first order LTI to CAF transition, as shown in Figures 2.14 (d). Promotion and suppression of electric polarization by applying magnetic fields suggest a magnetic gate in $Ni_3V_2O_8$. [88]

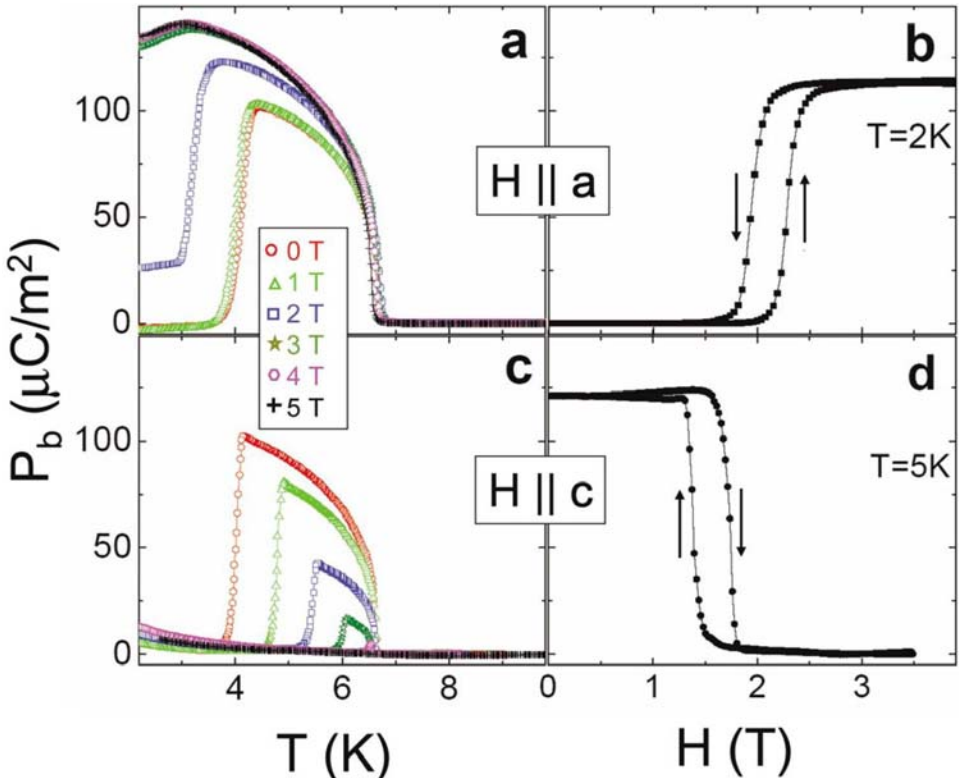

Figure 2.14: Magnetoelectric coupling effect in $Ni_3V_2O_8$. Temperature and magnetic-field dependence of electric polarization along the b axis for H along the a [panels (a) and (b)] and c [panels (c) and (d)] axes. (after Ref. [88])

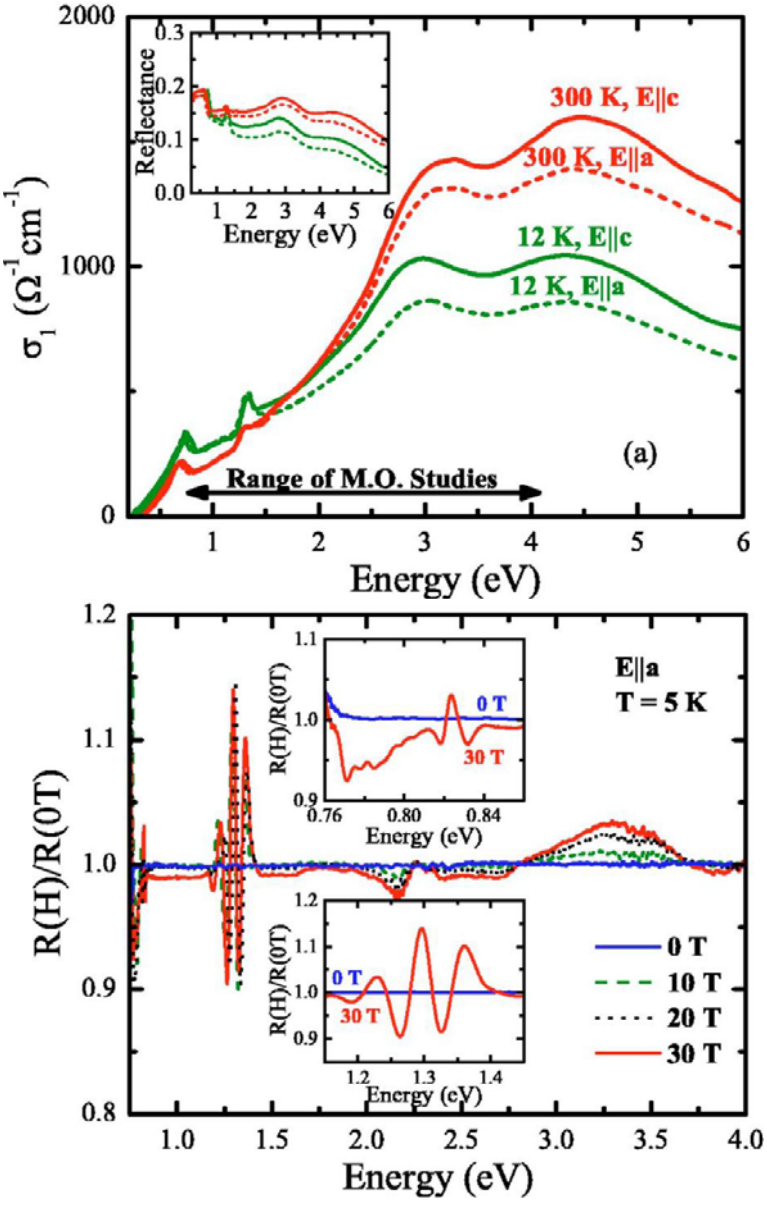

Figure 2.15: (Left panel) Polarized optical conductivity (E||c and E||a) of $Ni_3V_2O_8$ at 300 and 12 K, extracted from reflectance measurements (inset) by a Kramers-Kronig analysis. (Right panel) The normalized reflectance R(H) / R(H=0 T) in an applied magnetic field (H||b) from 0 to 30 T at 5 K E||a axis. (after Ref. [91])

The interplay between magnetism and optical properties was previously studied by reflectance measurements in the field. [91] Figure 2.15(a) displays the polarized optical conductivity of $Ni_3V_2O_8$ in the paramagnetic phase at 300 and 12 K. The features at ∼0.75, 1.35 eV are assigned as ${}^3A_{2g} \rightarrow {}^1E_g$ and ${}^3A_{2g} \rightarrow {}^3T_{1g}$ d to d excitations on the Ni^{2+} centers. [92] And broad bands at ∼3.0, 4.4 eV are O *2p* to Ni and V *3d* hybridized charge transfer excitations, which defines the optical band gap. This result suggests that $Ni_3V_2O_8$ is an intermediate gap, local-moment band insulator. The electronic structure change with field is particularly favorable for magnetodielectric couplings. Field-induced changes in reflectance is shown in Fig. 2.15(b). The reflectance changes in the visible range centered are much broader and will result in a magnetochromic effect. This remarkable interplay of magnetic field and optical properties could be useful for producing highly tunable optical filters. [93]

2.6 $R\mathbf{In}_{1-x}\mathbf{Mn}_x\mathbf{O}_3$ (R = Rare earth)

Rare earth indium oxides crystallize in hexagonal structures (space group $P6_3cm$) and are isostructural with $LuMnO_3$ [94]. The noncentrosymmetric structure gives rise to ferroelectricity in RMnO$_3$ [95]. Rare earth elements form triangular lattices in the ab plane and result in the frustration. The frustration parameter $f = |\theta_{CW}| \ / \mathrm{T}_N$ in the hexa-RMnO$_3$ system ranges from 5.8 to 10.3, indicating a high degree of magnetic frustration. [96] In the lattice structure, rare earth ions are seven-fold coordinated with two different site symmetries C_3 and C_{3v}. When the rare-earth ionic radius is large ($\mathrm{r}_R > \mathrm{r}_{Dy}$), hexagonal RMnO$_3$ transforms to orthorhombic perovskite structure (space group $Pnma$). Fig. 2.16(a) and (b) show the magnetic structure of $DyMnO_3$ at 0 and above 30 kOe based on magnetic measurements. [97] This structure is described by a three-sublattice model: a lattice of In (or Mn) that forms a 120° spin arrangement in the ab plane and two other lattices formed by the rare-earth ions with C_3 and C_{3v} site

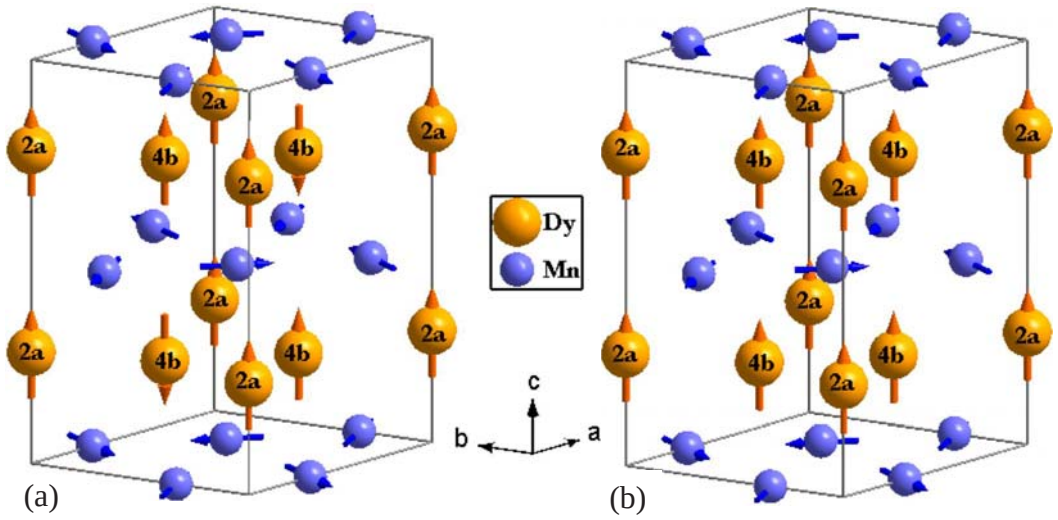

Figure 2.16: (a) Magnetic structure of the hexagonal $DyMnO_3$ crystal at (a) zero field and (b) H>30 kOe. The Dy^{3+} ions at the two inequivalent positions along with the Mn ions are shown. (after Ref. [97])

symmetries. At 2 K, the interlayer coupling between the Mn ions in the *ab* plane gives rise to a non-collinear antiferromagnetic order, in which the rare earth elements at 2a sites order ferromagnetically and those at 4b sites ions order antiferromagnetically with their magnetic moments pointing along the *c* axis. [97] When applied the magnetic field, the spins at R_{4b} ions are aligned along the *c* axis and the crystal appears weak ferromagnetic.

The rare-earth manganites are very intriguing multiferroic materials. Hexagonal $TbMnO_3$ films display ∼20 times larger remnant polarization than the value of its orthorhombic analog with the ferroelectric ordering temperature shifted from 27 to 60 K. [98] The origin of the ferroelectric ordering in hexagonal manganites is related to the tilting of the rigid MnO_5 trigonal bipyramid. [99] Figures 2.17a-d display the temperature dependence of polarization versus electric field (PE) hysteresis loops with the E parallel to the *c* axis. The PE loop at 20 K displays weak ferroelectric-like behavior with a small remnant polarization value ($< 0.25\ \mu Ccm^{-2}$). When temperature is increased to 60 K, a typical ferroelectric character emerges. As shown in Figure 3b, the

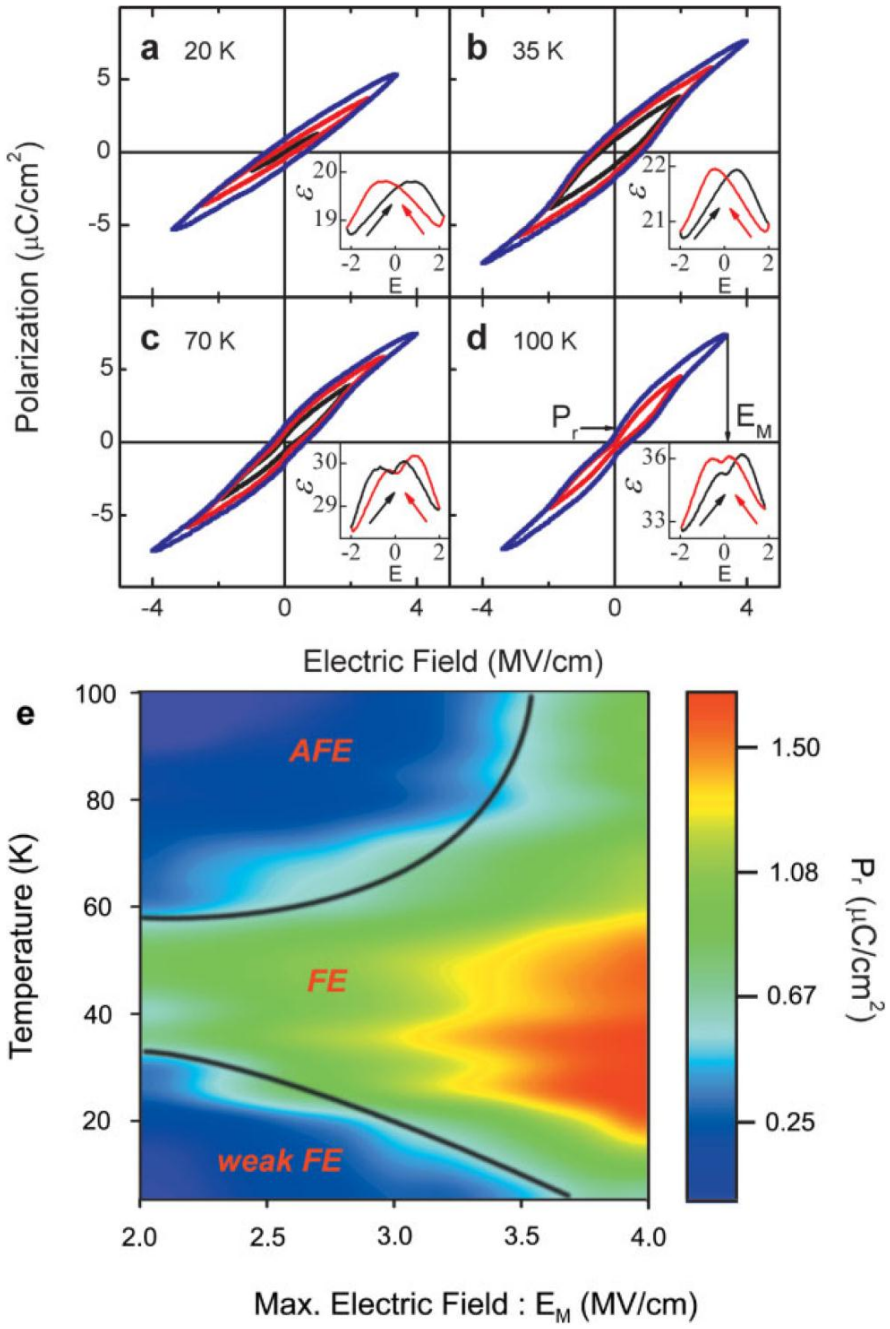

Figure 2.17: The ferroelectric properties of hexagonal $TbMnO_3$ as a function of the electric field at selected temperatures. Polarization versus electric field hysteresis loops measured at 2 kHz at a) 20 K, b) 35 K, c) 70 K, and d) 100 K. Insets show the hysteresis loops of the dielectric constant, ϵ, versus the electric field at 100 kHz. e) A phase diagram showing the ferroelectric and antiferroelectric regions as a function of temperature and electric field. The maximum remnant polarization value is also plotted. $TbMnO_3$ is antiferroelectric at $T > 60$ K, ferroelectric at $T < 60$ K, and weakly ferroelectric at $T < 20$ K. (after Ref. [98])

value of remnant polarization is ∼1.6 μCcm^{-2} at 35 K, whereas the reported saturation polarization for the orthorhombic $TbMnO_3$ is only 0.08 μCcm^{-2} at 10 K. [100] The signature of a new antiferroelectric phase is revealed above 60 K (Figs. 2.17c,d). A phase diagram was construct using the remnant polarization value as applied electric field, as displayed in Fig. 2.17e. It is clear that an antiferroelectric-ferroelectric phase transition is induced by the electric field (E) when E > 3.7 MV/cm. The coexistence of the ferroelectric phase with the antiferromagnetic ordering is expected to show magnetoelectric coupling. Such effect is verified directly by measuring the magnetocapacitance (ε(H)/ε(0) - 1). [98] These results indicate hexagonal $TbMnO_3$ films show multiferroic signatures with enhanced ferroelectric properties.

The effects of temperature and magnetic field on the electronic structure of hexagonal RMnO$_3$ thin films have been investigated using optical spectroscopy. A broad band at ∼1.7 eV is observed, as shown in Fig. 2.18. It is attributable to the intersite optical transition from the hybridized occupied states with d_{xy} /$d_{x^2-y^2}$ orbital symmetry to the unoccupied Mn $d_{3z^2-r^2}$ state. [101] The transmittance ratio spectra at different magnetic fields Tr(H) /Tr(H=0 T) also reveal the field effect on this d-d excitation. The results clearly indicated that deviation of the spectral ratio from unity becomes larger as the magnetic field increases. It is because the 1.7 eV peak red shift in the applied field due to the Zeeman effect, as shown in Figs. 2.18(c) and (d). This magneto-optical results implied that the magnetic ordering influences the electronic structure of the RMnO$_3$. A sufficiently strong external magnetic field can disturb the long-range antiferromagnetic ordering structure and decrease the on site excitation energy. The similar effect is also evidence in the temperature dependent results. A distinct anomaly around T_N is observed in the peak energy as a function of temperature. This result strongly suggests coupling between the electronic structure and the magnetic structure. [101]

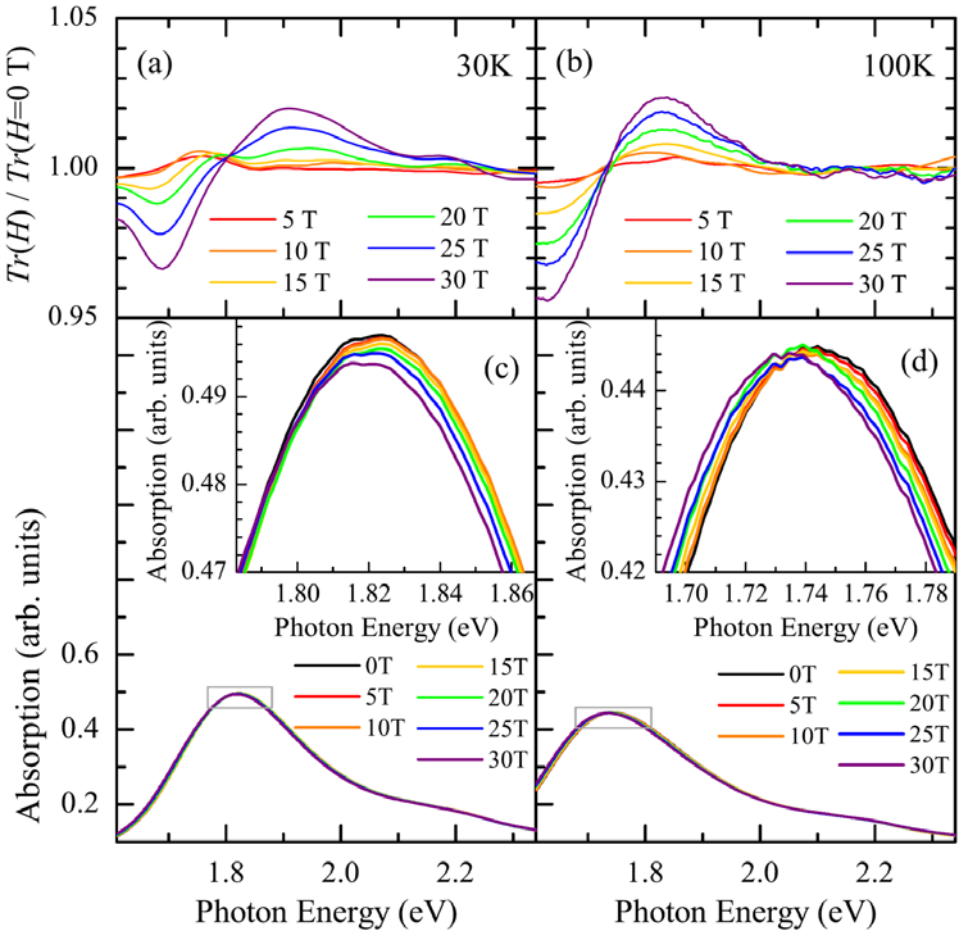

Figure 2.18: Magnetic-field dependence of the optical transition at ∼1.7 eV of hexagonal $TbMnO_3$ thin film at 30 K and 100 K. (a),(b) Transmittance ratio, Tr(H) /Tr(H=0 T) with magnetic field along the c axis from 0 to 30 T with a 5 T step. (c), (d) Absorption spectra illustrate the peak shift. The insets is the close-up view of the peak. (after Ref. [101])

Chapter 3

Experimental and Theoretical Techniques

3.1 Optical Theory

Optical properties are the results from the interaction of electromagnetic radiation with matter. They are directly related to the electronic and magnetic structure of a solid. Therefore, interpretation of the optical properties is fundamental to understand the spin and charge dynamics from a microscopic view. Experimentally, optical properties are determined from the frequency-dependent reflectance $R(\omega)$ and transmittance $T(\omega)$ measurements. We can extract the optical constants including absorption $\alpha(\omega)$, dielectric function $\varepsilon(\omega)$, optical conductivity ($\sigma_1(\omega)$), plasma frequency (ω_p), effective mass ($m^*(\omega)$), oscillator strength (S), and relaxation time ($\tau(\omega)$). The absorption $\alpha(\omega)$ and dielectric function $\varepsilon(\omega)$ are responsible for the absorptive and electronic nature of a material. And these optical constants are usually derived from Beer's law, Kramers-Kronig analysis, or Glover-Tinkham analysis. [102, 103]

3.1.1 Maxwell's Equations

The relationship between light and matter is well described by the macroscopic form of Maxwell equations (SI units) [102]:

$$\nabla \cdot \mathbf{D} = \rho^{ext} \tag{3.1}$$

$$\nabla \cdot \mathbf{B} = 0 \tag{3.2}$$

$$\nabla \times \mathbf{E} = -\frac{\partial \mathbf{B}}{\partial t} \tag{3.3}$$

$$\nabla \times \mathbf{H} = \frac{\partial \mathbf{D}}{\partial t} + \mathbf{J}^{cond} + \mathbf{J}^{ext}, \tag{3.4}$$

where $\mathbf{E}$ and $\mathbf{H}$ are the electric and magnetic fields, $\mathbf{D}$ and $\mathbf{B}$ are the displacement field and magnetic induction, J^{cond} is current density arising from the motion of conduction electrons, and J^{ext} and ρ^{ext} are current and charge density induced by external force.

For isotropic media and weak electromagnetic field, only the linear response will be retained, and we can obtain the following relations:

$$\mathbf{D} = \epsilon \mathbf{E} \tag{3.5}$$

$$\mathbf{B} = \mu \mathbf{H} \tag{3.6}$$

$$\mathbf{J}^{cond} = \sigma \mathbf{E}, \tag{3.7}$$

where ϵ is the dielectric function, and σ is the optical conductivity, and μ is the magnetic permeability. Here both ϵ and σ are scalar quantities rather than tensors for the isotropic and homogeneous media.

The complex refraction index [102]

$$N(\omega) = n(\omega) + i\kappa(\omega),$$

and the complex dielectric function

$$\epsilon(\omega) = \epsilon_1(\omega) + i\epsilon_2(\omega),$$

where n and κ are the refractive index and the extinction coefficient, $\epsilon_1(\omega)$ and $\epsilon_2(\omega)$ are the real and imaginary part of complex dielectric function, and $N(\omega)$ and $\epsilon(\omega)$ are related by the following equation

$$N(\omega) = \sqrt{\epsilon(\omega)}. \tag{3.8}$$

Finally, solving Maxwell's equations 3.1-3.4 for a plane wave

$$\mathbf{E} = \mathbf{E_0} exp[i(\mathbf{q} \cdot \mathbf{x} - \omega t)], \tag{3.9}$$

gives the following relation,

$$\epsilon(\omega) = 1 + \frac{i\sigma(\omega)}{\omega\epsilon_0}, \tag{3.10}$$

or

$$\epsilon(\omega) = \epsilon_1(\omega) + i\epsilon_2(\omega) = \epsilon_1(\omega) + \frac{4\pi i\sigma_1(\omega)}{\omega}, \tag{3.11}$$

where $\sigma_1(\omega)$ is the frequency dependent (optical) conductivity. In the case of weak absorption, $\epsilon_1 = n^2 - k^2 \approx n^2$, and $v \approx c/n$, the absorption coefficient α can be written as

$$\alpha = \frac{4\pi\sigma}{\epsilon_1 v} = \frac{4\pi\sigma}{nc}. \tag{3.12}$$

Table 3.1 lists the relationships between the various response functions.

Table 3.1: Relationships between the various response function $\epsilon(\omega)$, $\sigma(\omega)$, and $N(\omega)$

Dielectric constant $\epsilon(\omega)$	Conductivity $\sigma(\omega)$	Refractive index $N(\omega)$
$\epsilon = \epsilon_1 + i\epsilon_2$	$\epsilon_1 = 1 - \frac{4\pi\sigma_2}{\omega}$	$\epsilon_1 = n^2 - k^2$
$\sigma_1 = \frac{\omega\epsilon_2}{4\pi}$	$\epsilon_2 = \frac{4\pi\sigma_1}{\omega}$	$\epsilon_2 = 2nk$
$\sigma_2 = (1-\epsilon_1)\frac{\omega}{4\pi}$	$\sigma = \sigma_1 + i\sigma_2$	$\sigma_1 = \frac{nk\omega}{2\pi}$
$n = (\frac{1}{2}((\epsilon_1^2+\epsilon_2^2)^{1/2}+\epsilon_1))^{1/2}$	$n = (\frac{1}{2}(((1 - \frac{4\pi\sigma_2}{\omega})^2 + (\frac{4\pi\sigma_1}{\omega})^2)^{1/2} + (1 - \frac{4\pi\sigma_2}{\omega})))^{1/2}$	$\sigma_2 = (1-n^2+k^2)\frac{\omega}{4\pi}$
$k = (\frac{1}{2}((\epsilon_1^2+\epsilon_2^2)^{1/2}-\epsilon_1))^{1/2}$	$n = (\frac{1}{2}(((1 - \frac{4\pi\sigma_2}{\omega})^2 + (\frac{4\pi\sigma_1}{\omega})^2)^{1/2} - (1 - \frac{4\pi\sigma_2}{\omega})))^{1/2}$	$N = n + ik$

3.1.2 Beer's law

For a sample of thickness $d < \delta = \frac{c}{\omega k}$, the penetration depth, the absorption coefficient can be directly determined from transmittance. This is one of the simplest and well known relations.

If a light beam with intensity I_0 is incident to a small element of thickness dx with cross section of absorption σ, the change in intensity is

$$dI = -\sigma I(N_0 - N_1)dx, \tag{3.13}$$

where N_0 and N_1 are the number of atoms in the ground and excited state, respectively. On integrating over the absorption path, we obtain

$$\int_{I_0}^{I} \frac{dI}{I} = -\sigma(N_0 - N_1)\int_0^d dx. \tag{3.14}$$

Usually, the cross section and the amount of atoms are combined to an absorption coefficient and we know transmittance $T = \frac{I}{I_0}$, thus $\alpha = -\frac{1}{d}ln(T)$.

The limitation of Beer's law is the requirement of a small contribution of the re-

flectance, which is not always neglectable. If the reflectance is important, the optical constants should be determined from combined reflectance and transmittance measurements. This technique is called the Glover-Tinkham analysis and is presented below.

3.1.3 Glover-Tinkham Analysis

A single crystal surrounded by the air can be approximated using the three-layer model. The complex refractive indices are N_1, N_2, and N_1, respectively, where $N_1 \approx 1$ and $N_2 = n + i\kappa$. When the multiple internal reflections are included, the transmission (t_c) and reflection coefficients (r_c) in normal incidence are:

$$\begin{aligned} t_c &= t_{12}t_{21}e^{i\theta}[1 + r_{21}^2 e^{i2\theta} + (r_{21}^2 e^{i2\theta})^2 + ...] \\ &= \frac{t_{12}t_{21}e^{i\theta}}{1 - r_{21}^2 e^{i2\theta}}, \\ r_c &= r_{12} + t_{12}r_{21}t_{21}e^{i2\theta}[1 + r_{21}^2 e^{i2\theta} + (r_{21}^2 e^{i2\theta})^2 + ...] \\ &= \frac{r_{12} + r_{21}e^{i2\theta}}{1 - r_{21}^2 e^{i2\theta}}, \end{aligned}$$

where $r_{ij} = \frac{N_i - N_j}{N_i + N_j}$, $t_{ij} = \frac{2N_i}{N_i + N_j}$, and the complex phase depth for crystal with thickness d is $\theta = N_2 \frac{\omega d}{c}$. The power transmittance (T_c) and reflectance (R_c) are defined as:

$$T_c = |t_c|^2 \text{ and } R_c = |r_c|^2. \tag{3.15}$$

Thus, we obtain the formula for the measured transmittance and reflectance of a crystal

$$T_c = \frac{[(1 - R_s)^2 + 4R_s sin^2\phi]e^{-\alpha d}}{(1 - R_s e^{-\alpha d})^2 + 4R_s e^{-\alpha d} sin^2(\phi + \beta)}, \tag{3.16}$$

$$R_c = \frac{(1 - e^{-\alpha d})^2 + 4e^{-\alpha d} sin^2\beta}{(1 - R_s e^{-\alpha d})^2 + 4R_s e^{-\alpha d} sin^2(\phi + \beta)} R_s. \tag{3.17}$$

Here, single bounce reflection of the crystal $R_s = |r_{12}|^2 = \frac{(1-n)^2+\kappa^2}{(1+n)^2+\kappa^2}$, phase ϕ is defined as $r_{12} = \sqrt{R_s}e^{i\phi}$ and $\tan\phi = -\frac{2\kappa}{1-n^2-\kappa^2}$, phase depth $\beta = n\frac{\omega}{c}d$, α is the absorption coefficient of the crystal, ω is the photon frequency, and c is the light speed. Integrating Eqs. 3.16 and 3.17 over $d\beta$, we get

$$T_c = \frac{(1-R_s)^2 e^{-\alpha d}}{1-R_s^2 e^{-2\alpha d}}, \tag{3.18}$$

$$R_c = \frac{1+(1-2R_s)e^{-2\alpha d}}{1-R_s^2 e^{-2\alpha d}} R_s. \tag{3.19}$$

Therefore, optical constants n and α of the crystal can be extracted from Eqs. 3.18 and 3.19 using frequency dependent T_c and R_c as inputs.

If the material is a thin film on a substrate with index n, it becomes a four-layer problem (Fig. 3.1). The film can be treated as a sheet of conductor with complex admittance $y_1 + iy_2$. The transmission through the film (T_f) and the reflectance (R_f) from the film is approximated as [103]

$$T_f = \frac{4n}{(y_1+n+1)^2+y_2^2}, \tag{3.20}$$

$$R_f = \frac{(y_1+n-1)^2+y_2^2}{(y_1+n+1)^2+y_2^2}. \tag{3.21}$$

The complex admittance is related to the conductivity σ by

$$y_1 + iy_2 = Z_0(\sigma_1 + i\sigma_2)d, \tag{3.22}$$

where d is the thickness of the film and $Z_0 = 376.7\ \Omega$ is the impedance of free space.

When the absorption coefficient is large in the film, the overall reflectance and

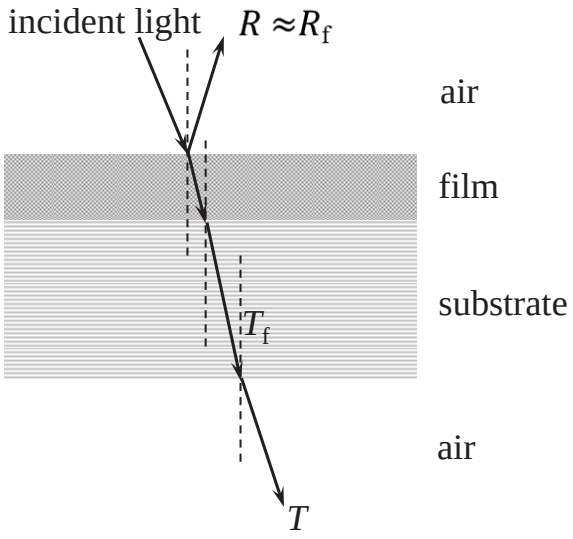

Figure 3.1: Schematic diagram of four-layer model used in Glover-Tinkham analysis. The light beams are tilted from the normal for clarity.

transmittance in this four-layer system are

$$R \approx R_f, \tag{3.23}$$

$$T = \frac{(1 - R_s)e^{-\alpha d}}{1 - R_s R'_f e^{-2\alpha d}} T_f. \tag{3.24}$$

Here,

$$R'_f = \frac{(y_1 - n + 1)^2 + y_2^2}{(y_1 + n + 1)^2 + y_2^2}, \tag{3.25}$$

and d is the thickness of the film. The refractive index n and absorption coefficient (α) of the substrate can be obtained by independently measuring the transmittance and reflectance of the substrate using the three-layer model mentioned above with Eqs. 3.18 and 3.19. Combined with measurements of T and R for the film+substrate, we can determine the optical constants $\sigma_1(\omega)$ and $\sigma_2(\omega)$.

3.1.4 Kramers-Kronig Analysis and Sum Rules

The dielectric function can be derived by Kramers-Kronig transformation of the reflectance spectrum measured over a wide frequency range. The reflectivity is defined as:

$$r = \frac{E_r}{E_i} = \frac{N_a - N_b}{N_a + N_b}, \tag{3.26}$$

where N_a and N_b are refraction indices of mediums a and b. When the light is incident from vacuum onto a sample surface at normal incident, which means that N_a=1, and N_b=N=n+$i\kappa$, the power reflectance is given by

$$R(\omega) = rr^* = \frac{(1-n)^2 + \kappa^2}{(1+n)^2 + \kappa^2}. \tag{3.27}$$

The power reflectance $R(\omega)$ and phase-dispersion shift $\phi(\omega)$ are related by Kramers-Kronig transformation [102]:

$$\phi(\omega) = \frac{\omega}{\pi} \int_0^\infty \frac{lnR(\omega) - lnR(\omega')}{\omega'^2 - \omega^2} d\omega'. \tag{3.28}$$

Since reflectivity

$$r = \sqrt{R} e^{i\phi}, \tag{3.29}$$

and combining Eqs. 3.27, 3.28, and 3.29, n and k can be determined by $R(\omega)$ and $\phi(\omega)$ as

$$n(\omega) = \frac{1 - R(\omega)}{1 + R(\omega) - 2\sqrt{R(\omega)} cos\phi(\omega)} \tag{3.30}$$

$$\kappa(\omega) = \frac{2\sqrt{R(\omega)} sin\phi(\omega)}{1 + R(\omega) - 2\sqrt{R(\omega)} cos\phi(\omega)}. \tag{3.31}$$

Then from Eqs. 3.8 and 3.11, the real part of dielectric function and the real part of

optical conductivity can be determined:

$$\epsilon_1 = n^2 - k^2 \tag{3.32}$$

$$\sigma_1 = \frac{\omega\epsilon_2}{4\pi} = \frac{\omega nk}{2\pi}. \tag{3.33}$$

All of these optical constants are frequency dependent. In Eq. 3.28, the integration is from zero to ∞. Since our optical measurements usually cover the frequency range from far-infrared to ultraviolet, proper extrapolations should be used. In this dissertation, either a Hagen-Rubens relation $R(\omega) = 1-(2\omega/\pi\sigma_0)^{1/2}$, is used for a metallic material; or as a constant for semiconductor in the low frequency range. In the high frequency, the optical response is modeled as $R \sim \omega^{-\alpha}$, where α varies from 0-4 and can be determined by comparing the absorption and calculated optical conductivity.

Together with physical arguments about the behavior of the response in certain limits, the Kramers-Kronig relation can also be used to derive sum rules. That is

$$\int_0^\infty \omega' Im(-1/\epsilon(\omega'))d\omega' = 1/2\pi\omega_p^2, \tag{3.34}$$

where ω_p is the plasma frequency. A partial sum rule [102] is also useful in quantifying the change of absorption spectra

$$f \equiv \frac{2c}{N_e\pi\omega_p^2}\int_{\omega_1}^{\omega_2} n\alpha(\omega, B)\,\mathrm{d}\omega. \tag{3.35}$$

Here, f is the oscillator strength, N_e=5 is the number of electrons per magnetic ion site, n is the refractive index, ω_p is the plasma frequency$\equiv\sqrt{\frac{e^2\rho}{m\epsilon_0}}$, e and m are the charge and mass of an electron, ϵ_0 is the vacuum dielectric constant, ρ is the density of magnetic ion sites, c is the speed of light, and ω_1 and ω_2 are the frequency limits of integration.

3.2 Spectrometers

3.2.1 Bruker IFS 113v Fourier Transform Infrared Spectrometer

The majority of the far-infrared (30-600 cm^{-1}) and middle infrared (500-5000 cm^{-1}) reflectance and transmittance spectra in this work were obtained by using Bruker IFS 113v Fourier Transform Infrared (FTIR) spectrometer. The schematic of the optical components of the Bruker IFS 113v FTIR spectrometer is illustrated in Fig. 3.2. The spectrometer is divided into four chambers – source, interferometer, sample, and detector. Light from the source chamber is focused on the beamsplitter at a small angle of incidence, and is split into two beams, i.e., one reflected and one transmitted. Both reflected and transmitted beams go to a moving two-side mirror (the position of which is tracked by a He-Ne laser), which gives a path length difference. Then the two beams are recombined at the beamsplitter and directed through the sample chamber to the detector. The Si or B-doped Si bolometer provides the extra sensitivity. The entire system is operated under vacuum.

Interferometer and beamsplitter

The Bruker IFS 113v uses Genzel-type interferometer, which is similar to a Michelson interferometer. A Michelson interferometer is illustrated in Fig. 3.3. Here, the incident beam is split into two parts by a beamsplitter. Half of the radiation transmitted by beamsplitter is reflected from the movable mirror M_2. The other half is reflected onto the fixed mirror M_1. Both beams are recombined again at the beamsplitter, and recorded by detector D. The intensity of the recombined beams $I(x)$ (interferogram function) depends on the path difference between the fixed mirror M_1 and the moving mirror M_2. The plot of $I(x)$ as a function of path difference x is known as an interfero-

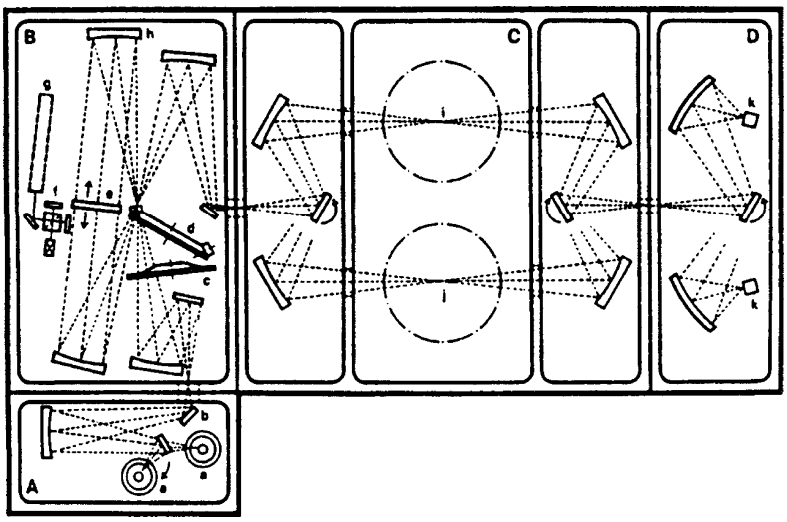

Figure 3.2: Optical layout of the Bruker 113V FTIR spectrometer.
A. Source Chamber; a- Tungsten lamp, Hg arc lamp, glowbar; b- automated aperture. B. Interferometer Chamber; c- optical filter; d- automatic beamsplitter changer; e- two-sided moving mirror; f- control interferometer; g- reference laser; h- remote control alignment mirror. C. Sample Chamber; i- sample focus; j- reference focus. D. Detector Chamber; k- far- and middle infrared deuterated triglycerine sulfate (DTGS) detector, far-infrared Si bolometer detector.

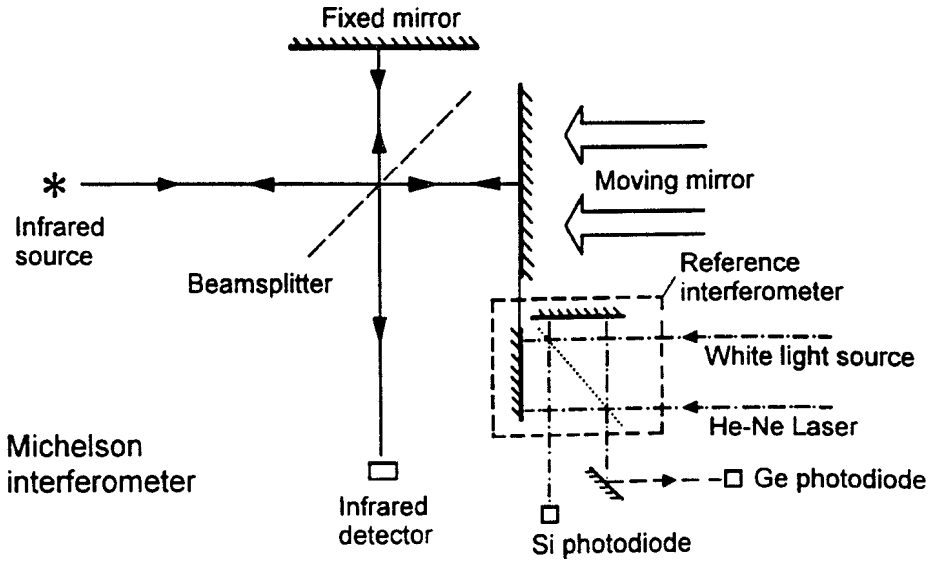

Figure 3.3: Schematic diagram of the Michelson interferometer

gram. If M_2 travels at a constant velocity, the relation between interferogram function $I(x)$ and the source intensity $B(\omega)$ is given by

$$I(x) = 1/2 \int_0^\infty B(\omega) cos 2\pi\omega dx,$$

where ω is the frequency in wavenumbers. $I(x)$ is the cosine Fourier transform of $B(\omega)$, and contains complete information about the spectrum. Thus, the Fourier transform of the interferogram gives the single beam infrared spectrum. The typical transmittance or reflectance spectrum is the ratio spectrum of sample to reference. In the Bruker IFS 113v, a secondary laser/white light interferometer physically attached to the main Genzel-type interferometer (as shown in Fig. 3.2) provides an "optical marker" to initiate the start of spectrum data acquisition and also to precisely determine the optical path difference and speed of the main moving mirror. The design is essential for accurate Fourier transformation.

Table 3.2: Bruker IFS 113v operating parameters

Range (cm^{-1})	Source	Beam splitter	Opt. Filter	Polarizer	Detector
10-50	Hg arc	Mylar 50 μ	Black PE	1	Si bolometer, DTGS
30-120	Hg arc	Mylar 23μ	Black PE	1	Si bolometer, DTGS
50-240	Hg arc	Mylar 12μ	Black PE	1	Si bolometer, DTGS
100-600	Hg arc	Mylar 3.5μ	Black PE	1	Si bolometer, DTGS
450-4000	Globar	KBr	open	2	B-doped Si bolometer, DTGS

PE = polyethylene. Polarizer 1 = wire grid on oriented PE, Polarizer 2 = wire grid on AgBr

Source, beamsplitter, detector, and accessories

In order to obtain the best far- and middle-infrared spectrum, we have to choose the appropriate combination of sources, beamsplitters, detectors, and polarizers. Table 3.2 lists the typical operating parameters. Typically, an external He-cooled Si bolometer detector made by Infrared Laboratories is used for far-infrared measurements. The intensity of a blackbody source becomes very weak in the far-infrared region, and the room-temperature DTGS detector does not have sensitivity to provide sufficiently high signal-to-noise ratio. The bolometer provides a much higher sensitivity (6-10 times better than DTGS) and lower noise level (less than 1% at liquid helium temperature).

The spectra taken with different beamsplitters are merged together to give the whole spectrum in the far- and middle- infrared. The spectra can be merged with the data taken with the Perkin-Elmer λ-900 spectrometer, as well.

3.2.2 Bruker Equinox 55 IR Microscope

The Bruker IR Scope II is designed for accurate measurement of micro samples, or small areas on larger samples. In our lab, Bruker IRscope II combined with Bruker Equinox 55 FTIR spectrometer can be used to obtain the spectrum from the middle-infrared to visible range. It is ideal for small crystals, small edges of a crystal, and

Table 3.3: Operating parameters of Bruker IRscope II

Range (cm^{-1})	Source	Beamsplitter	Detector
600-7500	Globar	KBr	MCT
4000-12000 with near-infrared polarizer	Tungsten	Quartz	InSb
9000 -17000 with visible polarizer	Tungsten	Quartz	Si diode

checking the absolute reflectance level obtained on the other instruments.

The Bruker Equinox 55 FTIR spectrometer is equipped with several sources including a Globar source, and two beamsplitters. It has an external port to transfer the incident light to the IRscope II. IRscope II has three objectives (4×, 15×, and 30×), and several detectors (MCT, InSb, and Si diode) to cover the energy range from 600-16000 cm^{-1}.

Figure 3.4 shows the optical path of Bruker IRscope II. The IRscope II can measure reflectance or transmission of the sample by changing the orientation of mirror 22. The infrared or visible mode can be chosen depending on the orientation of mirror 3 (reflectance mode) or 17 (transmission mode). The detector can be changed by flipping mirror 13. Table 3.4 lists the operating parameters of Bruker Equinox 55 FTIR spectrometer combined with IRscope II. The spectrometer is operated under N_2 purge.

3.2.3 Perkin-Elmer λ-900 Spectrometer

The near-infrared/visible/ultraviolet spectra in this dissertation were measured on the Perkin-Elmer λ-900 Spectrometer. The Perkin-Elmer λ-900 Spectrometer features an all-reflecting, double-monochromator, double-beam optical system. The energy range covered by the λ-900 Spectrometer is 3300-190 nm ($\approx$ 3000-52000 cm^{-1}). The spectrometer is operated under nitrogen purging. The optical system is depicted schemat-

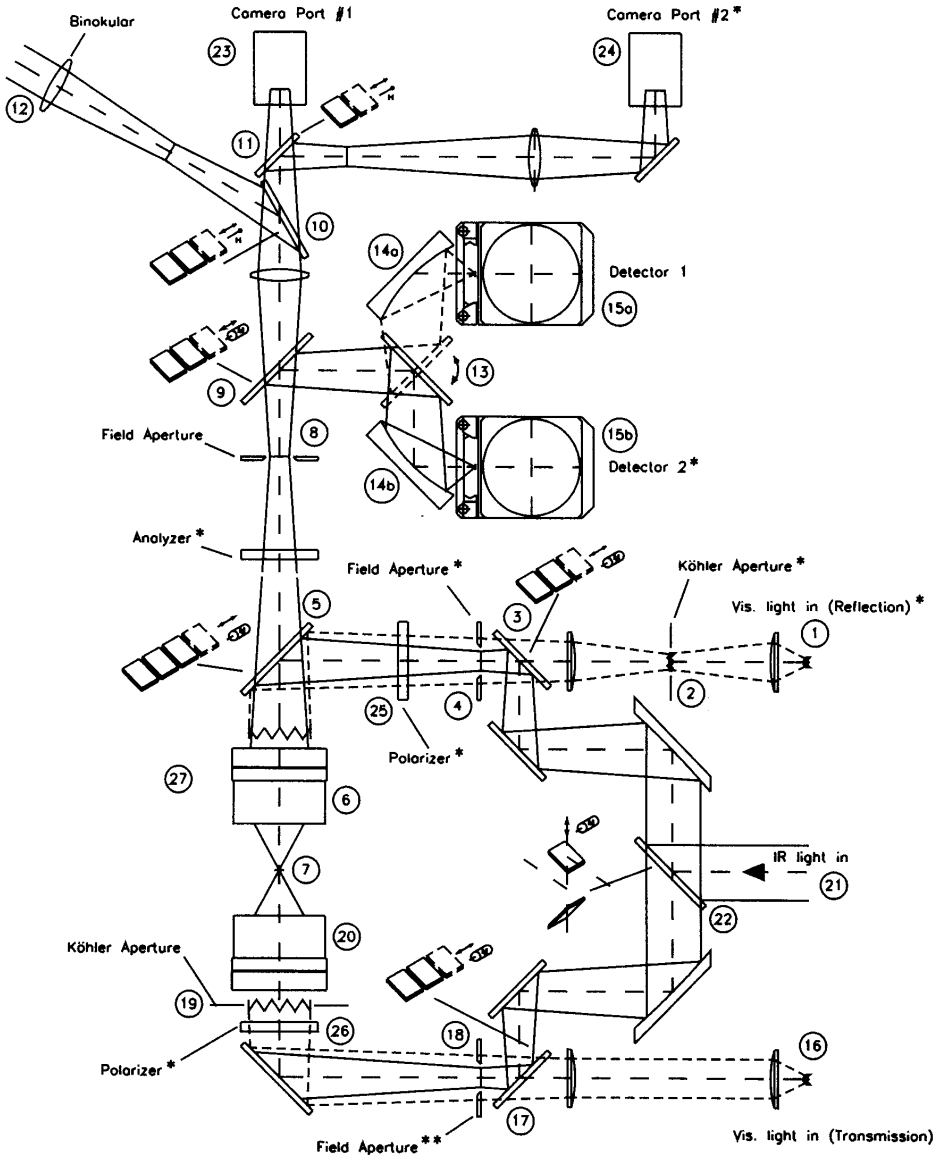

Figure 3.4: Optical path diagram of Bruker IRscope II.
1,16-visible light source; 2,19- visible light aperture; 3,22- motorized switch mirror; 4,18-optional iris or knife edge aperture; 5,9,10,17- beamsplitter changer; 6- Objective lens; 7-Sample; 8- Iris or knife edge aperture which defines the area of sample analyzed; 12- binocular eyepiece; 13- two position detector selection mirror; 14- mirror routing to detector; 15- detector; 20- condenser; 21- IR beam (from spectrometer); 23,24-camera port; 25,26,27-polarizer.

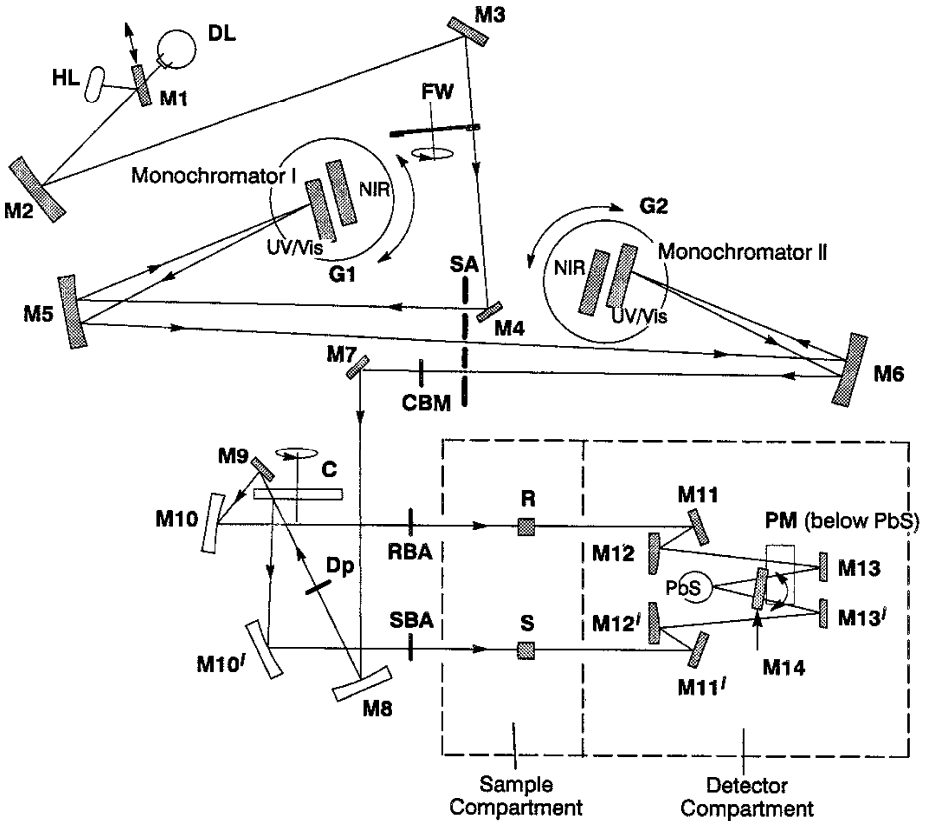

Figure 3.5: Optical layout of Perkin-Elmer λ-900

ically in Fig. 3.5.

There are two radiation sources, a deuterium lamp and a halogen lamp. Halogen lamp is used for near-infrared and visible range, and deuterium lamp is used for ultraviolet range. Source change is controlled by flipping mirror M1. The radiation of source is reflected by mirror M2, M3, and passes optical filter FW. Then, the beam is brought in monochromator I through M4, slit SA, and M5. Depending on the desired wavelength range, the collimated radiation beam strikes either the 2400 lines/mm grating or the 1200 lines/mm grating. The rotation position of the grating effectively selects a segment of the spectrum, reflecting this segment to mirror M5, to go through the exit slit, and enter Monochromator II. The advantage of the double-monochrometer is to maintain high spectral purity with an extremely low stray radiation content. The

Table 3.4: λ-900 operating parameters

Range (cm^{-1})	polarizer	Source	Monochromator	Detector
3100-14250	Glan-Thompson prism	Halogen Lamp	1200 lines/mm	PbS
11240-31330	Glan-Thompson prism	Halogen Lamp	1200 lines/mm	Photomultiplier
31330-52000	Glan-Taylor prism	Deuterium Lamp	2400 lines/mm	Photomultiplier

automatic grating change during monochromator slewing avoids the time-consuming re-alignment of the optics pathway due to themonochromator change.

The double beam is achieved via the chopper assembly C. As the chopper rotates, a mirror segment, a window segment and two dark segments are brought alternately into the radiation beam. When a window segment enters the beam, radiation passes through to mirror M9 and is then reflected via mirror M10 to create the reference beam (R). When a mirror segment enters the beam, the radiation is reflected via mirror M10′ to form the sample beam (S). When a dark segment is in the beam path, no radiation reaches the detector, permitting the detector to create the dark signal (D). Then, the measured spectrum is expressed as

$$spectrum = (S - D)/(R - D).$$

Two detectors are used in the Perkin-Elmer λ-900 spectrometer. A lead sulfide (PbS) detector is used in the near-infrared range while a photomulitplier (PM) is used in the Ultraviolet/Visible range. Detector change is automatic by rotating mirror M14 during scans.

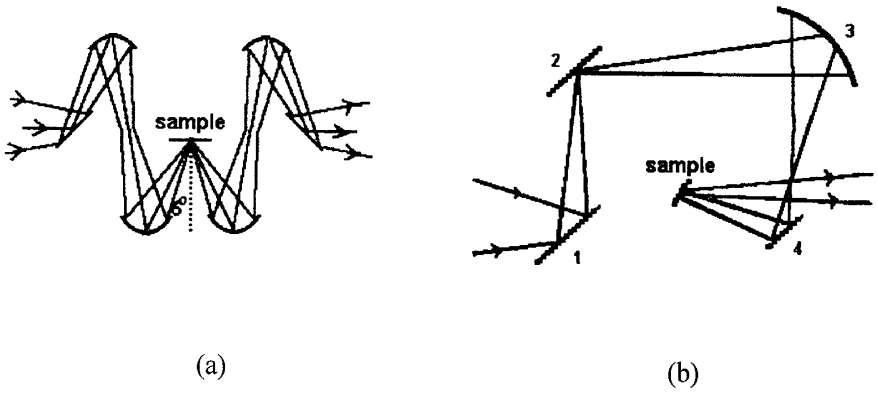

Figure 3.6: Reflectance set-up for (a) Bruker IFS 113v FTIR and (b) Perkin-Elmer λ-900

3.2.4 Reflectance Stages

To measure the absolute reflectance spectrum, a reflectance stage (as shown in Fig. 3.6) is used to bring the near normal incidence ($< 6°$) light to a solid sample or reference mirror. [104] An aluminum mirror is usually used as a reference material to obtain a baseline scan, then the reflectance spectrum of the sample is measured relative to the baseline. The absolute reflectance spectrum of the sample is obtained by renormalizing the measured spectrum with absolute Al mirror reflectance.

Anisotropic materials and polarizers

The optical theory outlined in Section 3.1 is based on Maxwell's equations 3.1–3.4 and Eqs. 3.5–3.7. The Eqs. 3.5– 3.7 are the material equations for an isotropic medium. In an anisotropic crystal, $\vec{D}$ and $\vec{E}$ are related by the following form:

$$D_x = \epsilon_{xx}E_x + \epsilon_{xy}E_y + \epsilon_{xz}E_z, \tag{3.36}$$

$$D_y = \epsilon_{xy}E_x + \epsilon_{yy}E_y + \epsilon_{yz}E_z, \tag{3.37}$$

$$D_z = \epsilon_{zx}E_x + \epsilon_{zy}E_y + \epsilon_{zz}E_z. \tag{3.38}$$

The nine qualities ϵ_{xx} ϵ_{xy}, ...are constants of the medium, and constitute the dielectric tensor. It is always possible to find a set of axes, *the principle dielectric axes*, such that the complex dielectric tensor can be put into diagonal form, i.e.,

$$\epsilon(q,\omega) = \begin{vmatrix} \epsilon_{xx} & 0 & 0 \\ 0 & \epsilon_{yy} & 0 \\ 0 & 0 & \epsilon_{zz} \end{vmatrix}. \tag{3.39}$$

Along the principle axes, $\vec{D}$ and $\vec{E}$ have the same directions. Since the dielectric tensor varies with frequency, the directions of the principal axes may also vary with frequency. This dispersion of the axes can arise only in crystals with monoclinic and triclinic symmetry. In the reflectance experiment on single crystals, the principal axes can be determined by considering the crystal shape and measuring the polarization dependence of the reflectance response.

To find the dielectric tensor along the principle axes of the single crystals, a polarized electric field of the light $\vec{E}$ is required. The polarized light is obtained by inserting a polarizer in the path of the beam. Several polarizers are used to cover the spectral range from far-infrared to ultraviolet. In the infrared, the polarizers used are made of a gold wire grid, vapor-deposited on polyethlylene (far-infrared) or silver bromide substrates. A set of plastic Polariod film polarizers are used for the infrared microscope. In the near-infrared/visible/ultraviolet range, dichroic Glan-Thompson and Glan-Taylor polarizers are used for Perkin-Elmer λ-900.

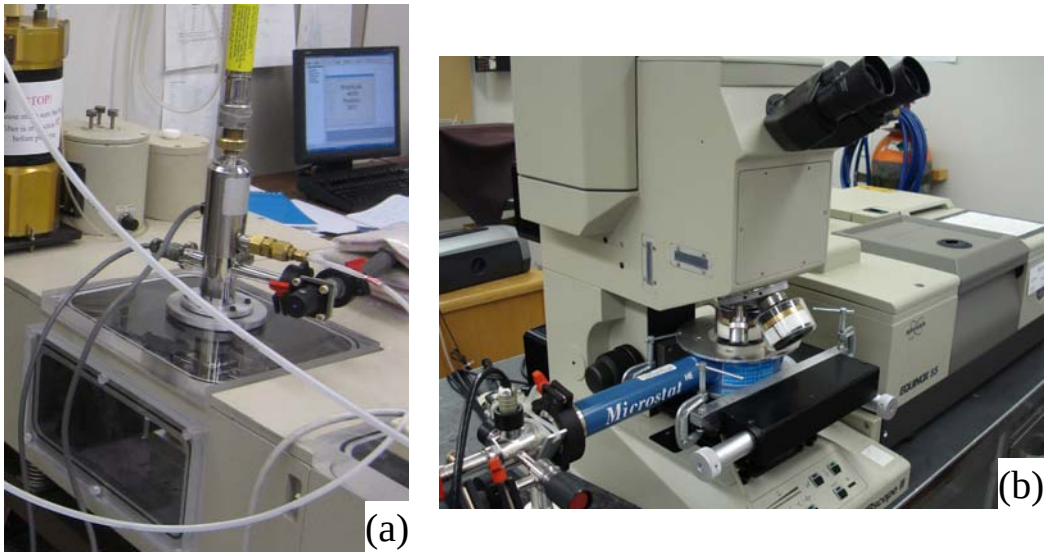

Figure 3.7: (a) and (b) Close-up views of the cryostats mounted for optical measurements in Bruker IFS 113v and Bruker Equinox 55, respectively.

3.3 Spectra under Extreme Conditions: Low Temperature and High-Field Measurements

3.3.1 Low-Temperature Techniques

The low-temperature measurements were carried out with an open-flow cryostat. The low-temperature experiments with the Bruker IFS 113v and Perkin-Elmer λ-900 are performed in combination with an APD LT-3-110 Heli-Tran cryostat system with dual temperature sensors and a Lakeshore Model 330 temperature controller. Measurements with the Bruker Equinox 55 are made with Oxford Instruments Microstat He (Fig. 3.7).

The principles of operation are illustrated in Fig.3.8. Cooling is accomplished by a controlled liquid He transfer through a high efficient transfer line to a heat exchanger adjacent to the sample interface. A needle valve at the end of the transfer line permits precise control of the flow rate. The cooling rate can be regulated by changing the pressure of the supply dewar, adjusting the flowmeter, and optimizing the position of the needle valve. It often takes about 25 minutes to precool the system, and the lowest stable temperature obtained is ~ 5 K.

To improve the thermal contact, crycon grease is placed between the cold stage of the cryostat and the sample holder, and the sample is mounted on the sample holder with GE Varnish and silver paste. There are two thermal sensors inside the cryostat, one is embedded in the tip of the cold stage, the other one is mounted on the sample holder. In this configuration, the temperatures provided by the two sensors allow us to estimate the real sample temperature.

3.3.2 Experimental Set-up at the NHMFL

The National High Magnetic Field Laboratory (NHMFL) provides a great opportunity to do magnet-related research. Different kinds of magnets including superconducting, resistive, hybrid and pulsed magnets are built at NHMFL (Fig. 3.9). The world record magnets and magneto-optics facilities at NHMFL make it possible to investigate the unusual nature of low-dimensional solids in very high magnetic fields. For more information, visit the website of NHMFL at *http://www.nhmfl.gov*.

Figure 3.10 shows a schematic of the optical set-up for the transmission measurement in the 35 T resistive magnet. For the measurement in the near-infrared/visible/ultraviolet range, a MacPherson 0.75m single grating monochrometer/spectrometer with a CCD or InGaAs detector is used to cover the energy range from 300-1600 nm (0.77-4.13 eV). The light beam is transferred in and out of the probe by red (370-2000 nm) or blue (300-

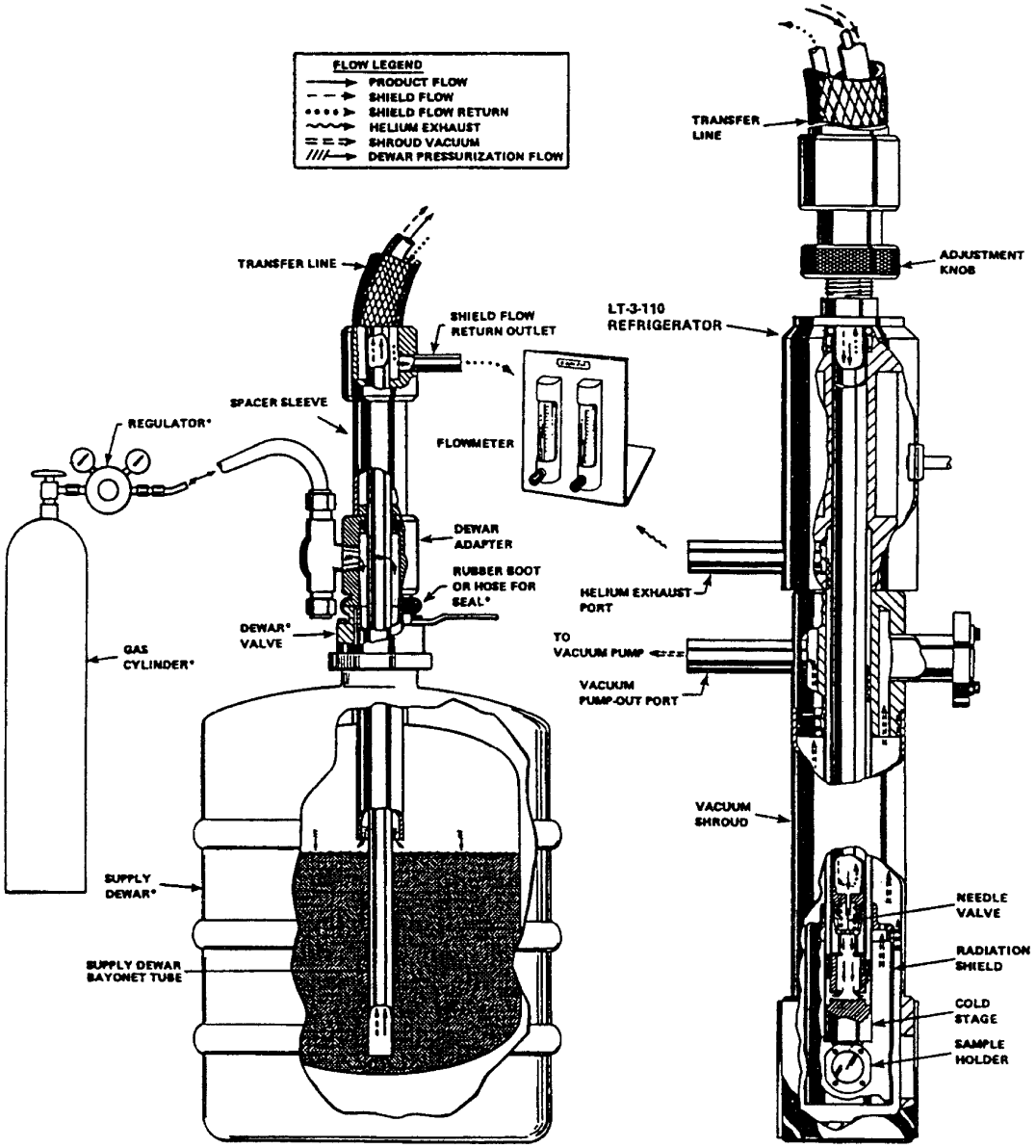

Figure 3.8: Set-up of LT-3-110 Heli-Tran liquid transfer line and cryostat.

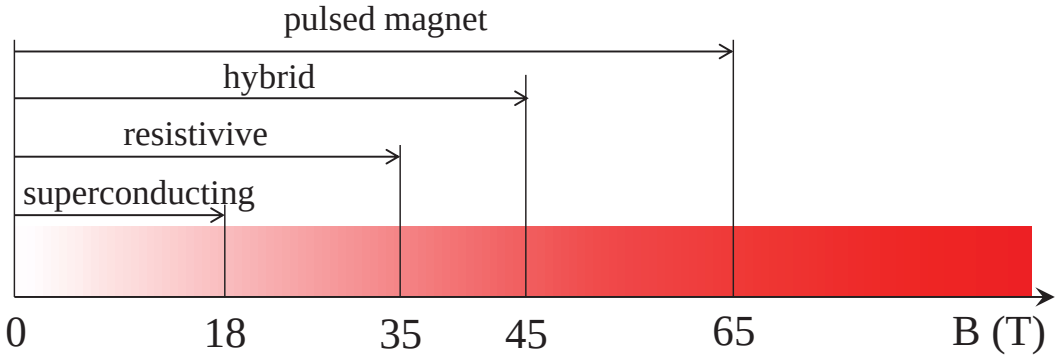

Figure 3.9: A schematic energy scale of various magnets (superconducting, resistive, hybrid, and pulsed magnets) at NHMFL.

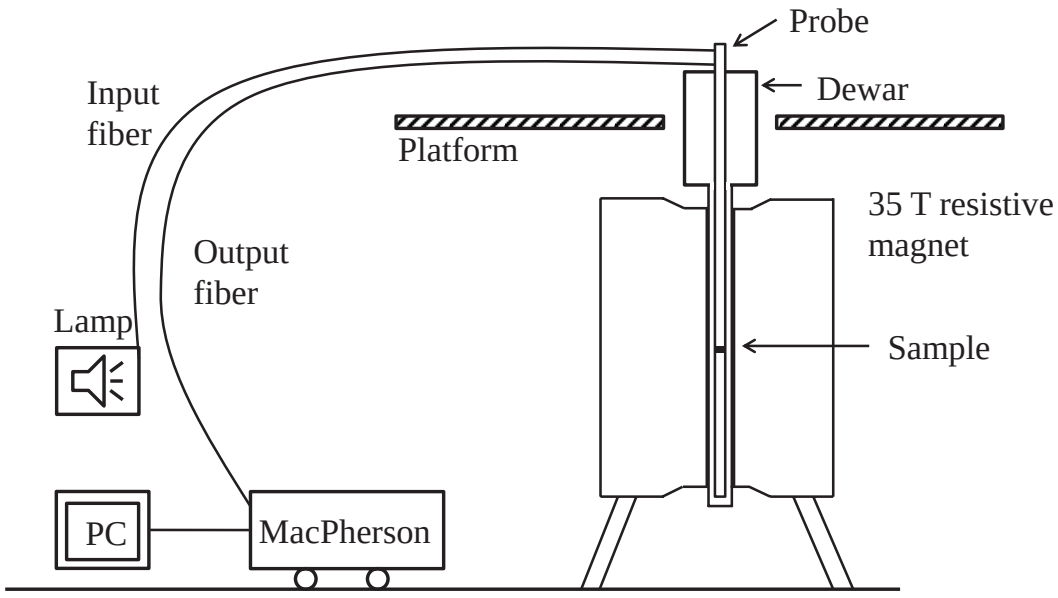

Figure 3.10: A schematic of optical set-up in the resistive magnet at NHMFL.

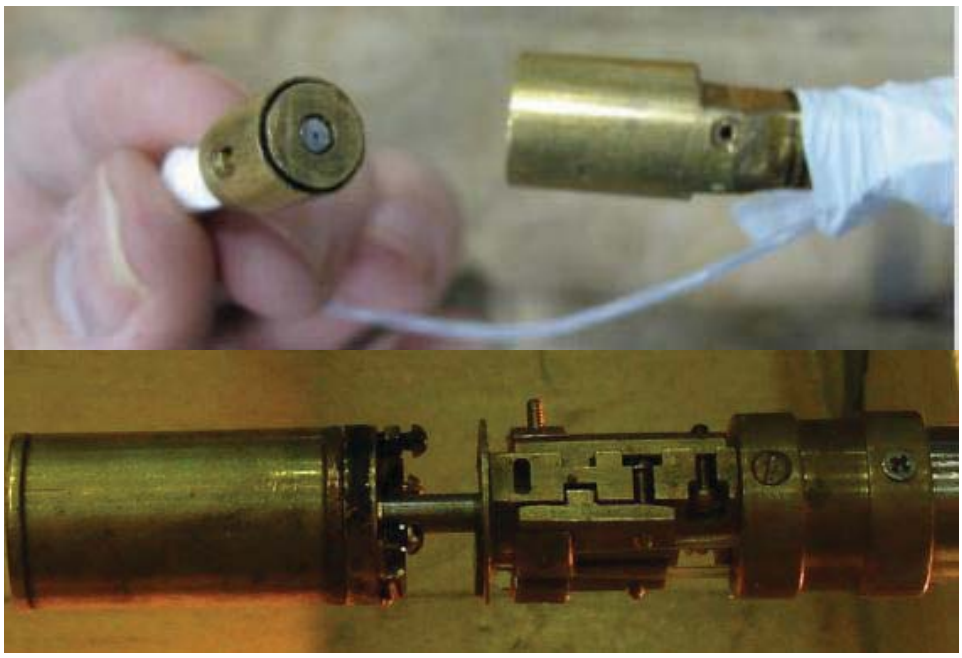

Figure 3.11: The photos of the transmittance (top) and reflectance (bottom) probe tip.

700 nm) optical fibers. Depending on the desired wavelength range and resolution, a series of gratings (150 g/mm, 300 g/mm, 600 g/mm, 1200 g/mm, and 1800 g/mm) can be used. 150 g/mm grating gives the highest light intensity and the broadest coverage, but the lowest resolution. Similar set-up can be used for the reflectance measurement with a different type of probe. Figure 3.11 displays the photos of the transmittance and reflectance probe tip used in the magnet. The probe has to be carefully positioned in the cryostat so that the sample is at the field center.

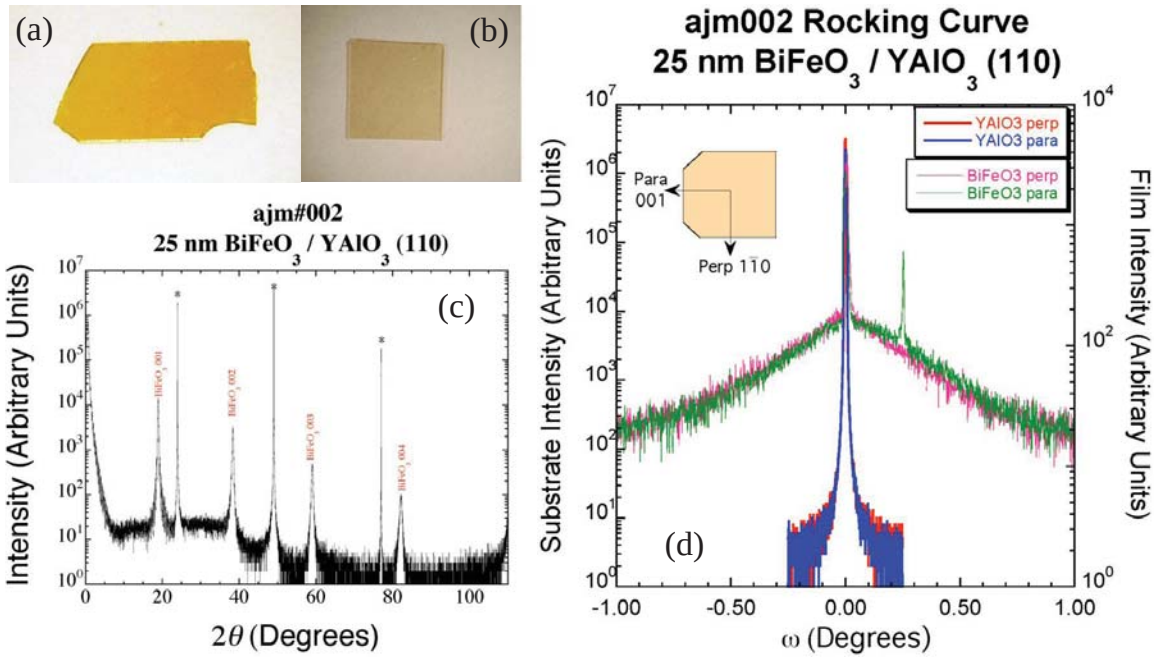

Figure 3.12: Photos of (a) rhombohedral and (b) tetragonal films. (c) The x-ray diffraction data shows only substrate and film peaks, and (d) the rocking curve shows partial relaxation with a FWHM that is virtually the same as the substrate. These results indicate good quality (in terms of screw and dislocation defects) and phase purity of this sample. (after Ref. [105])

3.4 Materials of Interest: Measurements and Complementary Calculations

3.4.1 Tetragonal $BiFeO_3$ film

Film growth

Epitaxial tetragonal $BiFeO_3$ films were grown by Darrell G. Schlom's team at Cornell University and Ramamoorthy Ramesh's group at University of California, Berkeley. A series of films with thicknesses between 23 and 38 nm were deposited on (110) $YAlO_3$ substrates using laser molecular-beam epitaxy and pulsed laser deposition. [24] X-ray results show these films have a c/a ratio of 1.27 (Fig. 3.12).

Transmittance and reflectance measurements

Room temperature transmittance and reflectance spectra were collected using a Perkin-Elmer Lambda-900 spectrometer (3000 – 190 nm; 0.41 – 6.53 eV). The spectral resolution was 1 nm in the whole range. Aluminum mirrors were used as references for reflectance measurements. We calculated the absorption coefficient $\alpha(E)$ using Glover-Tinkham analysis from combined transmittance and reflectance measurements. [103] These experiments were complemented by ellipsometry studies by our collaborators. [106]

Band gap determination

The theory of energy gap determination in solids is well established. The absorption coefficient, $\alpha(E)$, consists of contributions from both the direct and the indirect band gap transitions [108], and is given by

$$\alpha(E) = \frac{A}{E}(E - E_{g,dir})^{\frac{1}{2}} + \frac{B}{E}(E - E_{g,indir} \mp E_{ph})^2, \tag{3.40}$$

where $E_{g,dir}$ and $E_{g,ind}$ are the magnitude of direct and indirect gaps, respectively, E_{ph} is the emitted (absorbed) phonon energy, and A and B are constants. The precise profile assumes a simple band shape and may not be exactly followed in a material with complex band structure. The direct energy gap can be extracted by plotting $(\alpha \cdot E)^2$ as a function of photon energy (E). And the indirect energy gap can be extracted by plotting $(\alpha \cdot E)^{0.5}$ as a function of photon energy (E).

3.4.2 $BiFeO_3$ nanoparticles

Nanoparticle growth

Single-crystalline $BiFeO_3$ nanoparticles were provided by Stanislaus S. Wong's group at Stony Brook. They were prepared by sol-gel techniques as described by Park *et al.* [109]. In a typical synthesis of $BiFeO_3$ nanoparticles, 5 mmol of $Bi(NO_3)_3{\cdot}5H_2O$ and $Fe(NO_3)_3{\cdot}9H_2O$ was added successively to 12 ml of ethylene glycol. The mixture was stirred at 80 °C, after which a yellow-brown sol was recovered upon evaporation of the excess ethylene glycol. Thereafter, the resultant gel samples were preheated to 400 °C in three separate runs at a ramp-rate of 5 °C/min in order to remove excess hydrocarbons and NO_x impurities. To obtain reasonable size variation, samples were further annealed at 400, 425, 460, 595, 635, and 800 °C for 30 minutes, respectively. The purity and crystallinity of as-prepared $BiFeO_3$ nanoparticles were examined by X-ray powder diffraction measurements, as shown in Fig. 3.13. [109]

Transmittance measurements

The $BiFeO_3$ nanoparticles were mixed with paraffin or KBr to form isotropic composites appropriate for transmittance experiments. The compounds were evenly suspended in the matrix. Different loading levels ($\sim$0.01 - 1% by volume) were employed as needed to obtain optimum sensitivity over the full energy range of our investigation. The far infrared transmittance spectra were measured with a Bruker 113V Fourier transform infrared spectrometer. The near-infrared, visible, and near-ultraviolet spectra were measured with a modified Perkin-Elmer λ-900 spectrometer. Spectral resolution is 1 cm^{-1} in the infrared range and 2 nm in the near-infrared, visible, and near-ultraviolet. The absorption spectrum was calculated from the transmittance as $\alpha(\omega) = -\frac{1}{d} ln T(\omega)$, where d is the pellet effective thickness.

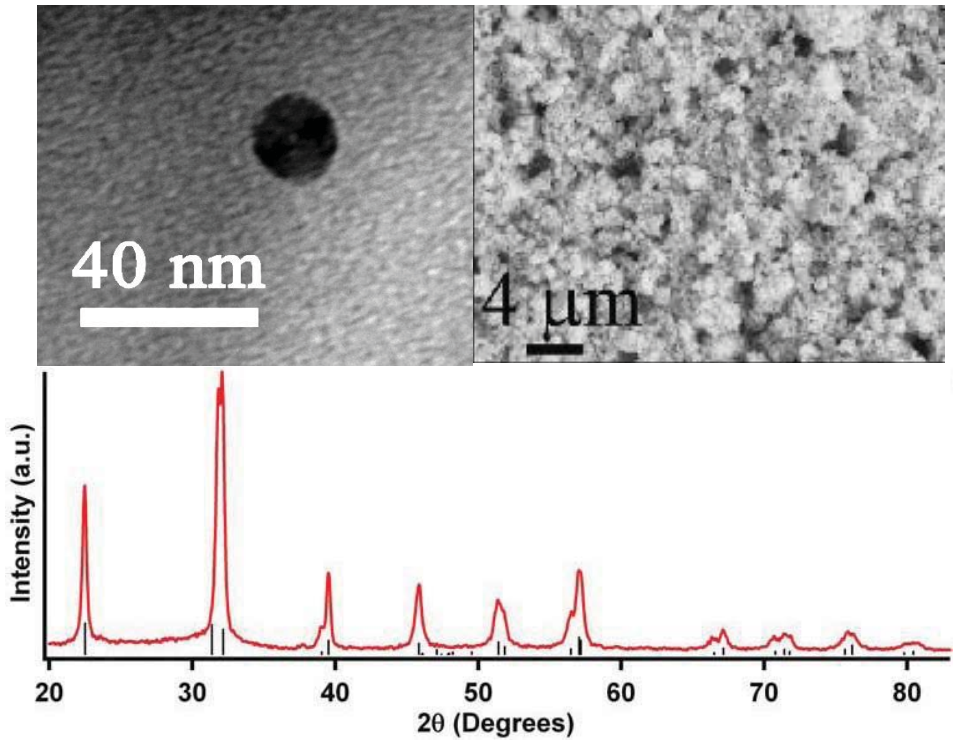

Figure 3.13: (Top left) transmission electron microscopy (top right) Scanning electron microscopy images of the 16 nm $BiFeO_3$ nanoparticles annealed at 400 °C. (bottom) A representative x-ray diffraction pattern (red) of 16 nm nanoparticles with the corresponding JCPDS standard (black) for bismuth ferrite (JCPDS #20-0169) shown immediately below.(after Ref. [10])

Lattice dynamical calculations

Lattice dynamical calculations were performed based on a real-space summation involving a spherical cutoff boundary and Coulomb potential between Fe and O ions with nominal valencies. This method is validated by simulations of crystals, liquids, and interfacial systems. [110] We calculated zone-center phonon mode frequencies in the ferroelectric $R3c$ phase of $BiFeO_3$. To allow the structure to change smoothly from the $R3c$ rhombohedral symmetry of bulk $BiFeO_3$ to the $Pm\bar{3}m$ cubic symmetry, we use a single cubic unit cell and calculated the zone center + zone boundary k = (111) modes in $Pm\bar{3}m$ phase. The results can be compared with the group theory predictions.

3.4.3 $Bi_{1-x}Nd_xFeO_3$ polycrystals

Preparation of doped materials

Polycrystalline $Bi_{1-x}Nd_xFeO_3$ were synthesized in Sang-Wook Cheong's group at Rutgers University. A series of ceramics with $x = 0$, 0.03, 0.07, 0.09, 0.10, 0.15, and 0.20 was prepared by the solid-state sintering route from Fe_2O_3, Bi_2O_3, and Nd_2O_3. [111]

Transmittance measurements

The spectra were measured with a Bruker Equinox 55 Fourier transform infrared spectrometer coupled with a Bruker IR Scope II. The near-infrared, visible, and near-ultraviolet spectra were measured with our modified Perkin-Elmer λ-900 spectrometer. Variable temperature spectroscopies were carried out between 4.2 and 300 K using an open-flow helium cryostat and temperature controller. Spectral resolution is 1 cm^{-1} in the near-infrared, and visible range. The absorption spectrum was calculated from the transmittance as $\alpha(\omega) = -\frac{1}{d} ln T(\omega)$, where d is the crystal thickness.

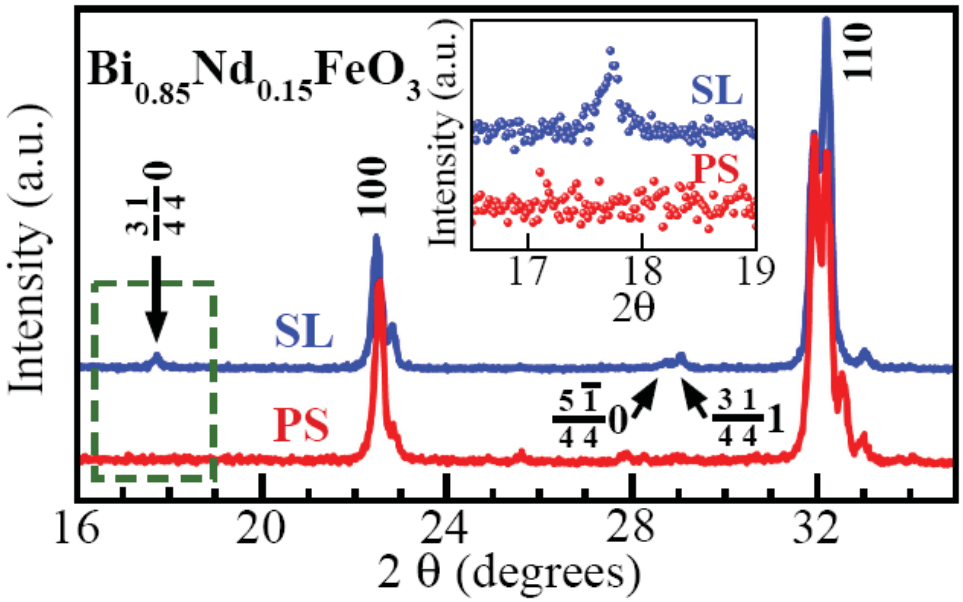

Figure 3.14: Representative x-ray diffraction patterns of $Bi_{0.85}Nd_{0.15}FeO_3$ with both primitive and superlattice structure.

Field dependent measurements

The magneto-optical properties were measured at the National High Magnetic Field Laboratory (NHMFL) in Tallahassee, FL, using a McPherson 2061A monochromator (0.84.1 eV) equipped with InGaAs, CCD detectors and a 35 T resistive magnet. The experiments were carried out between 4.2 and 90 K in the spectral range of 0.8 - 3 eV. Data were collected on both increasing and decreasing magnetic field. We focus on the 9500-11000 cm^{-1} range, a choice driven by the physics of Nd-substituted $BiFeO_3$. Absorption difference spectra were calculated as $\Delta\alpha$=[$\alpha(B)$ - α (B = 0 T)]. We identified the magnetic phase boundaries using slope discontinuities in the oscillator strength trends of the absorption difference spectra.

3.4.4 α-Fe_2O_3 single crystals

High quality α-Fe_2O_3 single crystals were grown using the flux method in Sang-Wook Cheong's group at Rutgers University. X-ray shows no impurity phases and a single

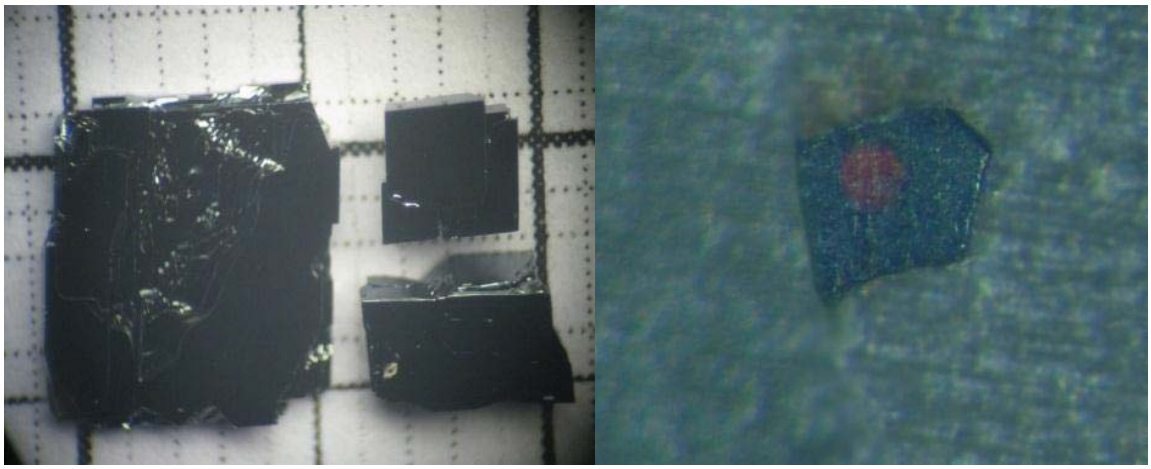

Figure 3.15: (a) Photo of representative as-grown α-Fe_2O_3 single crystals on graph paper with a 1 mm grid size. The largest crystal is $\sim 7 \times 7$ mm^2. (b) Transmittance image of a polished 18 μm thick sample with a (111) face. The characteristic color of α-Fe_2O_3 is observed. (after Ref. [14])

oxidation state. We employed five independent crystals of varying thicknesses and either (111) or $(\bar{1}10)$ orientation for our optical properties work. This combination allowed us to obtain complete results over the full frequency range of interest and optimal sensitivity to the small features. [14] Exciton and magnon investigations were best carried out with thicknesses > 80 μm, whereas on-site excitations were followed with thicknesses < 50 μm. The transmittance image of a polished crystal shows the dark reddish color (Fig. 3.15).

Transmittance and reflectance measurements

The spectra were measured with a Bruker Equinox 55 Fourier transform infrared spectrometer coupled a Bruker IR Scope II. Variable temperature spectroscopies were carried out between 4.2 and 300 K using an open-flow helium cryostat and temperature controller. Spectral resolution is 0.1-1 cm^{-1} in the near-infrared, and visible range. Aluminum mirrors were used as references for reflectance measurements. We calculated the absorption coefficient $\alpha(E)$ using Glover-Tinkham analysis from com-

bined transmittance and reflectance measurements. [103]

Field dependent measurements

The magneto-optical properties were measured at the National High Magnetic Field Laboratory (NHMFL) in Tallahassee, FL, using a McPherson 2061A monochromator (0.8 - 4.1 eV, B ∥[111], B ⊥ [111]).) equipped with InGaAs, CCD detectors and a 35 T resistive magnet. A series of gratings (150 g/mm, 600 g/mm, and 1200 g/mm) were used to resolve broad *d*-*d* on site band and fine structures like magnon sideband and excitons. Magnetic field was ramped by every 0.2 T step to catch the critical field for spin flop transition. The experiments were carried out at 4.2 K in the spectral range of 0.8 - 2.3 eV. Data were collected on both increasing and decreasing magnetic field. Absorption difference spectra were calculated as $\Delta\alpha$=[$\alpha(B)$ - $\alpha(B = 0\ T)$].

Density of states calculation

The magnon sideband density of states $\rho_{e-m}(\omega)$ is defined as [51]

$$\rho_{e-m}(\omega) = \sum_{\overrightarrow{k},u,v} \delta[\omega - \omega_e(-\overrightarrow{k}, u) - \omega_m(\overrightarrow{k}, v)], \tag{3.41}$$

where ω_e is the exciton frequency, ω_m is the magnon frequency, δ is the Dirac delta function, and u and v represent exciton and magnon branches, respectively. In order to compare the magnon sideband features in the spectra with predictions from this model, we calculated ρ_{e-m} using the magnon dispersion provided by Samuelsen [112]. This involved 2×10^7 sampling points evenly distributed throughout the Brillouin zone. As an approximation, we neglected the exciton dispersion. To determine the optimal exchange interaction parameters, we fit $\rho_{e-m}(\omega)$ to the σ-polarized spectrum by the least squares method: $S = \sum_{i=1}^{n}(\alpha_i(\omega) - f_i)^2$, where $\alpha_i(\omega)$ is the measured absorption coefficient, and f_i is the calculated density of states. We minimized S with 0.1 K

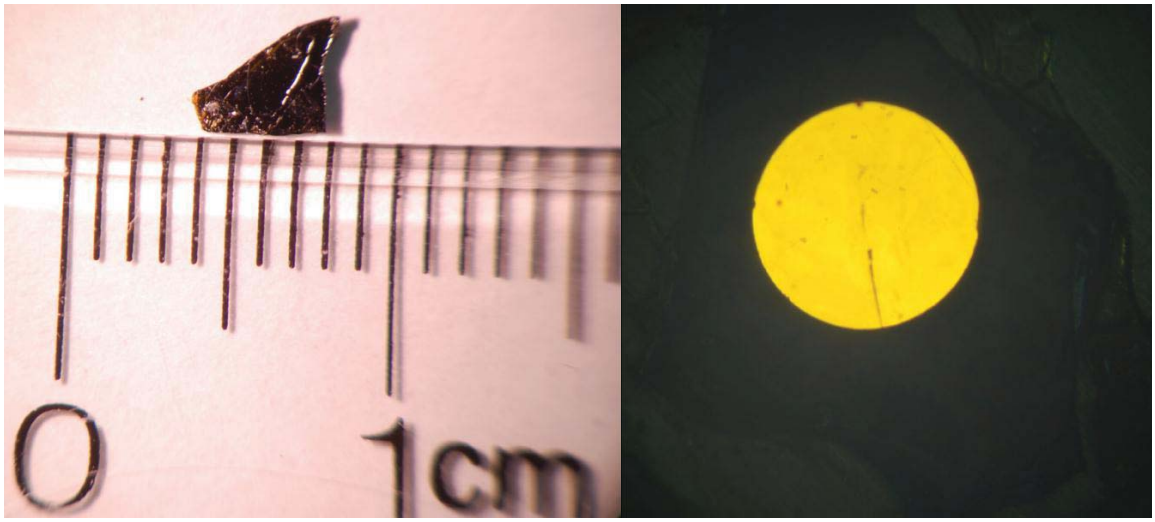

Figure 3.16: (a) Photo of representative as-grown $Ni_3V_2O_8$ single crystals on paper with a scale displayed below. The crystal is $\sim 4 \times 3$ mm^2. (b) Transmittance image of a polished 50 μm thick sample with a (001) face.

step iterations for each interaction constant. The interaction constants obtained from fitting the spectrum at 0 T are in reasonable agreement with the exchange constants from neutron scattering measurements [28], which provides a useful consistency check on this multi-variable optimization process. These same exchange constants were used to calculate the magnon density of states.

3.4.5 $Ni_3V_2O_8$ single crystals

Crystal growth

$Ni_3V_2O_8$ single crystals were grown using a BaO-V_2O_5 flux in Robert J. Cava's group at Princeton University and Bernd Lorenz's group at University of Houston. [34, 113] They were cut to expose the *ac*, *ab*, and *bc* planes and polished down to $\simeq$50 μm for transmittance measurement. The transmittance image of a polished crystal shows the yellowish color (Fig. 3.16).

Transmittance and reflectance measurements

The spectra were measured with a Bruker Equinox 55 Fourier transform infrared spectrometer coupled a Bruker IR Scope II. The near-infrared, visible, and near-ultraviolet spectra were measured using a modified Perkin-Elmer λ-900 spectrometer. Variable temperature spectroscopies were carried out between 4.2 and 300 K using an open-flow helium cryostat and temperature controller. Spectral resolution is 1 cm^{-1} in the near-infrared, and visible range. Aluminum mirrors were used as references for reflectance measurements. We calculated the absorption coefficient $\alpha(E)$ using Glover-Tinkham analysis from combined transmittance and reflectance measurements. [103]

Field dependent measurements

The magneto-optical properties were measured at the National High Magnetic Field Laboratory in Tallahassee, FL, using a McPherson 2061A monochromator (0.8 - 4.1 eV, B $\|a$, b and c axis.) equipped with InGaAs, CCD detectors and both a 35 resistive magnet and the 45 T hybrid. 150 and 600 g/mm gratings were used to resolve broad d-d on site band, charge transfer excitation edge, and excitons. Magnetic field was ramped by every 1 T step to study the spin charge coupling effect. The experiments were carried out between 1.6 K and 12 K in the spectral range of 0.8 - 2.6 eV. Data were collected on both increasing and decreasing magnetic field. Absorption difference spectra were calculated as $\Delta\alpha$=[$\alpha(B)$ - $\alpha(B = 0\ T)$]. To catch the color change in the magnetic field, we replaced the spectrometer with a black box and took pictures of the light brought in by optical fiber (1 mm diameter, 370-2000 nm) by Canon Powershot SX30 IS with a Xenon source.

Electronic structure calculations

The electronic structure calculations for $Ni_3V_2O_8$ were performed using the rotationally invariant σ-GGA+U approach as implemented in the Quantum Espresso

package [114]. The overall results are in good agreement with local density approximation (LDA)+U calculations for U=5 eV. [91] We used ultrasoft pseudopotentials [115] to describe valence-core interaction. The Ni and O pseudopotentials have been successfully used to describe the electronic structure of NiO [116]. The valence electronic configurations are $3d^9 4s^1 4p^0$, $3d^3 4s^2 4p^0$, and $2s^2 2p^4$ for Ni, V, and O, respectively. Kinetic energy cutoffs of 55 and 600 Ry were adopted for the wave function and charge density Fourier expansion. Electronic structure calculations were carried out in the primitive cell (26 atoms, Fig. 1(a), inset of the main text). Brillouin zone integrations were performed with a Marzari-Vanderbilt smearing of 0.005 Ry [117]. 12×12×9 Monkhorst and Pack special k-point grids [118] were used to evaluate the density of states and 1750 k-points were sampled for the band structure calculation. To obtain the well converged U's, we performed the computation on conventional unit cell (52 atoms) and extrapolated the result up to 416 atoms. As a first order approximation, we used collinear spin moments to compute U in antiferromagnetic state. It is a reasonable estimation because the final calculation results in collinear antiferromagnetic (AFM) and commensurate AFM states [86], which are basically the same. Computed Hubbard U's are 4.0 and 4.2 eV for Ni(c) and Ni(s), respectively [116].

3.4.6 $R\mathrm{In}_{1-x}\mathrm{Mn}_x\mathrm{O}_3$ polycrystals

Material preparation

Polycrystalline $R\mathrm{In}_{1-x}\mathrm{Mn}_x\mathrm{O}_3$ were synthesized in Sang-Wook Cheong's group from Rutgers University. A series of ceramics with R=Y, Gd, Tb, Dy and $x = 0$, 0.003, 0.01, 0.02, and 0.05 was prepared by the mixture of $\mathrm{In_2O_3}$ and rare earth oxides. The samples were polished down to $\simeq$80 μm for transmittance measurement and the transmittance images of polished samples were shown in Fig. 3.17.

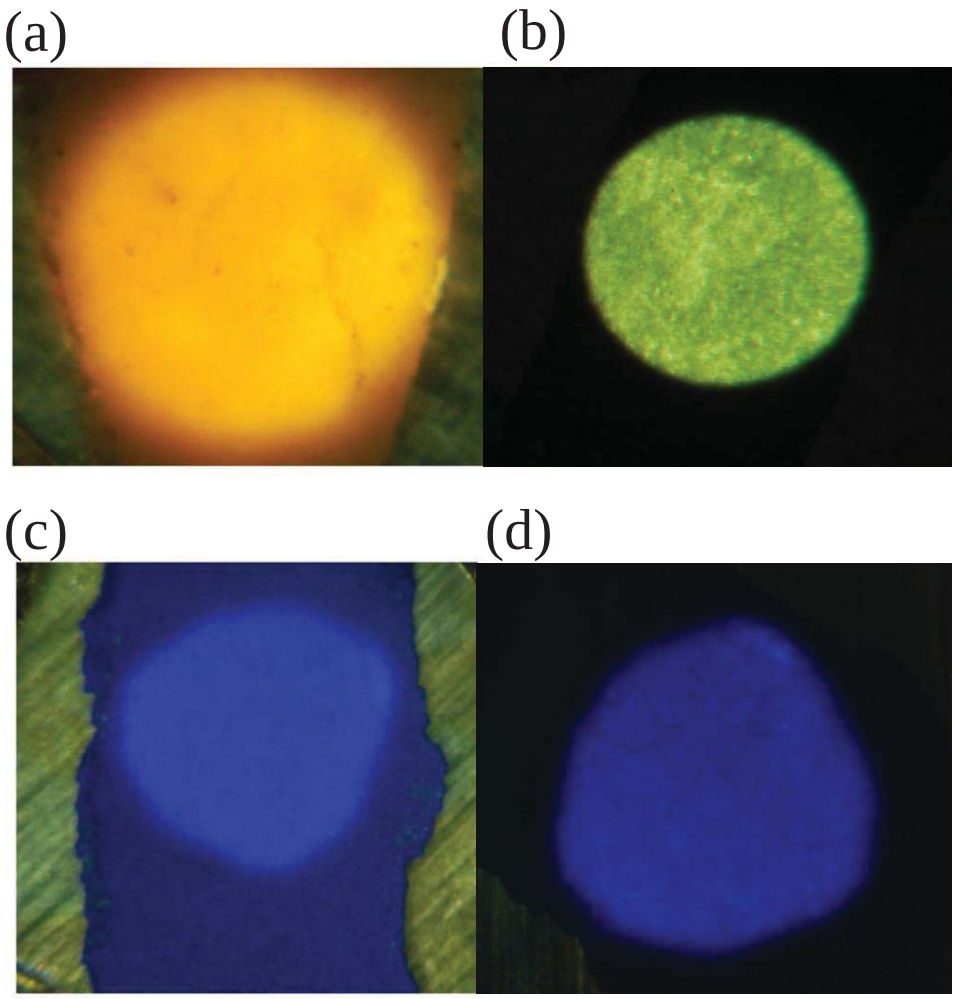

Figure 3.17: Transmittance images of polished samples: (a) $TbInO_3$, (b) $TbIn_{0.997}Mn_{0.003}O_3$, (c) $DyInO_3$, and (d) $DyIn_{0.99}Mn_{0.01}O_3$.

Transmittance measurements

We measured middle-infrared transmittance spectra with a Bruker Equinox 55 Fourier transform infrared spectrometer coupled a Bruker IR Scope II. The near-infrared, visible, and near-ultraviolet spectra were measured with our modified Perkin-Elmer λ-900 spectrometer. Spectral resolution is 1 cm^{-1} in the near-infrared, and visible range. The absorption spectrum was calculated from the transmittance as $\alpha(\omega) = -\frac{1}{d} ln T(\omega)$, where d is the crystal thickness.

Field dependent optical measurements

We measured the magneto-optical properties of $R\mathrm{In}_{1-x}\mathrm{Mn}_x\mathrm{O}_3$ at the National High Magnetic Field Laboratory in Tallahassee, FL, using a McPherson 2061A monochromator (0.8 - 4.1 eV) equipped with InGaAs, CCD detectors and both a 35 resistive magnet and the 45 T hybrid. 150 and 600 g/mm gratings were used to resolve broad d-d on site excitation and f electron excitations, respectively. Magnetic field was ramped by every 1 T step on both increasing and decreasing magnetic field to study the spin charge coupling and Zeeman effect. The experiments were carried out between 1.6 K and 100 K in the spectral range of 0.8 - 4.1 eV. Absorption difference spectra were calculated as $\Delta\alpha$=[$\alpha(B)$ - $\alpha(B = 0\ T)$]. We used a black box instead of the spectrometer to study the color change of $R\mathrm{In}_{1-x}\mathrm{Mn}_x\mathrm{O}_3$ in the field. The pictures were taken through the optical fiber (1 mm diameter, 370-2000 nm) by Canon Powershot SX30 IS with a Xenon source.

Magnetization measurements

Isothermal magnetization was measured at the NHMFL Pulsed Magnet Facility at Los Alamos National Laboratory in collaboration with John Singleton using the set-up described by Goddard *et al.* along with a 65 T short-pulse magnet. [119] Data were collected at temperatures ranging from 0.3-20 K. The magnetometers work by detecting

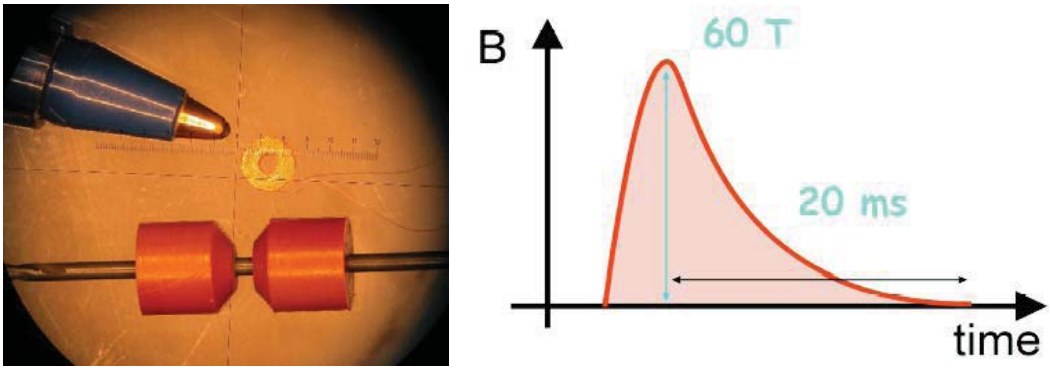

Figure 3.18: (Left) View of a 1000 turn 1 mm bore coil alongside a Bic biro for scale. Below it is the 1 mm drill plus plastic end-restraints used as a mandrel. (Right) Schematic response of the pulsed magnet.

the voltage induced in two concentric coils wound in series (the inner one being wound clockwise, the outer anticlockwise) by a changing magnetic field. The coils are designed to provide equal and opposite induced voltages, so that their combined induced voltage is zero in the absence of a sample. They are small (< 1 mm) because the cold bore of a pulsed-field magnets is small (around 7 mm in ^{3}He space). The typical time scale of pulsed magnet response is $\sim$20 ms, as shown in Fig. 3.18.

Alternating current susceptibility measurements

The alternating current susceptibility measurements were made at NHMFL Millikelvin Facility in Tallahassee, FL. The differential susceptibility was measured by means of a mutual inductance technique in the frequency range from 1 Hz to 10 KHz. Both the in-phase component $\chi^{'}$ and the out-of-phase component $\chi^{''}$ of the complex susceptibility are measured simultaneously. The ac driving field was varied between 0.1 and 0.3 Oe. The frequencies was ranging from 97 Hz to 1.4 kHz in dc fields between 0 and 2 T with temperatures between 0.5 and 1.6 K. The photo of the probe and portable dilution refrigerator used in the Millikelvin lab are shown in the Fig. 3.19.

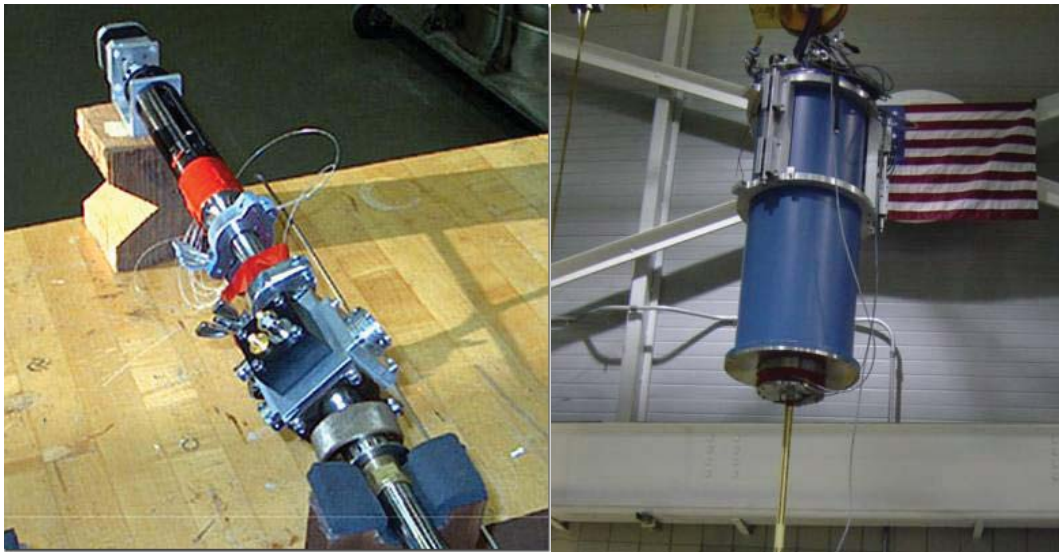

Figure 3.19: (Left) Photo of a rotating probe fit for ^{3}He refrigerator. (Right) Photo of the portable dilution refrigerator.

Chapter 4

Optical properties of $BiFeO_3$: size, structure dependence, and chemical substitution

We employed finite length effect, different lattice structure, and chemical substitution to investigate physical and chemical tuning in optical properties of $BiFeO_3$. The findings indicate that electronic and magnetic properties of $BiFeO_3$ are very flexible and can be tailored for an appropriate application in certain conditions.

4.1 Size-dependent infrared phonon modes in $BiFeO_3$ nanoparticles: probing ferroelectric phase transition

We combine infrared spectroscopy with group theory and lattice dynamics calculations to reveal the displacive nature of the ferroelectric transition in $BiFeO_3$. Systematic intensity and frequency trends in selected vibrational modes show that the paraelectric

phase is $Pm\bar{3}m$ and the lowest frequency A_1 feature is the soft mode that drives the first order transition.

4.1.1 Group theoretical analysis

Group theory predicts that $BiFeO_3$ in the $R3c$ space group should display the following optical phonon modes:

$$\Gamma(R3c) = 4\mathrm{A}_1^{\mathrm{IR,R}} \oplus 9\mathrm{E}^{\mathrm{IR,R}} \oplus 5\mathrm{A}_2.$$

The A_1 and E modes are both infrared (IR) and Raman (R) active, whereas the A_2 modes are silent. Here, the singly-degenerate A_1 modes are z-directed, and the doubly-degenerate E modes are xy-plane polarized [120, 121]. We consider two candidate paraelectric phases [27]. The first is an ideal perovskite with cubic ($Pm\bar{3}m$) symmetry. This paraelectric phase presents three triply-degenerate infrared active modes and one triply-degenerate silent mode [121]:

$$\Gamma(Pm\bar{3}m) = 3\mathrm{F}_{1\mathrm{u}}^{\mathrm{IR}} \oplus \mathrm{F}_{2\mathrm{u}}.$$

The second candidate paraelectric phase has $R\bar{3}c$ symmetry. Group theory predicts infrared-active A_{2u} and E_u features along with additional Raman-active and inactive modes:

$$\Gamma(R\bar{3}c) = 3\mathrm{A}_{2\mathrm{u}}^{\mathrm{IR}} \oplus 5\mathrm{E}_{\mathrm{u}}^{\mathrm{IR}} \oplus \mathrm{A}_{1\mathrm{g}}^{\mathrm{R}} \oplus 4\mathrm{E}_{\mathrm{g}}^{\mathrm{R}} \oplus 3\mathrm{A}_{2\mathrm{g}} \oplus 2\mathrm{A}_{1\mathrm{u}}.$$

Clearly, the $Pm\bar{3}m$ and $R\bar{3}c$ structures display very different symmetry characteristics. These differences can be used to identify the most probable paraelectric phase.

4.1.2 Vibrational modes in bulk and nanoparticles

Figure 4.1 displays the 300 K absorption spectrum of bulk and 16 nm $BiFeO_3$. We assign the observed vibrational excitations based on previous first principles calculations and infrared reflectance results [49, 120]. The latter [49] were carried out on a $(012)_h$ plane single crystal in reflectance mode and revealed nine E symmetry vibrational features. As summarized in Table 4.1, we observe eleven transverse optic (TO) vibrational modes in the spectrum of both bulk and nanoparticle $BiFeO_3$. The peaks assigned as E symmetry modes agree very well with those reported by Lobo *et al.* [49], and the peaks assigned as A_1 symmetry features are in reasonable agreement with calculated results [120, 122]. Striking finite length scale effects are evident in the nanoparticle response. Specifically, the A_1(TO1) mode red shifts by $\sim$10 cm^{-1}, and several E symmetry modes [E(TO1), E(TO3), E(TO7)] are strongly damped in spectrum of the 16 nm particles. With decreasing nanoparticle size, the overall spectral shape also begins to display "three band character", indicative of a size-induced approach to the paraelectric phase in small particles and in line with high temperature infrared reflectance trends [121]. Taken together, these results illustrate the impact of particle size on the vibrational properties of a model polar oxide.

4.1.3 Lattice dynamics in the paraelectric and ferroelectric phases

To understand the observed infrared activity and the consequences of that activity for the ferroelectric transition, we performed a series of lattice dynamical calculations [110]. Figure 4.2c displays the calculated zone-center phonon mode frequencies in the ferroelectric $R3c$ phase of $BiFeO_3$ compared with those of the two candidate paraelectric phases ($Pm\bar{3}m$ and $R\bar{3}c$) [27]. In order to allow structure to change smoothly from the $R3c$ rhombohedral symmetry of bulk $BiFeO_3$ to the $Pm\bar{3}m$ cu-

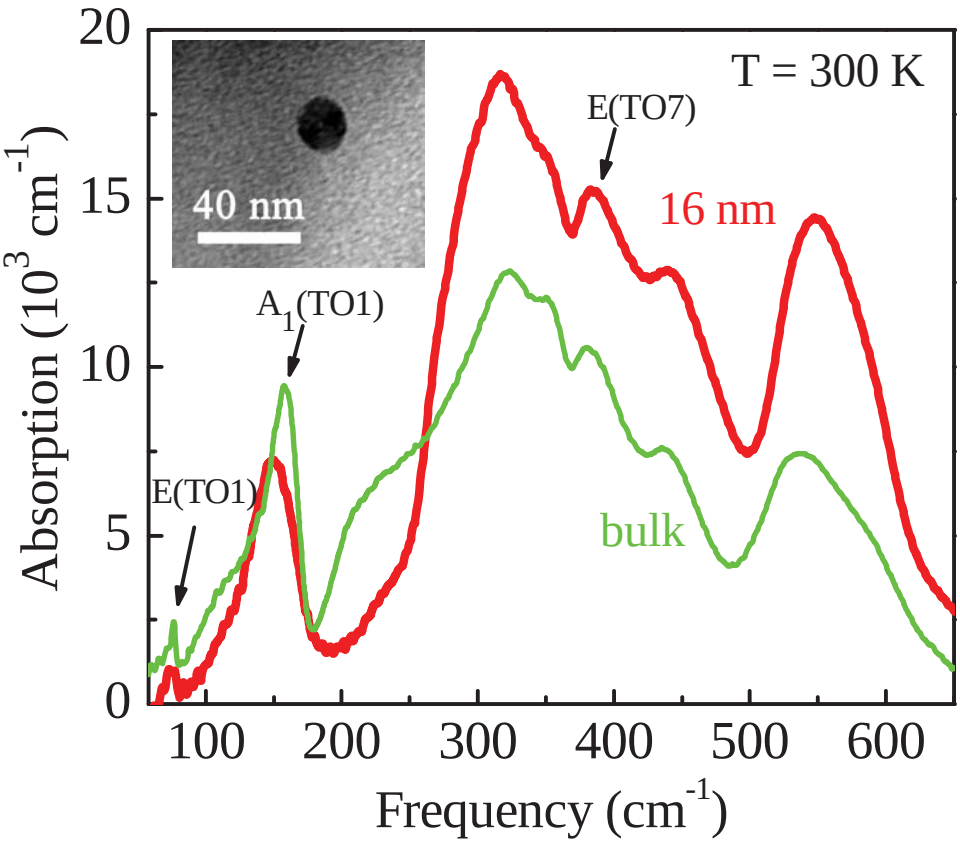

Figure 4.1: (Color online) 300 K absorption coefficient $\alpha(\omega)$ of bulk (dotted line) and 16 nm (solid line) $BiFeO_3$. The spectrum of bulk is offset by 6×10^2 cm^{-1} along the y-axis for clarity. Three modes of particular interest [E(TO1), A_1(TO1), E(TO7)] are labeled. Inset: TEM image of the 16 nm nanoparticles annealed at 400 °C. (after Ref. [10])

Table 4.1: Frequencies (cm^{-1}) and assignments of transverse optic (TO) phonon modes in $BiFeO_3$. We quantify mode softening in the nanoparticles compared to the bulk material as $\Delta\omega/\omega = (\omega_{bulk} - \omega_{nano})/\omega_{bulk}$. Calculated [120] and single crystal reflectance [49] results are shown for comparison as well.

Mode	Calc. [120]	Crystal [49]	Bulk	16 nm	$\Delta\omega/\omega$(%)
E(TO1)	102	66	76.4	77.3	-1.18
E(TO2)	152	126	114.7	113.9	0.7
A_1(TO1)	167		160.2	150.5	6.05
E(TO3)	237	240	227.6	226.2	0.62
E(TO4)	263	262			
A_1(TO2)	266				
E(TO5)	274	274	279.1	279.1	0
A_1(TO3)	318		323.8	318.7	1.58
E(TO6)	335	340	352.5	351.8	0.20
E(TO7)	378	375	384.6	385.5	-0.23
E(TO8)	409	433	441.6	444.1	-0.57
E(TO9)	509	521	531.2	536.8	-1.05
A_1(TO4)	517		580.3	575.4	0.84

bic symmetry, we use a single cubic unit cell (a = 3.87 Å) and calculated the zone center + zone boundary k = (111) modes. [123] For the $R3c$ structure, phonon polarization analysis yields four singly-degenerate and nine doubly-degenerate infrared active modes. By comparison, the $Pm\bar{3}m$ structure generates three triply-degenerate infrared active modes, whereas the $R\bar{3}c$ structure yields three singly-degenerate and five doubly-degenerate infrared active modes (Fig. 4.2c). These results are consistent with the aforementioned group theory predictions, and at the same time, they provide important information on how modes in the $R3c$ phase correlate with those in other symmetry space groups. For instance, through a hypothetical $R3c \rightarrow Pm\bar{3}m$ transition, E(TO2)+A_1(TO1), E(TO5)+A_1(TO3), and E(TO9)+A_1(TO4) combine to form three triply-degenerate infrared active modes, E(TO6) becomes inactive, and the other features develop into inactive zone boundary modes. In contrast, through a hypothetical $R3c \rightarrow R\bar{3}c$ transition, four doubly-degenerate infrared active modes [E(TO3), E(TO4), E(TO6), E(TO8)] and one singly-degenerate mode [A_1(TO4)] become Raman active. Importantly, E(TO1), E(TO7) and A_1(TO2) modes are predicted to disappear through the ferroelectric $\rightarrow Pm\bar{3}m$ paraelectric transition but remain active through the ferroelectric $\rightarrow R\bar{3}c$ transition. Moreover, A_1(TO4) will remain active in the $Pm\bar{3}m$ phase but disappear in the $R\bar{3}c$ phase. These differences provides a clear test of paraelectric phase symmetry in $BiFeO_3$.

4.1.4 Revealing nature of paramagnetic-ferromagnetic phase transition

To elucidate the paraelectric phase symmetry, we investigated the intensity of the E(TO1) and E(TO7) modes as a function of particle size [Figs. 4.3a and c]. We find that mode intensities decrease with decreasing size, disappearing almost completely in the spectrum of the 16 nm nanoparticles. Assuming spherical particles, the size-

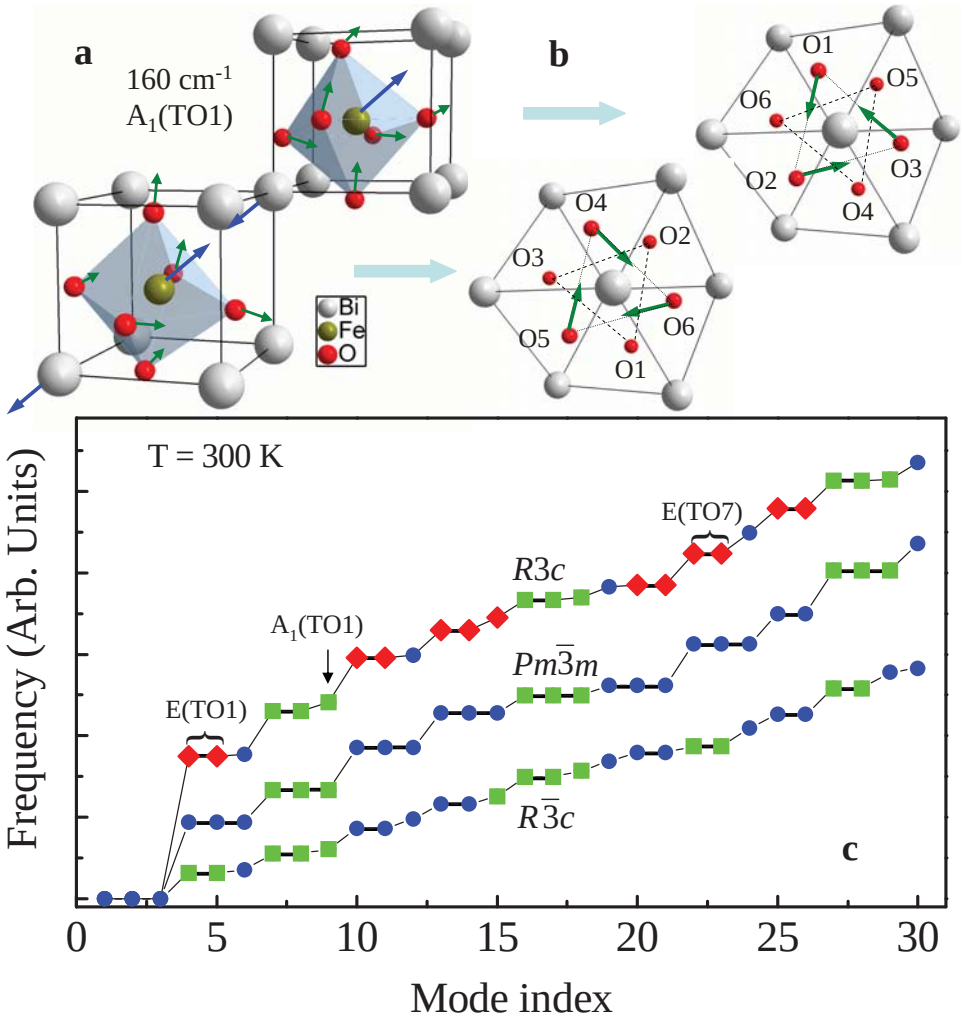

Figure 4.2: (Color online) Schematic representation of the calculated A_1(TO1) displacement vectors in rhombohedral $BiFeO_3$: (a) Bi, Fe vectors along [111] direction and (b) O vectors projected in (111) plane. (c) Calculated phonon mode frequencies for cubic ($Pm\bar{3}m$) and rhombohedral ($R\bar{3}c$) structures [27] (paraelectric phases) compared with those of the rhombohedral ($R3c$) (ferroelectric phase) system [124]. Blue dots represent acoustic and silent modes, green squares represent infrared active modes, and red diamonds mark the silent $\rightarrow$ active modes at the $Pm\bar{3}m \rightarrow R3c$ phase transition. Several modes of interest are indicated. (after Ref. [10])

dependent intensity can be expressed as a function of inverse crystallite diameter [125] as

$$I(d) = A - B/d, \tag{4.1}$$

where A, B are phenomenological constants and d is the particle diameter. To quantify finite size effects on the phonon modes of $BiFeO_3$, we calculated the relative intensities [126] of the E(TO1) and E(TO7) modes and fit the data according to equation (4.1) [Figs. 4.3b and d]. Extrapolating the curves to zero intensity, we find critical sizes (d_c) of 13.5 and 8.1 nm from our analysis of the E(TO1) and E(TO7) modes, respectively. These results are in good agreement with the 9 nm estimate of d_c from size-dependent c/a crystallographic data by Selbach *et. al.* [127]. The disappearance of E(TO1) and E(TO7) mode intensity on approach to the critical size regime combined with the presence of A_1(TO4) in the nanoparticle spectrum demonstrates that $BiFeO_3$ displays a rhombohedral $\rightarrow$ cubic distortion with decreasing particle size. Other mode behavior is reasonably consistent with group theory predictions. The paraelectric phase of $BiFeO_3$ could thus, in principle, be stabilized at room temperature with sufficiently small nanoparticles. Importantly, our findings rule out the $R\bar{3}c$ structure for the paralectric phase.

Combined group theory, dynamics, and vibrational property measurements also allow us to analyze the mechanism of the ferroelectric transition. Calculated displacement eigenvectors indicate that Bi centers participate only in the three lowest frequency modes whereas O motion dominates the higher frequency structures [120]. We focus on the A_1(TO1) vibrational mode, a feature that is significantly softened in the spectrum of the nanoparticles [Fig. 4.1, Table 4.1]. As shown in Figs. 4.2a and b, Bi cations move out-of-phase with respect to the FeO_6 octahedra along the polar direction (resulting in ferroelectricity), while the two adjacent FeO_6 octahedra counter rotate about the [111] axis (doubling the unit cell). Here, Fe cation displacements are

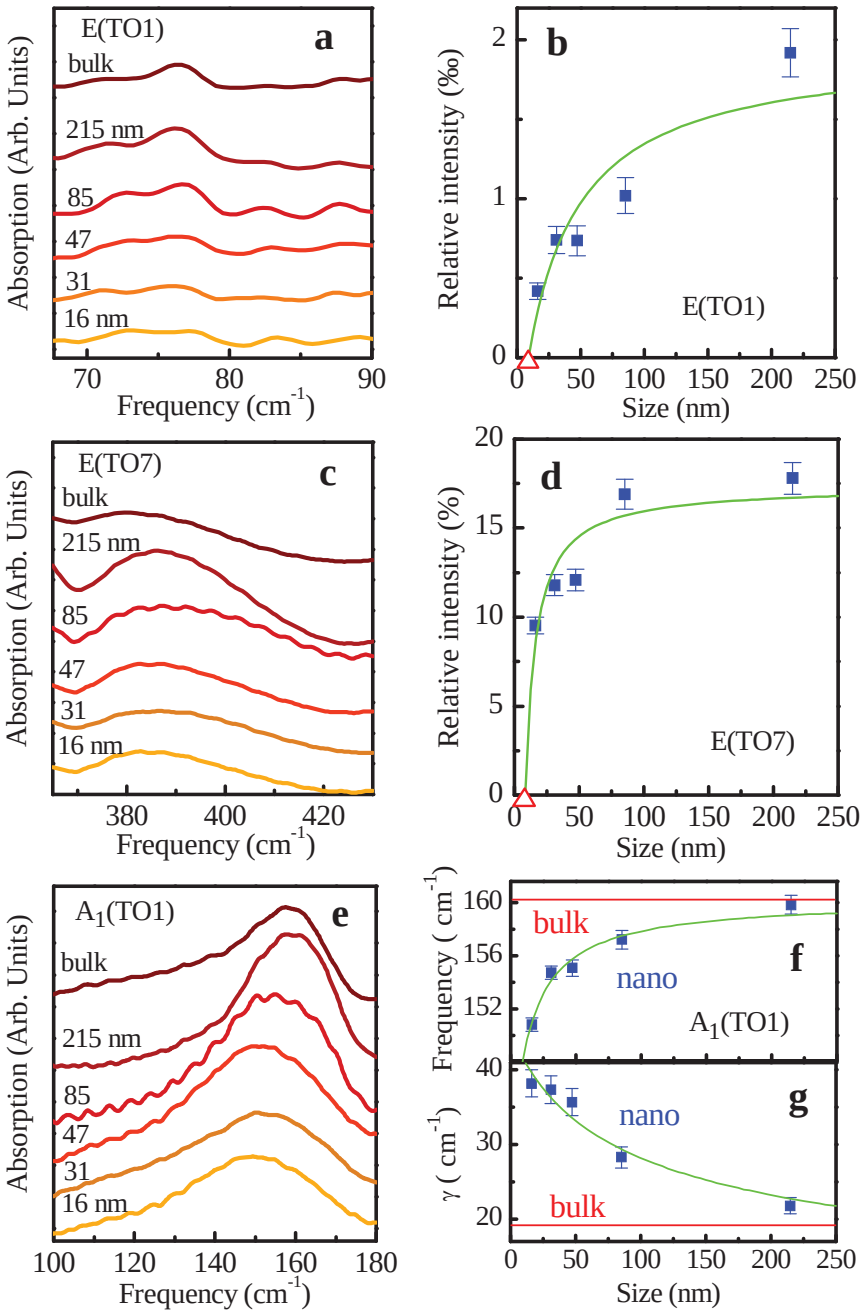

Figure 4.3: (Color online) Close-up view of selected phonon modes of $BiFeO_3$ as a function of size (diameter) at 300 K. These modes include features of (a) E(TO1), (c) E(TO7), and (e) A_1(TO1) symmetries. Important trends quantified include (b) the relative intensity of the E(TO1) mode vs. size, (d) the relative intensity of the E(TO7) mode vs. size, (f) the frequency of the A_1(TO1) mode vs. size and (g) the damping of the A_1(TO1) mode vs. size. The green solid lines are the calculated curves fit to the data, described in the text. Red triangles mark the critical size 13.5 nm and 8.1 nm for E(TO1) and E(TO7) modes respectively. (after Ref. [10])

fairly large, so they move off-center in the octahedra. These calculated results point toward a displacive phase transition mechanism [120] in which atomic displacement changes crystal symmetry [128]. We can test this prediction by searching for evidence of the displacive phonon. Figure 4.3e displays the frequency and damping constant of the A_1(TO1) mode as a function of particle size. With decreasing crystalline size, this vibrational feature softens by more than 6% and dampens considerably. The systematic red shifting of the A_1(TO1) vibrational mode with decreasing size strongly supports its assignment as the soft mode driving the ferroelectric transition. Moreover, this A_1 mode is underdamped, even in the 16 nm material, suggesting a first order nature. This result is consistent with the incomplete phonon softening in high temperature infrared [121] and Raman [129] measurements.

At a first order phase transition, the soft mode frequency varies with temperature [130, 131] as

$$\omega(d,T) - \omega_0(d,T_C(d)) = A|T_C(d) - T|^{\beta}. \tag{4.2}$$

Here, $T_C(d)$ is the Curie temperature of the nanoparticles, $\omega_0(d,T_C(d))$ is the soft mode frequency at the ferroelectric to paraelectric transition, A is a constant, and $\beta \simeq \frac{1}{3}$ is the critical exponent [130]. The variation of the transition temperature with particle size [132–135] is given by the empirical expression

$$T_C(d) = T_C(\infty) - B/(d-E), \tag{4.3}$$

where $T_C(\infty)$ is the Curie temperature of the bulk material, d is the particle size, and B and E are constants. Inserting the expression for $T_C(d)$ from equation (4.3) into equation (4.2) and incorporating temperature into the constants, we can obtain the

soft mode frequency in terms of particle size d at a specific temperature as

$$\omega(d) = \omega_0 + A'|1 - B'/(d - E)|^{\beta}. \tag{4.4}$$

Here, A' and B' are modified constants, and ω_0 is the soft mode frequency at the critical size. We also assume that $\omega_0[d, T_C(d)]$ in equation 4.2 is relatively constant across different particle sizes, a reasonable assumption since the structure of the paraelectric phase is expected to be independent of size. With the values of $\beta = 1/3$ and $\omega_0 + A'$ $= 160.23$ cm^{-1} which is the A_1(TO1) mode frequency of the bulk material (when $d = \infty$), we were able to determine constants from equation (4) by a least squares fit of the experimental data yielding the result $\omega(d) = 138.55 + 21.68|1 - 40.08/(d + 32.22)|^{1/3}$. From this expression, we find $\omega_0 = 138.55$ cm^{-1}. Notably, this soft mode frequency at the critical size is larger than zero. It is only ~16% lower than that in ferroelectric phase which is a relatively small change compared with traditional ferroelectric perovskites like $PbTiO_3$ [136], $BaTiO_3$ [137], and $SrTiO_3$ [138]. The nonzero value of $\omega(d)$ through the transition confirms the first order mechanism, and the modest displacement of the A_1(TO1) mode through the size-driven ferroelectric to paraelectric transition explains why phonon softening cannot be observed in high temperature experiments [121], where thermal expansion and disorder dominate the softening behavior. When $\omega(d) = 138.55$ cm^{-1}, we can extract a critical size ($d_c = 7.86$ nm). The latter is in excellent agreement with the values obtained from E(TO1) and E(TO7) mode intensity trends (8.1 and 13.5 nm). As a length scale, the 7.86 nm critical diameter corresponds to about 20 unit cells, which shows that the structure is highly strained. Figure 4.3g displays the damping coefficient γ as a function of particle size. Combining the relationship between γ and T_C [139] with equation (4.3), γ can be expressed as

$$\gamma(d) = A'|1 - B'/(d - C)|^{-3/8}, \tag{4.5}$$

where A', B', C are constants. This model fits the experimental data very well, as shown in the curve.

Bringing these results together, we propose that size effects in ultrafine $BiFeO_3$ particles can be understood within the soft mode picture [140] in which cubic structure dominates below d_c. To obtain the distorted ferroelectric phase, one of the TO modes with F_{1u} symmetry becomes soft and unstable. The important distortions consist of opposite polar displacements of Bi cations and FeO_6 octahedra combined with counter-rotation of adjacent FeO_6 octahedra around the [111] axis. As a consequence, the cubic symmetry transforms into rhombohedral. This transition is driven by the competition between short-range overlap and long-range Coulomb forces [140]. Surface tension δ impacts the latter. It can be expressed in terms of particle diameter as

$$\delta = Pd/4, \tag{4.6}$$

where P is the internal pressure [135]. We can estimate P from previous high pressure studies [16, 71, 72, 141] that show $BiFeO_3$ becomes metallic above 47 GPa. Employing a critical size of 7.86 nm (obtained from our frequency shift analysis of the A_1(TO1) mode which is more reliable than values determined from intensity trends), [142] we extract $\delta = 92$ N/m. Similar results are obtained in other polar oxides such as $PbTiO_3$ and $BaTiO_3$ [135].

4.2 Band gap tuning of tetragonal $BiFeO_3$ film and nanoparticles

Optical transmission spectroscopy and spectroscopic ellipsometry were used to extract the optical properties of an epitaxially grown quasi-tetragonal $BiFeO_3$ thin film.

The absorption spectrum is overall blue shifted compared with that of rhombohedral $BiFeO_3$, with a direct 3.1 eV band gap. Finite length scale effects are evident in the electronic structure with a red-shifted band gap (2.4 eV) in nanoscale $BiFeO_3$ compared with that of the rhombohedral film.

4.2.1 Optical absorption and ellipsometry measurements of rhombohedral and tetragonal $BiFeO_3$ films

Figure 4.4(a) displays the 300 K absorption spectrum of the tetragonal $BiFeO_3$ film compared with that of the rhombohedral analog. [52] We assigned the observed excitations based on recent first-principles calculations. [26, 27, 143] Although the overall absorption profiles are similar, the familiar 3.2 and 4.5 eV electronic excitations of the rhombohedral material, assigned as minority channel dipole-allowed charge transfer features, [8, 27, 52] are blue-shifted by $\sim$0.4 eV in tetragonal $BiFeO_3$. The blue shift of these strongly hybridized O p to Fe d excitations is a consequence of the strained nature of the non-equilibrium tetragonal phase. The quasi-tetragonal film displays an additional electronic feature centered at $\sim$6.2 eV that we assign as a strongly hybridized majority channel O p + Fe $d \rightarrow$ Bi p state excitation. The direct band gap is extracted by a linear extrapolation of an $(\alpha \cdot E)^2$ vs. E plot to zero [Fig. 4.4(b)]. [102] We find the band gap in tetragonal $BiFeO_3$ to be 3.10$\pm$0.02 eV, $\sim$0.4 eV larger than that in rhombohedral $BiFeO_3$ (2.67$\pm$0.02 eV). This result is different from theoretical calculations [26, 143] which predict a smaller band gap in tetragonal $BiFeO_3$. One of the probable reasons of the calculated smaller band gap in tetragonal structure is that effective on-site interaction parameter U_{eff} are different in tetragonal and rhombohedal structures. The 2.5 eV sub band gap absorption feature in the rhombohedral system [52] is also present in the tetragonal material. Figure 4.5 displays $\varepsilon_1(E)$ and $\varepsilon_2(E)$ for the quasi-tetragonal $BiFeO_3$ film compared to similar results on the rhom-

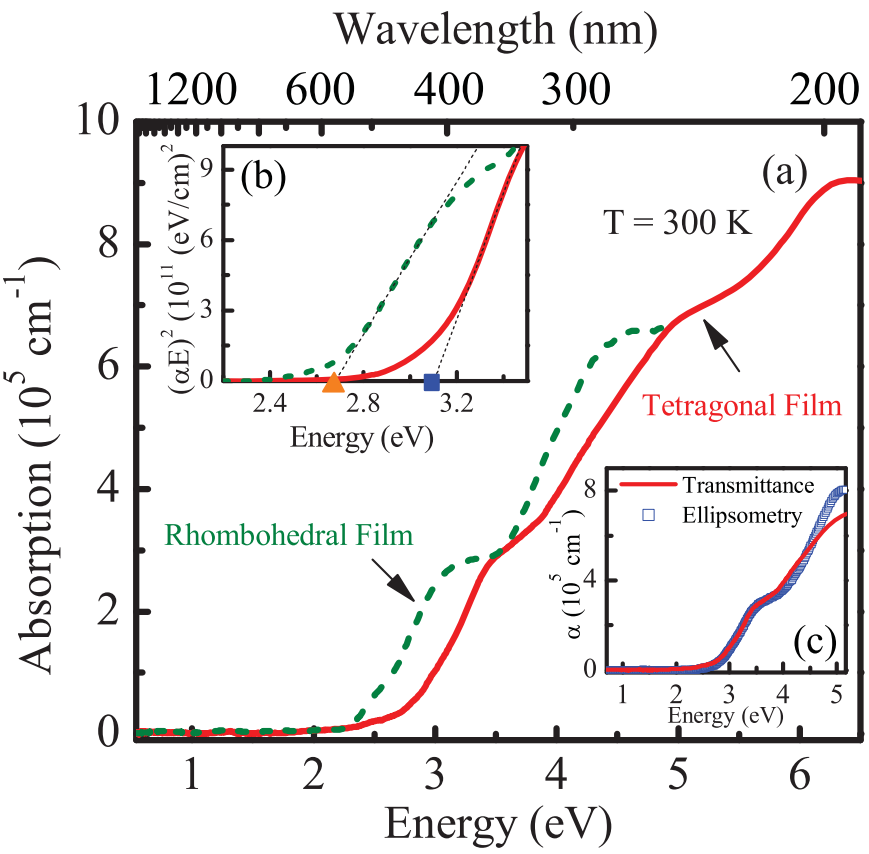

Figure 4.4: (Color online) (a) Absorption coefficient of tetragonal $BiFeO_3$ compared with that of the rhombohedral system. [52] (b) Direct band gap analysis of both materials. The (orange) triangle marks the 2.67±0.02 eV charge gap of the rhombohedral film whereas the (blue) square marks the 3.10±0.02 eV gap of tetragonal $BiFeO_3$. (c) $\alpha(E)$ obtained by optical transmittance compares well with that obtained by ellipsometry. (after Ref. [105])

bohedral material. [144] From ellipsometric results, tetragonal $BiFeO_3$ exhibits higher energy charge transfer excitations that are also broadened compared with the rhombohedral phase, a result that is overall consistent with the absorption spectra in Fig. 4.4(c).

We can also compare the optical properties of tetragonal $BiFeO_3$ with a local structure analysis [Fig. 4.6], simple crystal field theory, and first principles electronic structure calculations. [26,143] We begin by considering the FeO_6 structure in rhombohedral $BiFeO_3$ as an ideal octahedron. It is well-known that, in an octahedral crystal field,

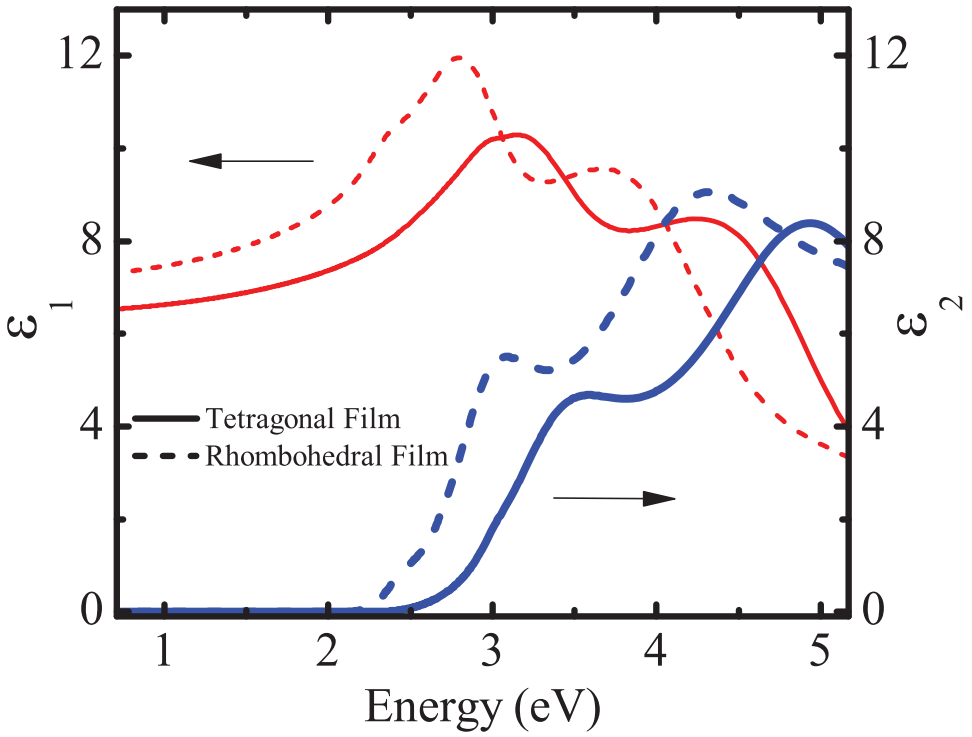

Figure 4.5: (Color online) Complex dielectric function spectra ($\varepsilon = \varepsilon_1 + i\varepsilon_2$) versus photon energy (E) obtained for tetragonal $BiFeO_3$ (solid line). ε_1(E) and ε_2(E) of rhombohedral $BiFeO_3$ (dashed line) are shown for comparison. [144] (after Ref. [105])

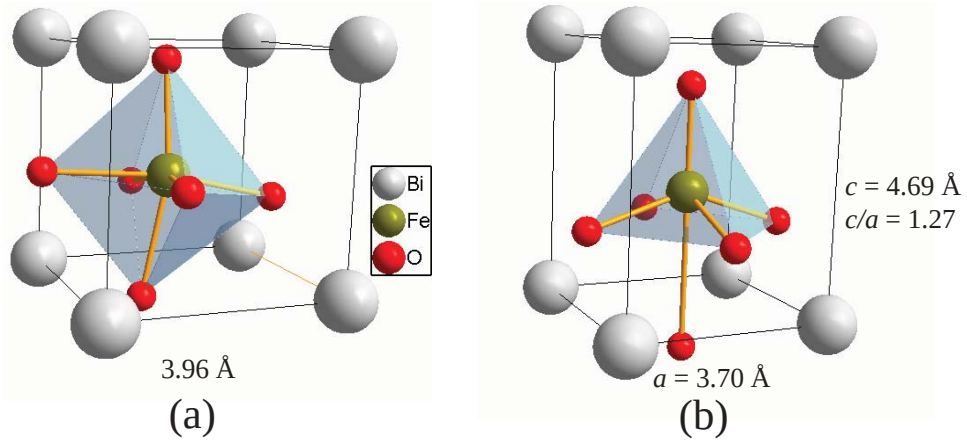

Figure 4.6: (Color online) Schematic view of the local structure around the Fe^{3+} center of (a) rhombohedral [124] and (b) tetragonal [143] $BiFeO_3$. (after Ref. [105])

the $3d$ orbital states split into t_{2g} and e_g levels. Strain has important consequences for the local structure. In tetragonal $BiFeO_3$, one of the Fe-O axial distances increases to $\sim$2.80 Å, and the Fe-O equatorial bond lengths are reduced to $\sim$1.93 Å. [143] These modifications split the t_{2g} states into a doubly-degenerate pair (d_{xz}, d_{yz}) and a singly-degenerate d_{xy} level, and the e_g states break symmetry to yield a lower energy d_{z^2} state and a higher energy $d_{x^2-y^2}$ level. The net effect is to move the empty Fe^{3+} $3d$ states closer to the occupied ones. Band structure calculations [26, 143] confirm this trend, predicting that the unoccupied Fe^{3+} $3d$ states broaden and move closer to the Fermi level in the quasi-tetragonal system. At the same time, the calculations predict that the O^{2-} $2p$ states move further away. [143] Together, these competing density of states shifts define the predicted charge gap. Based upon our measurement of a larger band gap in quasi-tetragonal $BiFeO_3$, the calculations either overestimate the shift in the Fe^{3+} $3d$ states or underestimate the shift of the O^{2-} $2p$ states.

4.2.2 Band gap of $BiFeO_3$ nanoparticles

The electronic properties of complex oxides provide fundamental information on chemical bonding, hybridization, and the interplay between charge, structure, and strain. Certainly, applied pressure induces electronic structure changes in $BiFeO_3$ through the phase transition [72]. The consequences of surface strain induced by finite size effects are of complementary importance. Figure 4.7 displays the optical absorption spectrum of the 16 nm $BiFeO_3$ nanoparticles. Compared to the response of an epitaxially grown rhombohedral thin film [52], the familiar 3.2 and 4.5 eV electronic bands, assigned as minority channel dipole-allowed charge transfer excitations [8, 27, 52] split into multiplets. For instance, the 3.2 eV band splits to reveal features centered at 2.9 and 3.4 eV. The splitting of these strongly hybridized O $2p$ to Fe $3d$ excitations is due to distortions of the FeO_6 octahedra [27, 145] that, from a local perspective, reflects the

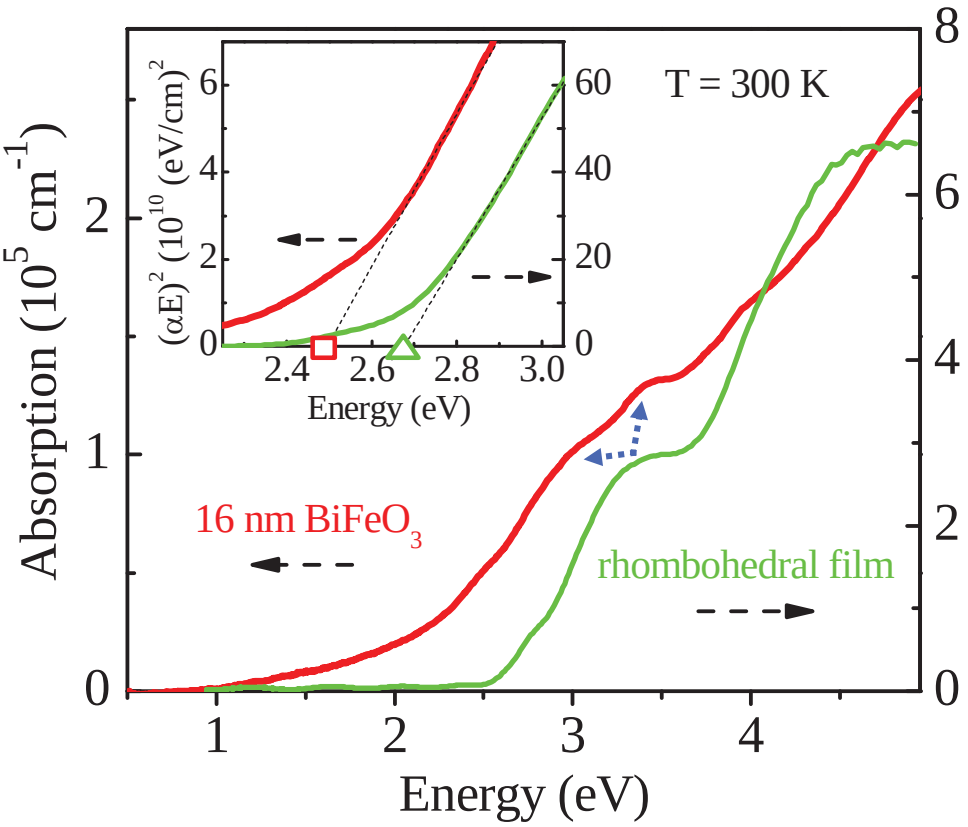

Figure 4.7: (Color online) 300 K absorption coefficient α(E) of 31 nm $BiFeO_3$ nanoparticles as compared with that of an epitaxially grown rhombohedral thin film. [52] Inset: Direct band gap analysis of the thin film and the nanoparticles. The triangle marks the 2.67±0.02 eV charge gap of the rhombohedral film whereas the square marks the 2.42±0.02 eV gap of 31 nm $BiFeO_3$. (after Ref. [10])

strained nature of small sized particles and reveals the diminished structural coherence at small particle sizes in conjunction with this tendency toward average cubic structure. [127, 146] We extract the direct band gap via a linear extrapolation of $(\alpha E)^2$ vs. E plots to zero (inset, Fig. 4.7). The gap in the nanoparticles (2.43 eV) is significantly reduced compared with that in the film (2.67 eV) [8, 52]. This is a consequence of the aforementioned splitting of the 3.2 eV charge transfer excitation due to symmetry breaking. A red shifted gap (2.5 eV) is also observed in $BiFeO_3$ nanowires [147], although tetragonal $BiFeO_3$ (stabilized by compressive strain) displays a larger 3.1 eV gap [105] that is again determined by the location of the lowest energy charge trans-

fer edge. That these are structural rather than chemical disorder-induced effects is supported by direct crystallographic studies [127] as well as our vibrational properties work that demonstrates small $BiFeO_3$ particles tend toward the cubic structure.

In principle, the gap of the nanomaterial can also be affected by quantum confinement (which scales as d^{-2}) [148]. We do not, however, expect to observe this effect here because even the smallest particle size in this experiment (16 nm) is still too large to display quantum confinement. The long near infrared tail below 2.3 eV in optical absorption spectrum of the nanoparticles is due to scattering and reflectance contributions, artifacts that can be corrected in certain cases (epitaxial thin films, single crystals) [105], but are difficult to quantify for a sample in powder form. Moreover, our experiments show no explicit size-dependent band gap for particles between 16 and 61 nm [149], indicating that the FeO_6 local structure distortion is of similar magnitude in this size range. Recent reports of photoconductivity, a photovoltaic effect, and a 0.8-0.9 V open circuit voltage combined with 10% external quantum efficiency above the band gap in a working ferroelectric solar device illustrate the potential of polar oxides like $BiFeO_3$ as active photovoltaic materials [52, 150, 151]. The optical response of the $BiFeO_3$ nanoparticles (Fig. 4.7) shows a smaller band gap and an improved match to the solar spectrum which translates into a broader active wavelength range in a photovoltaic device. It also illustrates the far-reaching potential of finite size effects for band gap modification of functional oxides.

4.3 Spin cycloid quenching in Nd-substituted $BiFeO_3$

We employ magneto-optical spectroscopy to investigate the behavior of the cycloid $\rightarrow$ homogenous (canted antiferromagnet) ordering transition in $Bi_{1-x}Nd_xFeO_3$. From the magneto-optical response, we construct a B–T–x phase diagram that shows how the critical field decreases with Nd^{3+} substitution, an effect that we model with Ginzburg-

Landau free energy and harmonic cycloid approximations. Spiral magnetic order is quenched when $x\sim0.2$. With increasing temperature (T<90 K), the critical field rises gently, a consequence of magnetic anisotropy changes with temperature.

4.3.1 Absorption spectra in near-infrared and visible range

Figure 4.8(a) displays the 4.2 K absorption spectra of $Bi_{1-x}Nd_xFeO_3$ ($0\leq x\leq0.20$). We assign the two strong bands centered at ∼11200 and 15250 cm^{-1} in the end member as ${}^6A_{1g} \rightarrow {}^4T_{1g}$ and ${}^6A_{1g} \rightarrow {}^4T_{2g}$ on-site excitations of Fe^{3+} [8, 14]. These *d*–*d* excitations are formally spin and parity forbidden. They are activated in $BiFeO_3$ and other transition metal oxides by spin-orbit coupling, exchange interaction, and odd parity phonons that hybridize states and break inversion symmetry [153]. The sharp structures superimposed on the *d*-*d* bands provide evidence of Nd^{3+} incorporation. The intensity increases with chemical substitution, and the line pattern depends upon the crystal field around the rare earth center. We assign these features as $4f$ excitations from the ${}^4I_{9/2}$ ground state to various excited states as indicated in Fig. 4.8(a) [152]. Naturally, the rare earth excitations in $Bi_{1-x}Nd_xFeO_3$ are very sensitive to the local structure [154]. Figures 4.8(b) and (c) display close-up views of the well-known ${}^4I_{9/2}$ → metastable ${}^4F_{3/2}$ and ${}^4I_{9/2} \rightarrow {}^2G_{7/2}+{}^4G_{5/2}$ exitations [152]. Compared with the features in the $x\leq0.10$ sample, the two peaks assigned as ${}^4I_{9/2}(0) \rightarrow {}^4F_{3/2}(0)$ and ${}^4I_{9/2}(0) \rightarrow {}^4F_{3/2}(1)$ [Fig. 4.8(b)] [155] start to disappear at x=0.15 and two new features with higher energy emerge at x=0.20; the separation also decreases by ∼14 cm^{-1}. Moreover, the peaks centered at 16,988 and 17,270 cm^{-1} split into doublets at x=0.20 [Fig. 4.8(c)]. These effects are due to distortion of the Nd^{3+} crystal field, a consequence of the structural change from rhombohedral in pristine $BiFeO_3$ → rhombohedral with slight triclinic distortion ($0.05\leq x\leq0.10$) → pseudo-tetragonal ($x\geq0.20$) [156].

Antiferromagnets have traditionally offered foundational opportunities to investi-

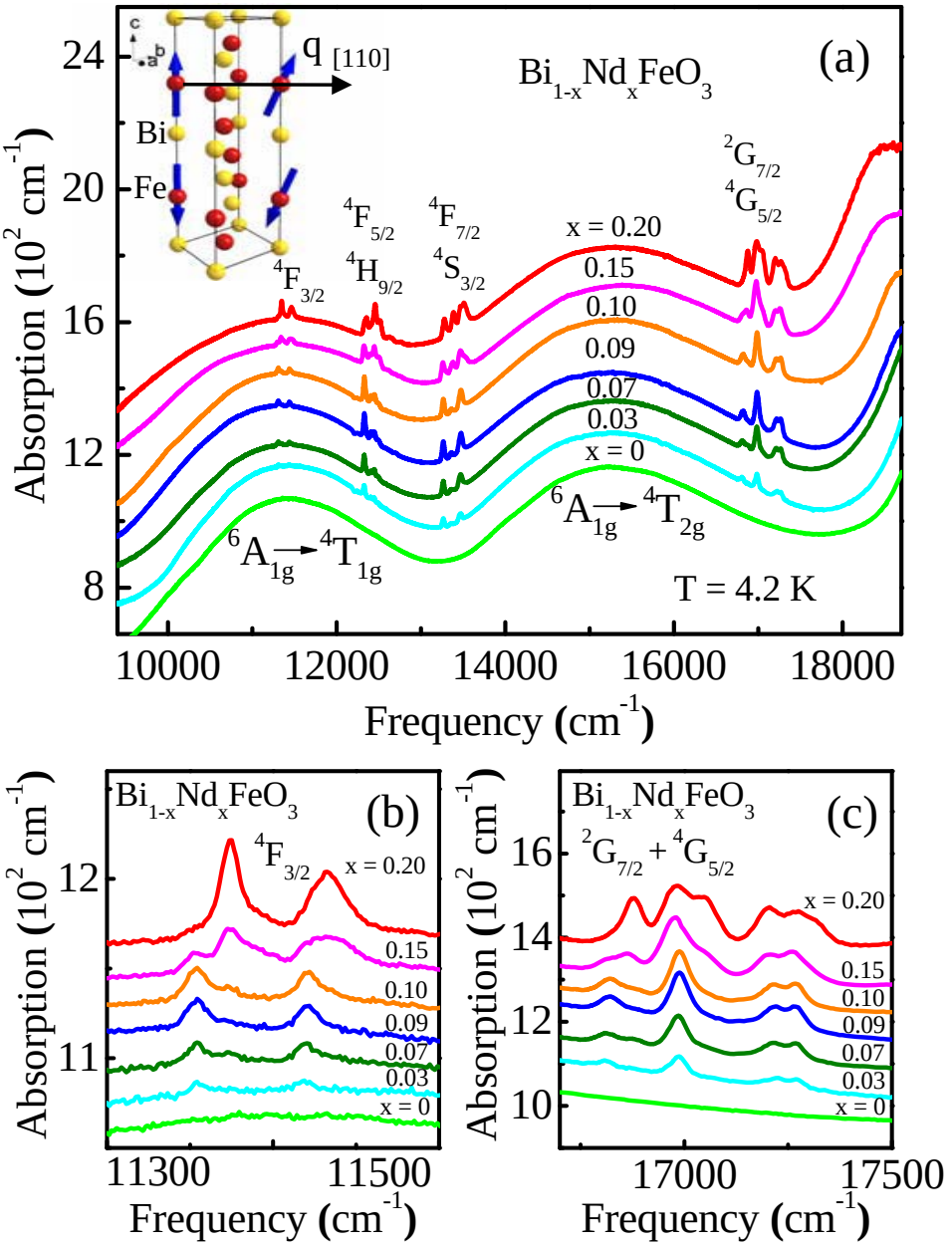

Figure 4.8: (Color online) (a) Absorption coefficient of $Bi_{1-x}Nd_xFeO_3$ ($0 \leq x \leq 0.20$) in the range of the on-site Fe^{3+} d-d excitations at 4.2 K. The spectra of the substituted compounds are offset along the y-axis for clarity. The sharp structures riding on top of the color band excitations are the well-known Nd^{3+} $4f$ excitations from the $^4I_{9/2}$ ground state to various excited states. They are labeled according to Refs. [8, 152]. Inset: structure of $BiFeO_3$ hexagonal unit cell. Only the Bi and Fe atoms are displayed for clarity. Spin spiral propagation (q) is along the $[110]_{hex}$ direction. (b, c) Close-up view of these excitations at different Nd^{3+} concentrations. Panel (b) shows the $^4I_{9/2} \rightarrow {}^4F_{3/2}$ features whereas panel (c) displays the $^4I_{9/2} \rightarrow {}^2G_{7/2}+{}^4G_{5/2}$ excitations. (after Ref. [111])

gate the collective excitations that arise from charge-spin coupling [157]. The magnon sideband is one of these well-known excitations. It arises from the combination of an exciton and a magnon and is commonly observed on the leading edge of the first d–d band in antiferromagnets like MnF_2 and α-Fe_2O_3 [14, 58]. Interestingly, the magnon sideband is not clearly evident in the linear absorption spectrum of single crystalline $BiFeO_3$ [8, 158]. This is because the center of symmetry between Fe^{3+} centers suppresses the transition of exchange coupled pairs [159]. Similarly, the magnon sideband is not directly observed in polycrystalline $Bi_{1-x}Nd_xFeO_3$ [Fig. 4.8(a)], though it is likewise expected. Our previous magneto-optical work on single crystalline $BiFeO_3$ finessed this situation, revealing underlying magnon sideband features in the magneto-optical response [8]. It is clearly very attractive to extend this technique to systems like $Bi_{1-x}Nd_xFeO_3$ where chemical substitution stabilizes weak ferromagnetism at the expense of the antiferromagnetic (spin spiral) phase. But here, the magnon sideband is both hidden and potentially contaminated with Nd^{3+} excitations [160]. Based on our previous work with pristine $BiFeO_3$ [8], a portion of the field-induced magnon sideband-related changes appear between 9500 and 11000 cm^{-1}, a regime where Nd^{3+} excitations are absent. Magnetochromism in this range therefore provides an an excellent opportunity to investigate how local magnetism (introduced by rare earth substitution) impacts the antiferromagnetic spin spiral state.

4.3.2 Magneto-optical properties to determine the critical field

Figure 4.9 summarizes the magneto-optical response of $Bi_{1-x}Nd_xFeO_3$. Panels (a), (c), and (e) display the field-induced absorption difference spectra for x=0.0, 0.09 and 0.20, substitutions that correspond to rhombohedral, triclinic, and pseudo-tetragonal crystal structures, respectively. Different magneto-optical contrast is observed depending on the Nd^{3+} concentration, an indication of magnon sideband sensitivity to competing

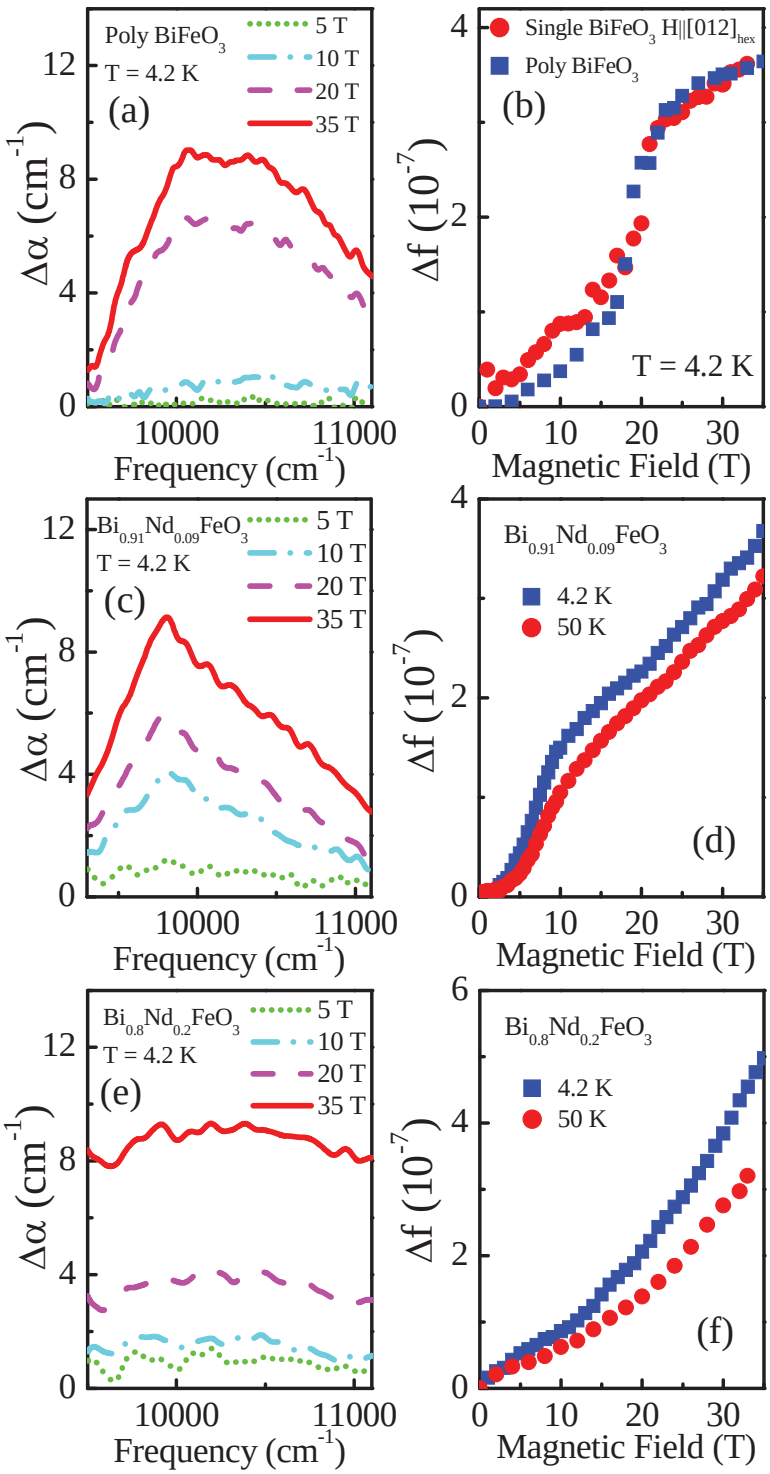

Figure 4.9: (Color online) Absorption difference spectra $\triangle\alpha$=$[\alpha(B) - \alpha(B = 0\ \mathrm{T})]$ of $Bi_{1-x}Nd_xFeO_3$ at 4.2 K for selected Nd^{3+} concentrations: (a) x=0, (c) x=0.09, and (e) x=0.20. (b) Comparison of oscillator strength change ($\triangle f$) in polycrystalline and single crystalline $BiFeO_3$ [8] in the magnon sideband range as a function of applied magnetic field. (d, f) Comparison of oscillator strength change ($\triangle f$) at selected temperatures (4.2 and 50 K) for (d) x=0.09 and (f) x=0.20. (after Ref. [111])

local and long-range magnetic interactions [161]. The magnon sideband intensity also increases with magnetic field. We quantified these effects with the oscillator strength sum rule [102]: $\Delta f \equiv \frac{2c}{N_e \pi \omega_p^2} \int_{\omega_1}^{\omega_2} n \Delta\alpha(\omega, B)\, \mathrm{d}\omega$. Here, f is the oscillator strength, N_e=5 is the number of electrons per Fe^{3+} site, $n \simeq 2.7$ is the refractive index [69], ω_p is the plasma frequency$\equiv \sqrt{\frac{e^2 \rho}{m \epsilon_0}}$, e and m are the charge and mass of an electron, ϵ_0 is the vacuum dielectric constant, ρ is the density of Fe sites [156], c is the speed of light, and ω_1=9500 cm^{-1} and ω_2=11000 cm^{-1} are the frequency limits of integration. Δf of polycrystalline $BiFeO_3$ displays a broad increase in the 17-26 T range [Fig. 4.9(b)], different from the sharp jump at 20 T [8, 64] in $(012)_{hex}$ face single crystals. The latter can be unambiguously assigned as the field-induced spin spiral quenching transition that drives toward a homogeneous canted antiferromagnetic state above the critical field (B_C) [64]. Orientational averaging of the easy and hard magnetization axes accounts for the broad transition region in polycrystalline $BiFeO_3$ [64,162,163]. As shown in Figs. 4.9(d) and 4.9(f), increasing temperature also reduces Δf, a trend that is probably related to the approach of the 140 K spin-reorientation transition [164,165]. The temperature-induced reduction of Δf is larger at higher rare earth substitution levels, a result that we attribute to Nd^{3+}-Fe^{3+} interactions. In principle, f follows phonon assisted trends [8], so Δf is expected to increase at high temperature (T>250 K). At x=0.20, we find only a smooth increase in Δf with no optical signature of the field-induced transition. This indicates that spiral order is suppressed in $Bi_{0.80}Nd_{0.20}FeO_3$. Antiferromagnetic sublattice canting [78,79] instead results in weak ferromagnetism [156].

4.3.3 B–T–x Phase diagram

We combined these magneto-optical results to generate the B–T–x diagram of $Bi_{1-x}Nd_xFeO_3$ [Fig. 4.10(a)]. At low magnetic fields and modest Nd^{3+} incorporation levels, $BiFeO_3$ and the chemically-substituted analogs possess spiral magnetic order as indicated by

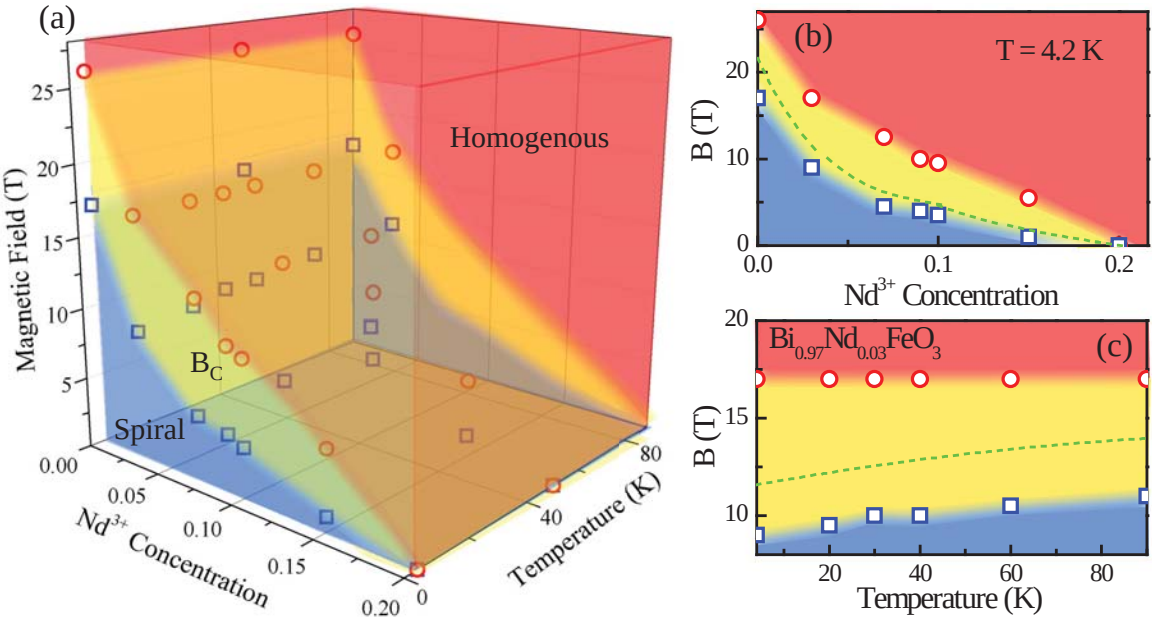

Figure 4.10: (Color online) (a) B–T–x phase diagram of $Bi_{1-x}Nd_xFeO_3$ constructed using change in oscillator strength ($\triangle f$) data in the range of the magnon sideband. Panels (b) and (c) show Nd^{3+} concentration and temperature slices taken from this three-dimensional plot. The B–x diagram is at 4.2 K, and the B–T plot is for x=0.03. The blue squares indicate the phase boundary between spiral magnetic ordering and transition region, the red circles represent the phase boundary between transition region and homogeneous magnetic ordering. Error bars of these boundaries are smaller than the symbol size and not shown. The mean value of the transition region is indicated by the green dashed lines. (after Ref. [111])

the blue shading. At the other extreme, high magnetic field [8, 67] and additional rare earth substitution quench the spin spiral and strongly stabilize the homogeneous magnetic state. The latter is indicated in red. The transition region (shown in yellow) is broadened due to orientational averaging effects. As discussed below, two-dimensional cross sections of this B–T–x diagram (at fixed temperature and composition) reveal the important trends more clearly.

Figure 4.10(b) summarizes the B–x behavior of $Bi_{1-x}Nd_xFeO_3$ at 4.2 K. With substitution, the critical field demarcated by the yellow transition region decreases systematically. The Ginzburg-Landau free energy and harmonic cycloid approximation [18, 64, 166] provide a framework within which we can understand this trend. For a randomly oriented material, an applied field with arbitrary orientation results in a broad critical field region. We set $[001]_{hex}$ as the z axis, and the spin spiral propagation direction $[110]_{hex}$ as the y axis. Our calculation follows the work of Le Bras *et al.* [18]. When the magneto-electric induced effective field (B_{ME}=$m_s/\chi_\perp$) is small compared with the critical field along the z axis ($B_{C,z} = \sqrt{\frac{4(Aq^2-\frac{|K|}{2})}{\chi_\perp}}$), a minimum critical field can be obtained when field is along the y axis:

$$B_{C,min} = \frac{2m_s}{\chi_\perp}(-1 + \sqrt{\frac{3}{4} + \frac{\chi_\perp(Aq^2 - \frac{|K|}{2})}{m_s^2}}). \tag{4.7}$$

Here, A is the exchange stiffness constant, K is the uniaxial anisotropy constant in zero field, m_s is the magneto-electric induced magnetization, $\chi_\perp$ is the magnetic susceptibility in the direction perpendicular to the antiferromagnetic vector, and q is the wave vector. When field is along the x axis, B_C reaches a maximum:

$$B_{C,max} = \frac{Aq^2 - \frac{|K|}{2}}{m_s} - \frac{m_s}{4\chi_\perp}. \tag{4.8}$$

$B_{C,min}$ and $B_{C,max}$ correspond to the lowest and highest boundaries of the yellow tran-

sition region in Fig. 4.10(b), respectively. In $BiFeO_3$, $K \ll Aq^2$ [64] and can be neglected. Using the reported values of $\chi_\perp$=4.7×10^{-5} [64, 166], q=$\frac{2\pi}{\lambda}$(λ=620 $\mathring{A}$) [162], m_s = 2.56 emu/cm^3 [64] and A=8.0 ×10^{-7} erg/cm [166], we find $B_{C,min}$=17 T and $B_{C,max}$=30 T for pristine $BiFeO_3$. These predicted values are in excellent agreement with our magneto-optical results. Chemical substitution has important effect on the anisotropy constant. Experimentally, we find that $B_{C,min}$=3.5 T and $B_{C,max}$=9.5 T for $Bi_{0.90}Nd_{0.10}FeO_3$. Using $\chi_\perp$=7.2×10^{-5} [156] and λ=680 $\mathring{A}$ (under the assumption that spiral wavelength typically increases by ∼10% with low levels of substitution [167]), we estimate that m_s is ∼0.5 emu/cm^3. Assuming exchange stiffness remains the same, we find $|K| = 1.3 \times 10^6$ erg/cm^3. These results agree reasonably with the estimates from electron spin resonance and magnetization [18, 166]. The value of K is comparable to Aq^2, therefore, we conclude that anisotropy constant increases with Nd^{3+} ions substitution. As a further self-consistency check, we calculated B_{ME} and $B_{C,z}$ for $x \leq 0.10$ using Eqns. 4.7, 4.8 and found B_{ME} is less than 4% of $B_{C,z}$, confirming the validity of our approach. Moreover, we can obtain the mean value of critical field by using our estimated m_s and K and averaging over all applied field orientations. This quantity is plotted as a function of x and T as a green dashed line in Figs. 4.10(b) and (c). These curves fall well within the transition region mapped out by our spectroscopic work, demonstrating the effectiveness of these expressions in explaining critical field phase boundary behavior [168]. Finally, we point out that the exponential decay of $B_{C,ave}$ is much faster than the linear decay revealed by La^{3+} substitution [18], an effect that emanates from magnetic interactions between between Fe^{3+} and Nd^{3+} centers.

Figure 4.10(c) displays the B–T behavior of $Bi_{0.97}Nd_{0.03}FeO_3$. This fixed composition slice of the three-dimensional phase diagram at $x = 0.03$ is useful for understanding how temperature impacts magnetic anisotropy and the critical field. With increasing temperature, the spiral → crossover regime boundary increases whereas that between

the crossover regime and homogeneous magnetic phase is relatively constant. These trends combine to stabilize the spin spiral phase at the expense of the crossover regime, in excellent agreement with the field induced polarization result [67]. Reduced magnetic susceptibility over this temperature range along with an increasingly important $\chi_{\parallel}$ (typical of antiferromagnets) is probably behind this progression [7, 169]. At much higher temperatures (but still below T_N), the increased susceptibility will lead to a lower critical field [169]. Moreover, $\chi_{\parallel}$ will approach $\chi_{\perp}$, which drives $B_{C,min}$ towards $B_{C,max}$. Temperature is thus expected to reduce the width of the transition regime, ultimately condensing it to a slice.

Chapter 5

Magnetic field–induced color change in α-Fe_2O_3

We investigated the magneto-optical properties of α-Fe_2O_3 in order to understand the interplay between charge and magnetism in a model transition metal oxide. We discovered that hematite appears more red in applied magnetic field than in zero field conditions, an effect that is amplified by the presence of the spin flop transition. Analysis of the exciton pattern on the edge of the *d*-*d* color band reveals $C2$ monoclinic symmetry in the high field phase. Below, we discuss the color band, magnon sideband, and exciton behavior at low temperature and high magnetic field.

5.1 Optical response of hematite

Figure 5.1(a) displays the optical response of α-Fe_2O_3. We assign the two strong, broad bands centered at ∼11550 and 15300 cm^{-1} as ${}^6A_{1g} \rightarrow {}^4T_{1g}$ and ${}^6A_{1g} \rightarrow {}^4T_{2g}$ on-site excitations [54, 173]. These *d*–*d* excitations are formally forbidden although they appear in many oxides due to spin-orbit coupling, exchange interaction, and odd parity phonons that hybridize states and break inversion symmetry [54, 153, 157]. Low

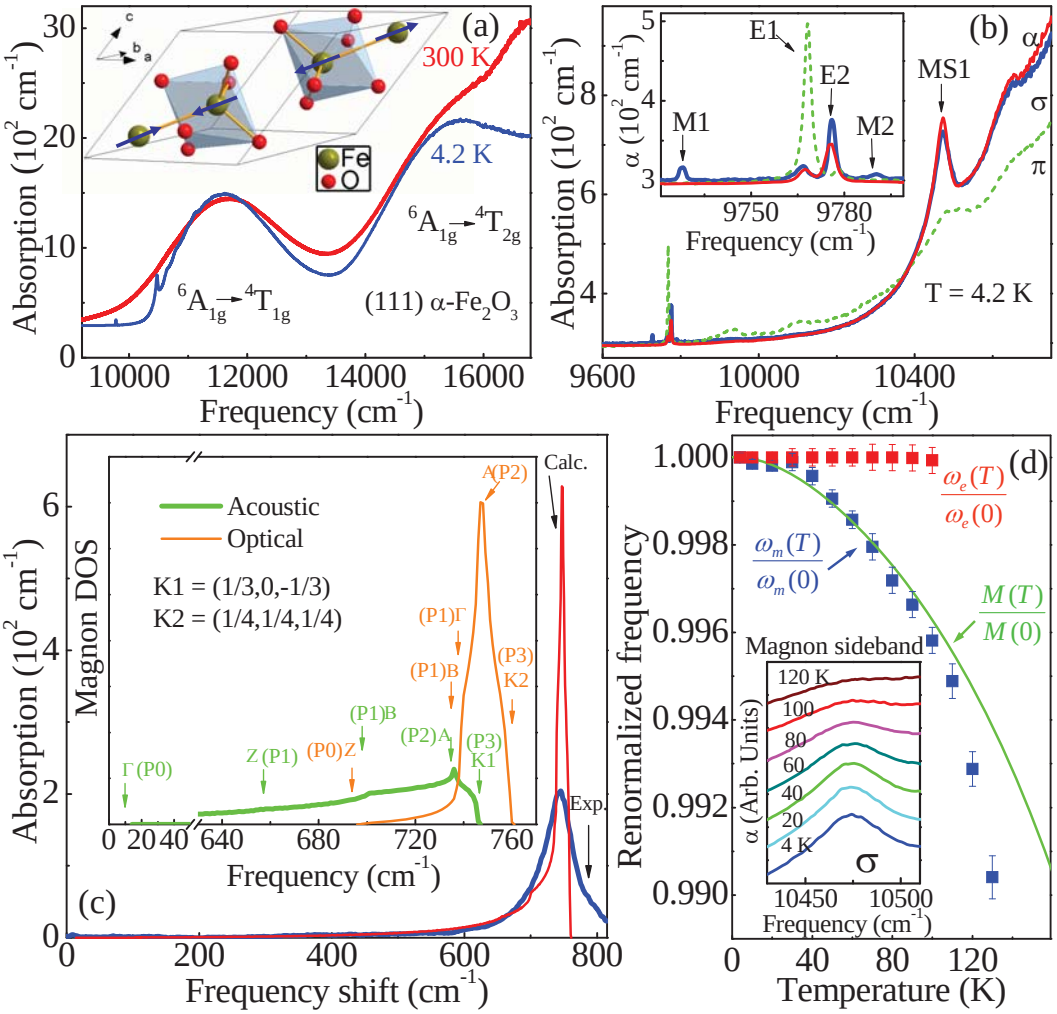

Figure 5.1: (a) (Color online) Absorption coefficient, $\alpha(\omega)$, of α-Fe_2O_3 in the range of on-site Fe^{3+} d-d excitations at 300 and 4.2 K. Inset: rhombohedral lattice [80] and low temperature four sublattice spin structure [77]. (b) Close up view of the fine structure on the leading edge of the $^6A_{1g} \rightarrow {}^4T_{1g}$ on-site excitation at 4.2 K in the α, σ and π polarizations. Inset: close-up view of the excitons. (c) Comparison of the σ-polarized magnon sideband absorption spectrum with the calculated density of states. Inset: Calculated magnon density of states using optimized exchange constants J_1 = 7.6 K, J_2 = 2.0 K, J_3 = -27.7 K, and J_4 = -22.2 K. The frequency channel width was taken to be the same as the spectral resolution (1 cm^{-1}). The nature of the critical points in Brillouin zone are indicated [170]. (d) Temperature dependence of E1 (π) exciton and magnon sideband (MS1, α) peak positions, expressed as the ratio of $\frac{\omega_e(T)}{\omega_e(0)}$ and $\frac{\omega_m(T)}{\omega_m(0)}$, respectively. The latter compares well with the calculated sublattice magnetization [28,171] using the same exchange constants listed above. Inset: $\alpha(\omega)$ of the σ-polarized magnon sideband at different temperatures. (after Ref. [14])

Table 5.1: Properties of ${}^6A_{1g} \rightarrow {}^4T_{1g}$ fine structure in α-Fe_2O_3 at 4.2 K. In the line notation, M represents magnetic dipole character, E is electric dipole and MS is magnon sideband. In the polarization notation, α ($\widetilde{E} \perp c, \widetilde{B} \perp c$), σ ($\widetilde{E} \perp c, \widetilde{B} \parallel c$), π ($\widetilde{E} \parallel c, \widetilde{B} \perp c$), $\widetilde{E}$ and $\widetilde{B}$ are the electric and magnetic vector of light, c is [111] axis of the crystal. $f \equiv \frac{2c}{N_e \pi \omega_p^2} \int_{\omega_1}^{\omega_2} n\alpha(\omega, B)\, \mathrm{d}\omega$, here, $N_e = 5$ is the number of electrons per Fe site, $n \simeq 2.23$ is the refractive index, ω_p is the plasma frequency $\equiv \sqrt{\frac{e^2\rho}{m\epsilon_0}}$, e and m are the charge and mass of an electron, ϵ_0 is the vacuum dielectric constant, ρ is the density of Fe sites, c is the speed of light, ω_1 and ω_2 are the frequency limits of integration [102].

Line	Polarization	Position	f	Representation	
		(cm^{-1})	10^{-10}	C_3	R$\bar{3}$C
M1	σ	9727.9	4.8	A	Γ_2^+
E1	π	9766.4	80	A	Γ_2^- [172]
	α, σ		8.6	C_1/C_2	Γ_3^-
E2	π	9776.1	4.3	A	Γ_2^- [172]
	α, σ		23	C_1/C_2	Γ_3^-
M2	σ	9790.1	2.5	A	Γ_2^+
MS1	α, σ, π	10471.5	1400		

temperature reveals a great deal of fine structure on the leading edge of the ${}^6A_{1g} \rightarrow {}^4T_{1g}$ band (Fig 5.1(b)). These strongly polarized features are collective excitations. Their properties are summarized in Table 5.1. For the purposes of our discussion, the fundamental magnetic- and electronic-dipole excitations, M1 and E1, are most important. Interactions between four translationally inequivalent Fe^{3+} sites in the magnetic structure give rise to Davydov splitting between the (M1σ, E1π) and (M2σ, E2π) exciton pairs. These splittings are 38.6 and 14.0 cm^{-1}, respectively, an order of magnitude larger than in $YCrO_3$ (2 cm^{-1}) [174] and Cr_2O_3 (3.5 cm^{-1}) [175]. This is a consequence of the larger inter-sublattice coupling energy in α-Fe_2O_3. The feature labeled MS1 is assigned as the magnon sideband [173]. Based on the position, shape, and polarization behavior, we associate it with the M1σ exciton [176]. The intensity is stronger than that of M1σ because this electric dipole-allowed excitation involves pairs of ions and thus breaks the parity selection rule [157, 177]. The magnon sideband frequency can be expressed as $\omega = \omega_e + \omega_m$ [58], where ω_e is the exciton frequency, and ω_m is the magnon frequency. We find $\omega_m = 743.7 \pm 0.1$ cm^{-1} in excellent agreement with the magnon energy obtained by neutron scattering [28]. Other collective excitations including phonon sidebands and the two magnon sideband are also observed.

We analyzed the magnon sideband selection rules [178] at different points in the Brillioun zone and calculated the density of states using the magnon dispersion of Samuelsen [112]. The results are in good agreement with the measured absorption spectrum (Fig. 5.1(c)) and explain the directionally-dependent magnon sideband shape. The exciton and magnon features display characteristic temperature dependence. As shown in Fig. 5.1(d), expressing the magnon sideband frequency as $\frac{\omega_m(T)}{\omega_m(0)}$ reveals high temperature softening, whereas the reduced frequency of the E1π exciton is relatively constant. The former compares well with a numerical calculation of the normalized sublattice magnetization ($\frac{M(T)}{M(0)}$) using the random phase approximation. The discrep-

ancy in the high temperature range is because magnetization measures the thermal average population of magnons and is less sensitive to the zone boundary (A point) dispersion [7, 58]. Similar effects are observed in MnF_2 [58] and Cr_2O_3 [179].

5.2 Magnetochromic effect in α-Fe_2O_3

Figure 5.2a displays the field-induced absorption difference spectra of α-Fe_2O_3 for different crystal orientations and magnetic field directions. The magnetochromic response reveals that the on-site excitations are intrinsically coupled to the microscopic spin structure. We can quantify the field-induced color change with the partial sum rule (inset, Fig 5.2a) [102]. Oscillator strength changes (Δf) show a first order transition at $B_{C\parallel} = 6.6 \pm 0.2$ T when B $\parallel$ [111], and a broad transition at $B_{C\perp} = 16.2 \pm 0.2$ T when B $\perp$ [111]. These critical fields are easily assigned as field-induced spin flop transitions in agreement with magnetization [29] and ultrasonic attenuation measurements [30]. Importantly, the *d–d* on site excitations are in the visible range and responsible for the reddish color of α-Fe_2O_3. As shown in the absorption difference plot, this system absorbs fewer photons in the red color range in high magnetic field (on the order of 2% less). α-Fe_2O_3 thus appears more red in the magnetically reoriented phase [180]. This color change is observed because the coherent spin transition amplifies the charge-spin interaction beyond what one might expect from traditional spin-orbit processes alone. The field-induced reduction of oscillator strength of the ${}^6A_{1g} \rightarrow {}^4T_{1g}$ band is partially recovered in the magnon sideband (insets, Fig. 5.2a). Optical property changes driven by magnetic order reorientation have been observed in other functional materials including $FeCO_3$ (color contrast at the 13 T spin-flop transition) [12] and $BiFeO_3$ (color change at 20 T due to spin spiral quenching) [8]. Here, we report the discovery of such an effect in α-Fe_2O_3, although it occurs by a fundamentally different mechanism.

Magnon sideband formation is controlled by exchange coupled pairs [159, 177], and

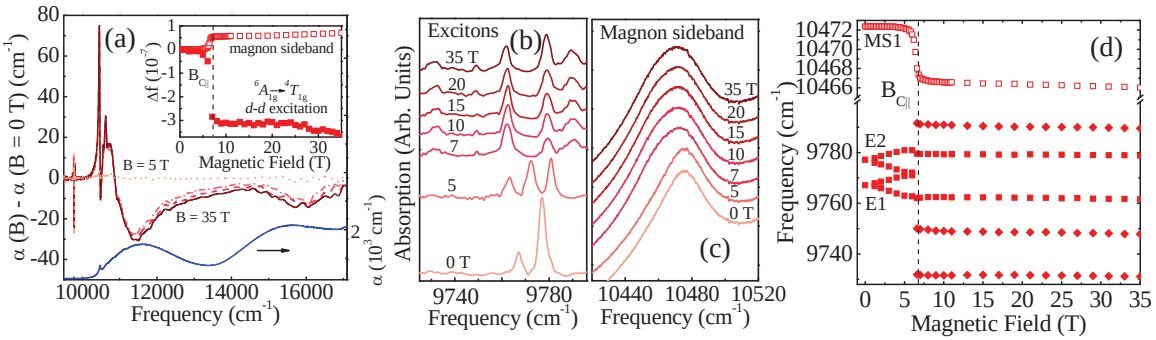

Figure 5.2: (Color online) (a) Absorption difference spectra [α(B) - α(B = 0 T)] of α-Fe_2O_3 at 4.2 K for the α-polarization and B $\parallel$ [111] at selected magnetic fields: 5, 10, 15, 35 T. The corresponding low temperature zero field absorption spectrum is shown as a blue solid curve for comparison. Inset: oscillator strength change in the range of the magnon sideband and ${}^6A_{1g} \rightarrow {}^4T_{1g}$ on-site excitation as a function of magnetic field. (b, c) Close-up view of the excitons and magnon sideband at selected fields. (d) Peak position vs. magnetic field for the exciton and magnon sideband features. Error bars of these positions are smaller than the symbol size and not shown.

as a consequence, field-induced magnetic order reorientation will significantly impact the behavior. Strikingly, the magnon sideband displays a 27% increase in oscillator strength at 35 T compared to its zero field value (insets, Fig. 5.2a). Magnon sideband intensity is dependent upon (i) exciton + magnon joint density of states and (ii) collinearity of the magnetic structure [13]. It will decrease dramatically if spin collinearity is violated as in $RbMnF_3$ [13] and $FeCO_3$ [12]. Based on the observed intensity increase, we conclude that spin collinearity is conserved through the spin-flop in α-Fe_2O_3. Figure 5.2b shows a close-up view of the magnon sideband excitation at selected magnetic fields. The field-induced frequency shifts are summarized in Fig. 5.2c, and like the oscillator strength, place the critical fields for spin-flop at $B_{C\parallel}$ = 6.6 $\pm$ 0.2 T and $B_{C\perp}$ = 16.2 $\pm$ 0.2 T. Importantly, the magnon sideband softens by $\sim$6 cm^{-1} through the 6.6 T transition. Assuming that the magnon dispersion does not change substantially [112], we can estimate changes in the exchange constants ($\frac{\Delta J}{J}$) using the least square method and a fit of the magnon density of states to the 35 T σ-polarized spectrum. The results show that ferromagnetic couplings J1 and J2 in-

crease by ∼15% and 8% respectively, whereas antiferromagnetic couplings |J3| and |J4| decrease by about 1%. These results indicate larger direct exchange [28] and smaller superexchange in the high field phase.

5.3 High field magnetic structure of α-Fe_2O_3

Exciton behavior provides an incisive probe of Zeeman-splitting in α-Fe_2O_3. As shown in Fig. 5.2c, the E1α and E2α excitons split into two components, each with total g values of 3.77 ± 0.1. This splitting is due to the removal of up- and down-spin sublattice degeneracies in the field [181]. The two sublattice model [11] allows us to evaluate g' of the excited state. We find $g' = 2.08 \pm 0.03$ assuming a ground state single sublattice g of 2 for E1 and E2. Using this g', we can back calculate [11] a magnon sideband g of 0.22, a value that is consistent with the lack of observed splitting in this feature up to $B_{C\|}$. These g values are typical for antiferromagnets [11], demonstrating that spin-orbit coupling in the excited $^4T_{1g}$ states is similar to that in MnF_2, even though the exchange interaction is much larger.

When the field is applied in the (111) plane, the excitons display Zeeman-like splitting above 13 T (Fig. 5.3(k,l)). The peculiar appearance is due to removal of degeneracy of the spin component parallel to the field. The exciton pattern in the new magnetically ordered state is consistent with the aforementioned group theory predictions for $C2$ magnetic symmetry, demonstrating that magnetic fields in different directions drive to identical high field phases in α-Fe_2O_3. Finally, above $B_{C\perp}$, Davydov splitting of (M1σ, E1π) and (M2σ, E2π) decreases by ∼8 and 2 cm^{-1}, respectively. This indicates that the inter-sublattice coupling energy is reduced compared to that in zero field.

Exciton behavior can also be used to reveal magnetic symmetry in the high field phase of α-Fe_2O_3. At $B_{C\|}$, the Zeeman splitting disappears, and a new pattern emerges

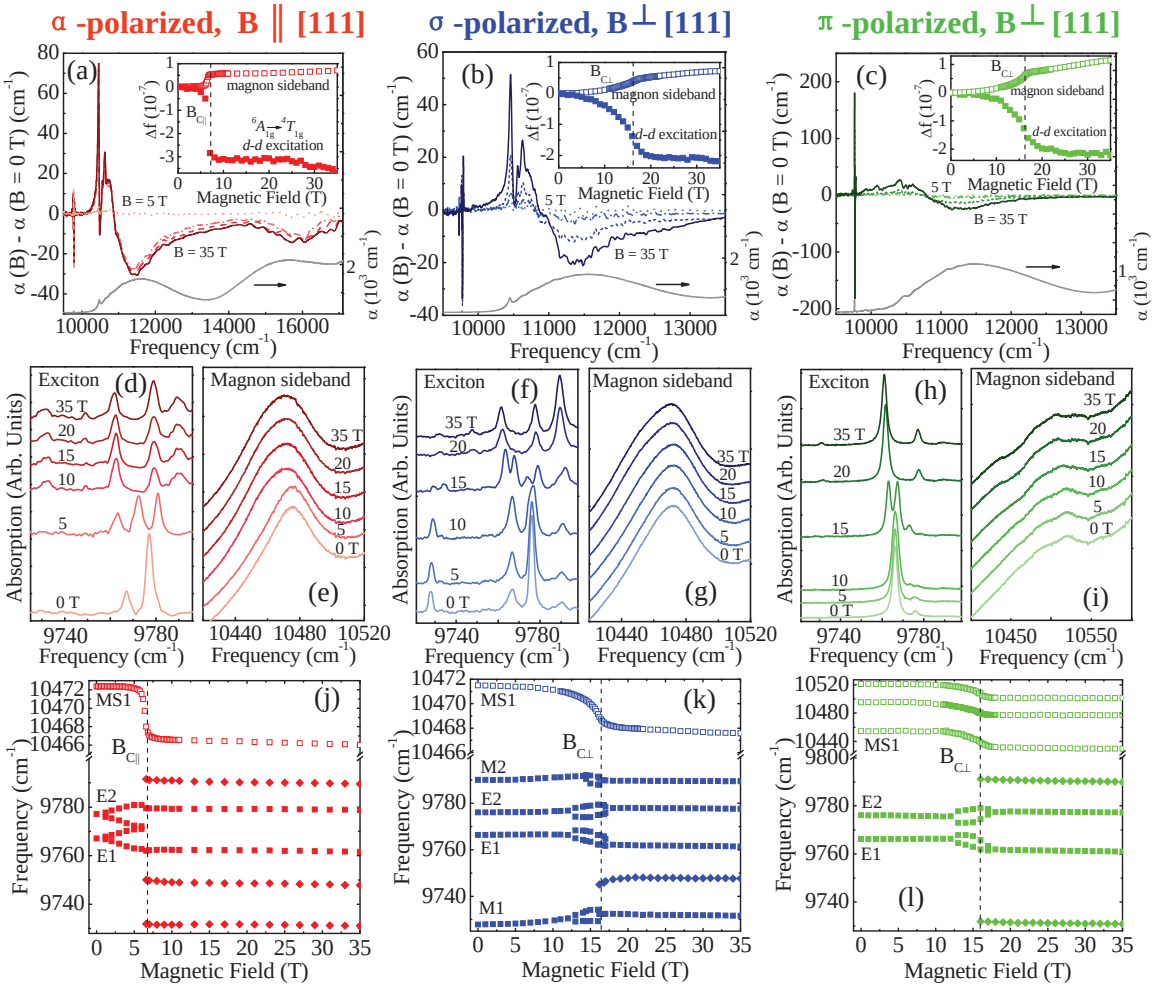

Figure 5.3: (Color online) Absorption difference spectra $[\alpha(B) - \alpha(B = 0\ \mathrm{T})]$ of α-Fe_2O_3 at 4.2 K for different crystal orientations and magnetic field directions: (a), α-polarization and B ∥ [111], (b), σ-polarization and B ⊥ [111], and (c), π-polarization and B ⊥ [111] at selected magnetic field 5, 10, 15, 35 T. The corresponding low temperature zero field absorption spectra are shown as gray solid curves for comparison. Insets: oscillator strength change in the range of the magnon sideband and ${}^6A_{1g} \rightarrow {}^4T_{1g}$ on-site excitation as a function of magnetic field. Close-up view of the excitons (d,e,f) and magnon sidebands (g,h,i) in the α-, σ-, and π-polarizations at selected magnetic fields. (j,k,l) Peak position vs. magnetic field for the exciton and magnon sideband features for the polarizations and field directions of interest. (after Ref. [14])

(Fig. 5.3(j)). This more complicated exciton pattern arises from the transition to a different magnetic ordering. Above $B_{C\|}$, lower symmetry lifts the degeneracy of the E1α excition and gives rise to a new peak at $\sim$9748 cm^{-1} [182]. Two magnetic-dipole excitons, M1σ and M2σ, are also activated due to the new coordinate system (and selection rules) above 6.2 T. M1σ hardens by 4.6 cm^{-1}, whereas M2σ softens by 0.5 cm^{-1}. To explore the symmetry of the high field phase, we make use of the observed exciton pattern in the α-, σ-, and π-polarizations and invoke two additional constraints: (i) the new magnetic order symmetry must be a subgroup of the original $R\bar{3}c$ structure and (ii) spin collinearity is conserved above $B_{C\|}$. The latter is based upon the increase in magnon side band intensity with field and requires that inversion and $C2$ rotational operations be maintained. Several symmetry candidates emerge from this analysis [183]. They include $P1$, $P\bar{1}$, $C2$, Cc, $C2/c$, $R3$, $R\bar{3}$, $R32$, and $R3c$. Only the $C2/c$ monoclinic structure contains the necessary inversion center and $C2$ rotational axis. We thus infer that the field-induced magnetic ordering is monoclinic with $C2/c$ symmetry - at least to first order. We know, however, that weak canting due to the Dzyaloshinskii–Moriya effect formally eliminates the inversion center [78, 79] (Fig. 5.4(b)). This higher order effect places additional constrains on the system. Reevaluating the magnetic symmetry with the surviving $C2$ operation (and without the inversion center), we find that only the $C2$ monoclinic structure meets our criteria. We therefore conclude that the formal symmetry of the field-induced ordered phase of α-Fe_2O_3 is $C2$. Switching the applied field to the (111) plane, the exciton pattern in the new magnetic order is consistent with the aforementioned group theory predictions for $C2/c$ or $C2$ magnetic symmetry (depending upon whether spin canting-induced symmetry breaking is ignored or invoked), demonstrating that magnetic fields in different directions drive to identical high field phases in α-Fe_2O_3.

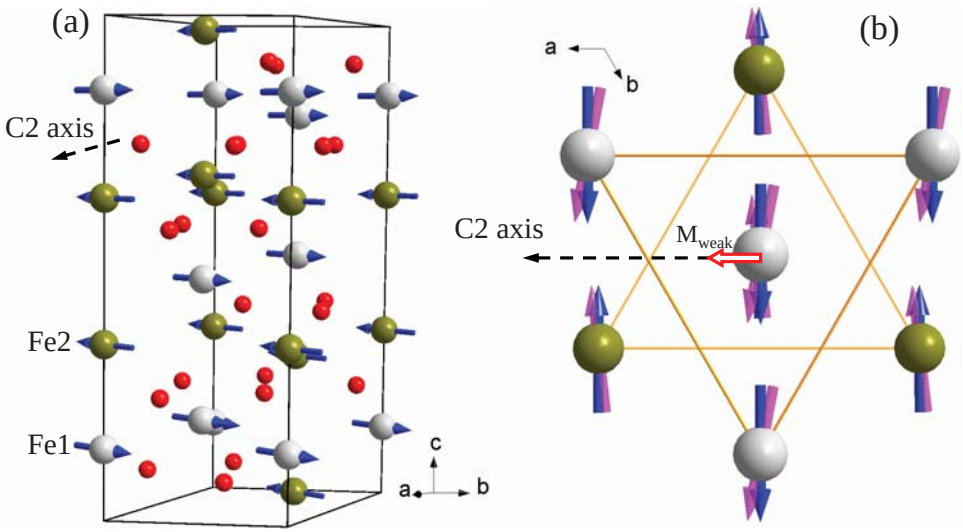

Figure 5.4: (a) Schematic view of the high temperature [77]/field magnetic structure of α-Fe_2O_3. The $C2$ rotational axis is indicated. (b) View of the magnetic ordering pattern looking down the [111] axis showing only the Fe centers. Blue arrows denote the collinear spin arrangement, and purple arrows schematically show the non-collinear state. The canting angle is on the order of $\sim 10^{-4}$ degrees and arises due to Dzyaloshinskii–Moriya interactions [78, 79]. Canting induces a weak ferromagnetic moment along the direction of the $C2$ rotational axis (red arrow). This symmetry is clarified on the central Fe site, where the spin vector on the site of interest is shown along with that on the site below. (after Ref. [14])

Chapter 6

Magnetic field-induced shift of the optical band gap in $Ni_3V_2O_8$

Spin-charge interactions underpin much of the rich science of multifunctional oxides and provide a mechanism for cross-coupling in external field. Here, we investigate control of charge by magnetic field in multiferroic $Ni_3V_2O_8$ with special emphasis on the color properties. Our measurements reveal field-induced blue shifts of the band gap (50 meV over 37 T for $B \parallel b$) that are much larger than those driven by temperature. $Ni_3V_2O_8$ therefore appears more green in the fully polarized state, a finding that we verify with direct photographic images. This chapter presents band gap behavior in various temperature and magnetic field and the evidence used to support these findings.

6.1 Magneto-optical properties of $Ni_3V_2O_8$

6.1.1 High field-induced band gap shift

Figure 6.1(a) displays the optical response of $Ni_3V_2O_8$. We assign the broad $\simeq$1.54 and 1.68 eV bands as ${}^3A_{2g} \rightarrow {}^1E_g$ and ${}^3A_{2g} \rightarrow {}^3T_{1g}$ d to d excitations on the Ni^{2+} centers. [92]

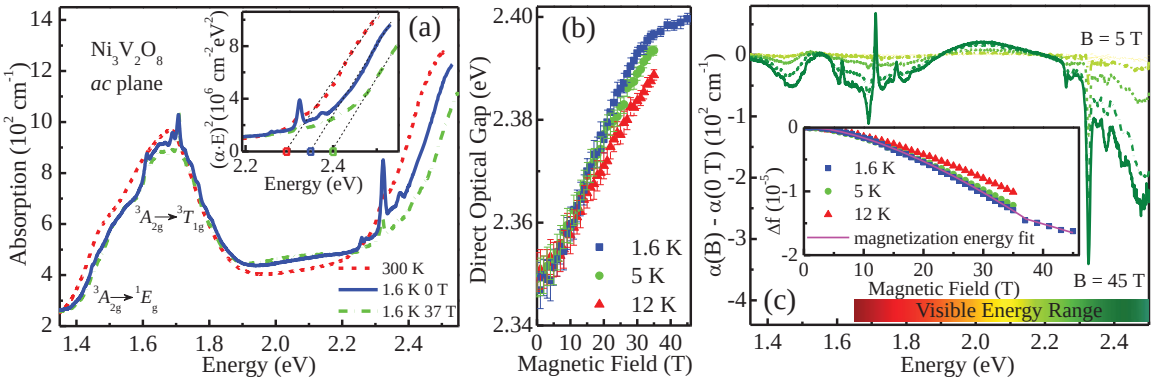

Figure 6.1: (a) (Color online) Absorption coefficient, α(E), of $Ni_3V_2O_8$ in the visible range at 1.6 K for selected fields and temperatures. Inset: Direct optical gap analysis. The (red) square marks the 2.29±0.01 eV optical gap of $Ni_3V_2O_8$ at 300 K, the (blue) square marks the 2.35±0.01 eV gap at 1.6 K, and the (green) square marks the 2.40±0.01 eV gap at 1.6 K with applied field of 37 T. (b) optical gap vs. magnetic field at selected temperatures 1.6, 5 and 12 K. (c) Absorption difference spectra [α(B) - α(B = 0 T)] of $Ni_3V_2O_8$ at 1.6 K for B $\parallel$ b axis at selected magnetic fields: 5, 10, 20, 35, 45 T. Inset: oscillator strength change (Δf = f(B) - f(B = 0 T) which is proportional to the integrated absorption coefficient) in the range of optical gap edge (2.17 - 2.50 eV) as a function of magnetic field at selected temperatures: 1.6, 5 and 12 K. The integrated magnetization [89] (magenta line) fits well with the Δf trend.

Another set of on-site excitations ($^3A_{2g} \rightarrow {}^3T_{2g}$) resides at lower energy. These d–d excitations are formally forbidden but become allowed due to spin-orbit coupling, exchange interaction, and odd parity phonons that hybridize states and break inversion symmetry. [14,157,184] In $Ni_3V_2O_8$, there may also be some mixing with unoccupied V states. [185] Resonant inelastic x-ray scattering and crystal field multiplet theory also reveal that the crystal field around the crosstie and spine sites is not very different. [185] Charge transfer excitations appear above 2.2 eV in the absorption spectrum and can be assigned as O *2p* to Ni and V *3d* hybridized excitations. [91] These excitations define the charge gap in $Ni_3V_2O_8$. We find that the gap is 2.35 eV at 1.6 K, [186] higher than previously supposed [91,187] but in good agreement with recent x-ray absorption and emission data [185], local density approximation (LDA)+U calculations for U=5 eV [91], and the shifted partial density of states in Ref. [185]. A linear fit of $(\alpha \cdot E)^2$ vs. E [inset, Fig. 6.1(a)] [102] shows that the 2.35 eV band gap is direct. A similarly large

optical gap is found in sputtered thin films. [188] Importantly, the ${}^3A_{2g} \rightarrow {}^3T_{1g}$ d to d excitation and the band gap are in the visible range and responsible for the yellowish-green appearance of $Ni_3V_2O_8$. Moreover, the charge gap red shifts by 60 meV between 1.6 and 300 K, similar to that in other oxides [189]. The fine structure riding on top of the on-site excitations and gap edge is assigned as a series of excitons. [157] They soften with increasing temperature.

Magnetic field drives $Ni_3V_2O_8$ from the commensurate antiferromagnetic state at 1.6 K and zero field, through a series of non-colinear regimes, and into the fully polarized paramagnetic state. [89] At the same time, the charge gap moves from 2.35 to 2.40 eV at 1.6 K and 37 T, a blue shift of 50 meV for $B \parallel b$. Between 37 and 45 T, changes in the gap edge are small and within 5 meV, indicating that the optical response saturates above the critical field. Strikingly, the field-induced modification of the gap edge below the critical field ($\approx$1.4 meV/T) is larger than the temperature-induced shift ($\approx$0.2 meV/K = 0.3 meV/T), and it exceeds what might be expected from the Zeeman effect (4.8 meV at 37 T; 0.13 meV/T) [89] by a considerable amount. This implies that field is a more effective tuning parameter than temperature. It also suggests that the excess (beyond that from normal Zeeman interactions) is due to an additional coupling mechanism, as discussed below. Considering the complexity of the B-T phase diagram, [34,89] one might anticipate anomalies in the charge gap at the magnetically-driven phase transitions. Our data instead reveal that the gap changes smoothly and continuously both below and above the 37 T critical field (Fig. 6.1(b)), with only a slope change as the system goes into the fully polarizaed state. The field-induced blue shift is slightly less at higher temperatures due to thermal broadening effects. Turning briefly to the other spectral features, the intensity of the d-d excitations decreases with field, a behavior also observed in hematite. [14] However, the magnitude of change in the site excitations in $Ni_3V_2O_8$ is $\approx$5 times greater, a consequence of larger spin-charge

coupling. We also find that the exciton peak positions follow the magnetization energy. In the following discussion, we focus on the gap behavior and its relation to the color property modifications.

Figure 6.1(c) displays the magnetic field-induced absorption difference spectra of $Ni_3V_2O_8$. In high field, this system absorbs fewer photons in the green color range (on the order of 24% less at 45 T). $Ni_3V_2O_8$ thus appears more green in the fully polarized paramagnetic state than at zero field. We quantify the field-induced color change with the partial sum rule (inset, Fig 6.1(c)): $f \equiv \frac{2c}{N_e \hbar \pi \omega_p^2} \int_{E_1}^{E_2} n\alpha(E,B)\,\mathrm{d}E$ [102]. Here, $N_e = 2$ is the number of electrons per Ni site, $n \simeq 2.13$ is the refractive index, ω_p is the plasma frequency $\equiv \sqrt{\frac{e^2\rho}{m\epsilon_0}}$, e and m are the charge and mass of an electron, ϵ_0 is the vacuum dielectric constant, $\rho = 2.17 \cdot 10^{28}\ m^{-3}$ is the density of Ni sites, c is the speed of light, $E_1 = 2.17$ eV and $E_2 = 2.50$ eV are the energy limits of integration. We find that oscillator strength decreases with applied field and that the overall trend is well described by the magnetization energy $\alpha \int M(B) dB$, where $M(B)$ is the experimental magnetization and α is a (negative) constant [inset, Fig 6.1(c)]. [89, 190] α is large below the critical field due to a combination of spin-charge coupling and Zeeman interactions. [191] Coupling is diminished in the fully polarized state, where the field-induced change in oscillator strength (Δf) is described solely by the Zeeman effect. [192]

6.1.2 Optical response in different polarizations

Figure 6.2(a) summarizes the magnetic field dependent optical properties of $Ni_3V_2O_8$ for the three different polarizations. The overall spectral shape is similar. All three low lying Ni *d-d* excitations ($^3A_{2g} \rightarrow {}^3T_{2g}$, $^3A_{2g} \rightarrow {}^1E_g$ and $^3A_{2g} \rightarrow {}^3T_{1g}$) are observed due to spin-orbit coupling, exchange interaction, and odd parity phonons that hybridize states and break inversion symmetry [14, 157]. The Laporte forbidden $^3A_{2g} \rightarrow {}^3T_{2g}$

and ${}^3A_{2g} \rightarrow {}^3T_{1g}$ excitations are partially polarization dependent. To a first order approximation, we use an octahedral crystal field around the Ni^{2+} center and Racah parameters [193] to extract the crystal field splitting energy Dq=824 cm^{-1}. This value is in excellent agreement with recent results from resonant inelastic x-ray scattering experiments of $Ni_3V_2O_8$ (≈800 cm^{-1}) [185] and the value obtained for NiO (≈880 cm^{-1}) [194].

It is known that the absorption coefficient changes with temperature due to broadened excitations [Fig. 6.2(b)]. At room temperature, $Ni_3V_2O_8$ becomes more reddish-yellow and less greenish. Magnetic field is different; it causes green color enhancement in the crystal [Fig. 6.2(c)]. The field induces spectral changes in all three orientations with a maximum of ≈24% over the energy range of our investigation. It is slightly larger when $\overrightarrow{E} \parallel c$, indicating that spin-charge coupling may be slightly larger in the spine direction (which corresponds to the magnetic hard axis).

It is worth mentioning that the spectra between 1.6 to 12 K are very similar. This indicates that electronic structure is not very sensitive to the complex magnetic phases (high and low temperature incommensurate phases and two commensurate antiferromagnetic spin structures) resulting from the frustration [34]. This finding is different from that in Ref [91].

Exciton behavior is an incisive probe of the Zeeman effect in $Ni_3V_2O_8$. We chose the electric-dipole-allowed exciton centered at ≈2.326 eV as an example because it exists along all three polarizations. As shown in Fig. 6.3(a), the peak position of this exciton shifts to lower energy with field, and its intensity is reduced. Moreover, the trend fits well with the magnetization energy [89]. This result demonstrates that the exciton shift in magnetic field is driven by the Zeeman interaction. With increasing temperature, the effect is reduced due to thermal disorder [Fig. 6.3(b)].

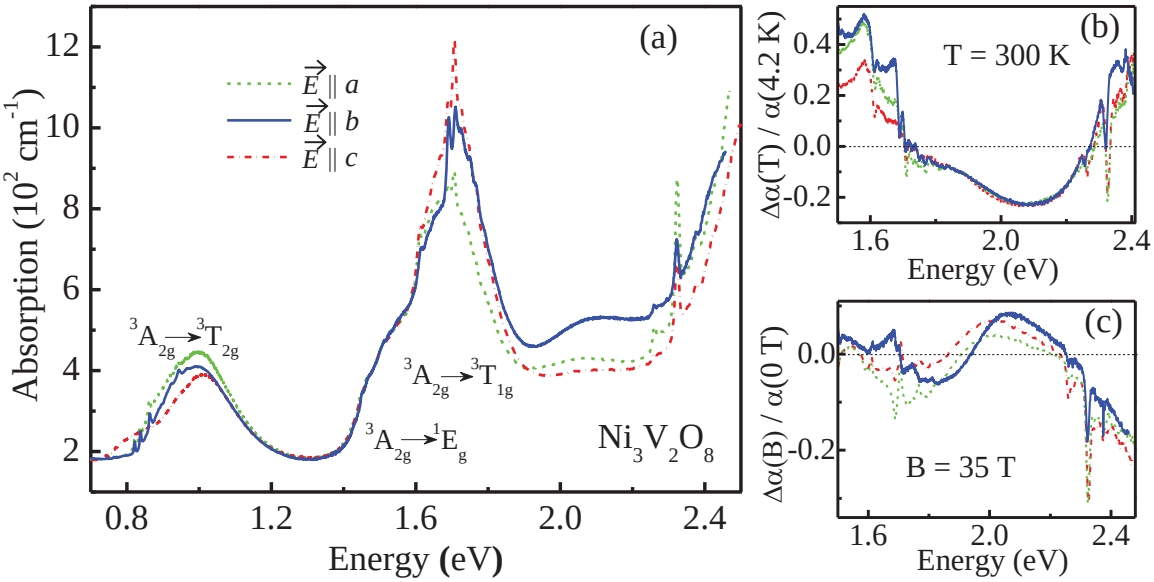

Figure 6.2: (Color online) (a) Absorption coefficient, $\alpha(E)$, of $Ni_3V_2O_8$ in the near-infrared and visible range at 4.2 K in different polarizations. $\vec{E}$ is the electric field vector of the light. (b) Absorption difference spectra $[\frac{\Delta\alpha(T)}{\alpha(4.2\ K)} = \frac{\alpha(300\ K) - \alpha(4.2\ K)}{\alpha(4.2\ K)}]$ in different polarizations showing the absorption change with temperature. (c) Absorption difference spectra $[\frac{\Delta\alpha(B)}{\alpha(0\ T)} = \frac{\alpha(35\ T) - \alpha(0\ T)}{\alpha(0\ T)}]$ at 4.2 K in different polarizations showing how the absorption changes with field.

6.2 Optical imaging of color change with field

Motivated by these spectroscopic findings, we sought direct visual confirmation of the field-induced color change in $Ni_3V_2O_8$. This evidence was obtained by replacing the spectrometer with a black box and taking pictures of the light brought in by optical fiber under various magnetic fields. The setup and photographic outcomes are summarized in Fig. 6.4. Clearly, the color of $Ni_3V_2O_8$ changes with temperature and magnetic field. Upon warming from 1.6 to 300 K, the reddish-yellow aspect of the crystal is enhanced while the green tones are diminished. This is a simple temperature broadening effect. By contrast, application of magnetic field at low temperature enhances the greenish appearance. As discussed below, this is a consequence of combined magnetoelectric coupling and Zeeman interactions. The color differences captured with our black box + camera setup are consistent with the magneto-optical data in Fig. 6.1. To quantify

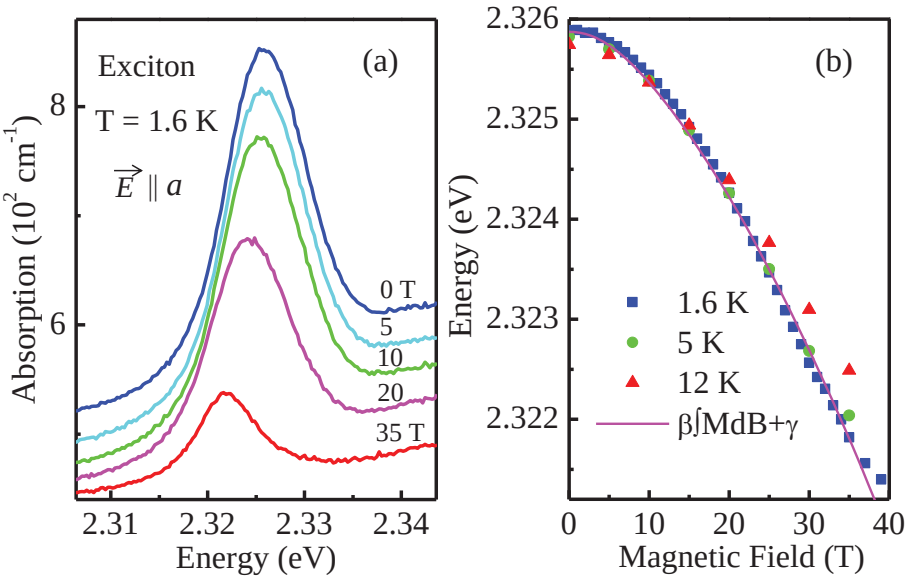

Figure 6.3: (a) Close-up view of the 2.325 eV exciton at selected fields. The spectra are offset along the y-axis for clarity. (d) Peak position vs. magnetic field for the exciton at selected temperatures: 1.6, 5, and 12 K. Relative error bars of these positions are smaller than the symbol size. The integrated magnetization, $\beta \int M(B)dB + \gamma$, at 1.3 K [89] (magenta line) fits well with the trend in the peak position with β=-1.46 and γ=2.3259 eV. Here γ is the zero field energy of the exciton.

how much green color is gained, we calculated the photon intensity in the 2.17 - 2.50 eV spectral range and show the variation $[\frac{\int I(E,B)dE - \int I(E,0\,T)dE}{\int I(E,0\,T)dE}]$ as a function of applied field (Fig. 6.4). Here, $I(E,B)$ is the photon intensity with energy E at magnetic field B. We find that green photon intensity increases by 20% at 35 T and 27% at 45 T - a huge effect.

6.3 Band structures in antiferromagnetic and ferromagnetic phases

To understand the field-induced color change mechanism, we calculated the electronic structure in two different limiting-case spin states and extracted charge density (ρ) differences [195]. The band structure reveals direct gap character in both the anti-

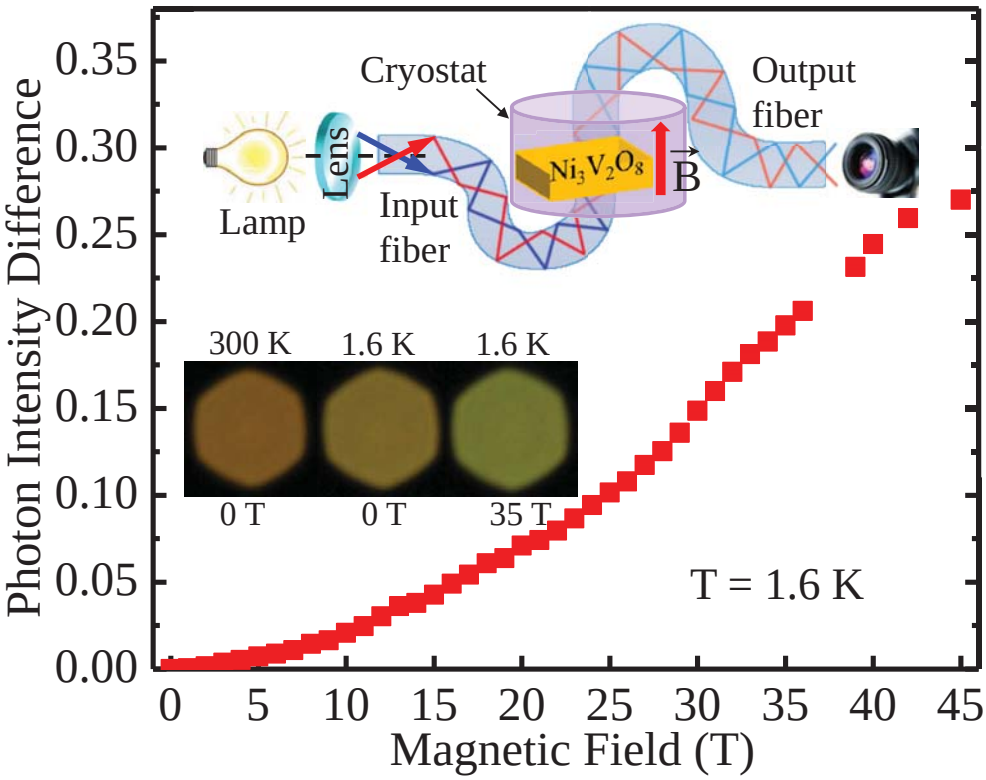

Figure 6.4: Photon intensity difference as a function of magnetic field in the green color range. It represents the green color change shown in the photos. Top inset: schematic view of experimental setup. We took pictures through the optical fibers (1 mm diameter, 370-2000 nm) by Canon Powershot SX30 IS with a Xenon source. Bottom inset: photos of $Ni_3V_2O_8$ single crystals at $B \parallel$ b axis.

ferromagnetic and ferromagnetic phases, although the gap shifts from the Z to the Y point and is predicted to increase slightly in the ferromagnetic state [top panel, Fig. 6.5(a)]. The latter is in agreement with our magneto-optical spectra. To investigate how the band structure evolves between the antiferromagnetic and ferromagnetic states, we gradually increased spin polarization away from the fully compensated situation [bottom panel, Fig. 6.5(a)]. Away from the Y point, the valence band energy systematically decreases with increasing moment. As the fundamental gap excitation shifts from Z in the antiferromagnetic state to Y in the ferromagnetic state, the gap increases. We therefore anticipate that the optical properties will be different at 0 T and full field, in agreement with our experimental findings.

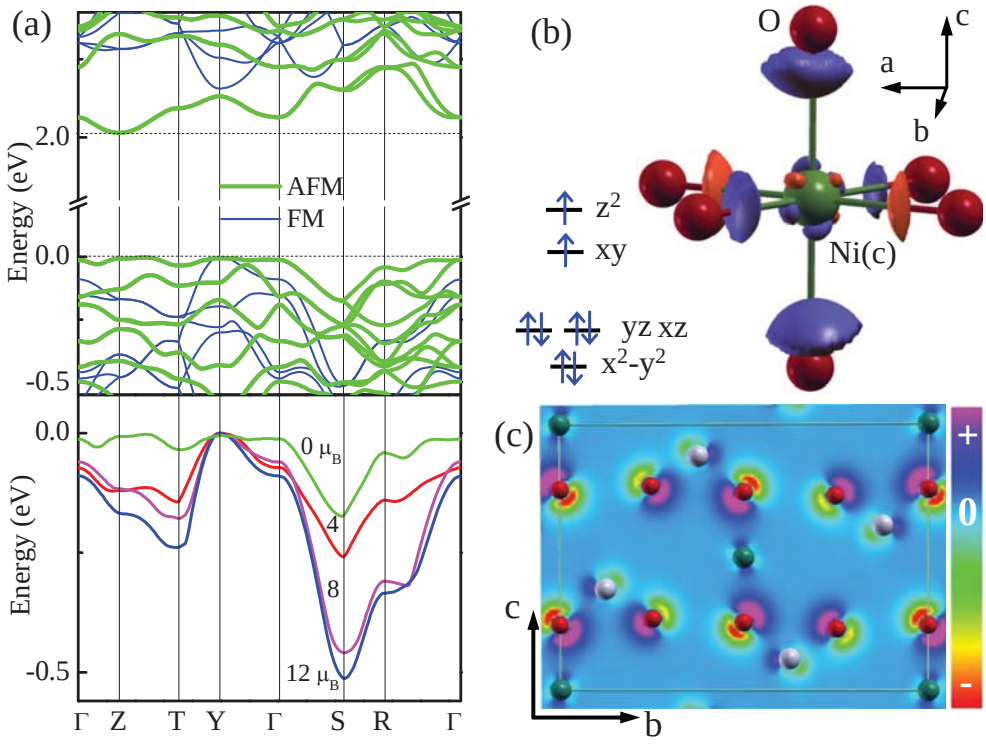

Figure 6.5: (a) Top panel: band structure of $Ni_3V_2O_8$ with antiferromagnetic and ferromagnetic ordering in the region of the band gap. The calculated band gap is 2.02 and 2.15 eV in antiferromagnetic and ferromagnetic state, respectively. In the ferromagnetic state, only the majority band structure is shown for clarity. The valence and conduction band edges in antiferromagnetic state are indicated by horizontal dashed lines. Computed Hubbard Us are 4.0 and 4.2 eV for Ni(c) and Ni(s) ions, respectively [116]. Bottom panel: valence band structure with total spin moment fixed at 0, 4, 8 and 12 μ_B. (b) Charge density difference $[\Delta\rho{=}\rho(FM) - \rho(AFM)]$ around the Ni cross-tie center. The isosurface is $\pm 0.014\ e/\mathring{A}^3$. The positive value is rendered by blue color, and negative value is indicated by red color. The other diagram illustrates the electron configuration of the Ni^{2+} (d^8). (c) $\Delta\rho$ projected onto the bc plane. The charge density scale is from -0.08 to 0.04 $e/\mathring{A}^3$.

6.4 Charge density differences

The charge density difference between the two limiting-case spin states captures the interplay between charge and magnetism in $Ni_3V_2O_8$. Figure 6.5(b) displays total charge density difference contours around the Ni cross-tie center. This plot reveals that the charge density of the d_{xy} and $d_{3z^2-r^2}$ states increases in the ferromagnetic phase, whereas that of the d_{xz} and d_{yz} states is reduced. Due to Ni-O bonding, O $2p$ density near the Ni(c) site is simultaneously enhanced. We also projected the charge density difference onto the bc plane [Fig. 6.5(c)]. In the ferromagnetic state, O $2p$ state density changes by approximately $\pm 3\%$, ρ of the Ni $3d$ states changes by about $\pm 1.5\%$, and ρ of the V $3d$ states changes less than $\pm 1\%$ [196]. These findings demonstrate that charge density (especially that around the O center) can be redistributed according to the spin state. This redistribution modifies the charge excitations in $Ni_3V_2O_8$. Changes in local charge density also drive magnetoelectric effects in molecular systems. [197]

Bringing these results together, we propose that the field-induced blue shift of the optical band gap in $Ni_3V_2O_8$ can be understood in terms of dynamic magnetoelectric coupling. Zeeman interactions certainly move the system toward the fully polarized state in applied field. But what really accelerates the process is the spin-charge coupling in which the higher field spin state redistributes the charge density around the Ni and O sites, differentiating it from that under zero field conditions. Polarizability on the Ni and O centers provides this flexibility. Since nearest-neighbor magnetic coupling arises from superexchange interactions mediated by Ni-O-Ni bonds, the O $2p$ charge density also becomes asymmetric, increasing near the Ni sites and decreasing on the opposite side. These field-induced charge density distortions modify the electronic structure and shift the band gap toward higher energy. Once the system is in the fully polarized state, the spin moment is saturated and this mechanism no longer contributes.

Since $Ni_3V_2O_8$ is an insulator, we can use the ratio of the gap difference to the

magnetization energy in the fully polarized state to estimate the magnitude of spin-charge coupling. Using a magnetization energy of 4.8 meV [89] and the 50 meV blue shift of the gap through the 37 T critical field, we find a coupling constant of $\approx$10, which is very large. It is worth mentioning that the static polarization induced by the field has a maximal value of 60 μC/m^2 and goes to zero above 12 T [89]. This indicates that static coupling and the ability to manipulate magnetization with electric field different takes place with a mechanism. [89, 198]

Chapter 7

Magnetochromism in frustrated $R\mathbf{In}_{1-x}\mathbf{Mn}_x\mathbf{O}_3$ (R=Tb, Dy)

We measured the magneto-optical properties of frustrated geometric $R\mathrm{In}_{1-x}\mathrm{Mn}_x\mathrm{O}_3$ (R=Tb, Dy) in order to investigate the effect of large spin-orbit in competition with magnetoelectric coupling on the interplay between charge and magnetism. $TbInO_3$ shows a large magnetochromic effect. Moreover, the f electron excitations in $DyInO_3$ change dramatically in the field, a result from the Zeeman effect. When doped with Mn ions, magnetization of the material is increased, and Mn d-d excitations emerge in the visible range. Below, we discuss the color band, f electron crystal field excitation, and Mn^{3+} d-d excitation behavior at low temperature and high magnetic field along with high field magnetization that accompanied this work.

7.1 High field magnetization to evaluate the saturation field

Figure 7.1 displays the isothermal magnetization of $R\mathrm{In}_{1-x}\mathrm{Mn}_x\mathrm{O}_3$ as a function of magnetic field up to 65 T. The moments grows rapidly below 10 T, above which, the change in moments decrease and the subsequent curves are almost linear. The measured moments of $TbInO_3$ and $DyInO_3$ are $\sim 6.9\mu_B/\mathrm{Tb}^{3+}$ and $\sim 8.1\mu_B/\mathrm{Dy}^{3+}$ at 65 T, respectively, although it is not saturated at this field. The values are approaching to the free ion magnetic moment of Tb^{3+} ($9\mu_B$) and Dy^{3+} ($10.6\mu_B$) and are expected to saturate at $\sim$200 T. Mn substitution introduces magnetic impurity in the lattice and have slightly higher saturation magnetization compared with the unsubstituted analogs. dM/dH curve indicates a maximum at $\sim$0.8 T for $DyInO_3$, which is a spin glass transition also observed in the *ac* susceptibility measurements at low temperature. [199]

7.2 Magnetochromic effect in $R\mathrm{InO}_3$

Figure 7.2(a) displays the optical response of $TbInO_3$. We assign the strong absorption at $\sim$20000 cm^{-1} as the O $2p$ to In $5s$ charge transfer excitation. [200] A 2.14 eV direct band gap is extracted from a linear fit of $(\alpha \cdot E)^2$ vs. E, where α is the absorption coefficient and E is the photon energy. [102] The absorption in the tail of the transition increases with field, probably due to changes in edge gap states. The field-induced absorption difference spectra is shown in the inset of Fig. 7.2(a) with a maximum change of 7% at $\sim$14000 cm^{-1}. As a consequence, this system absorbs fewer photons in the red and yellow color range in high magnetic field and appears less orange. This change occurs because the magnetic ordering is driven toward a fully polarized state in applied field and causes an electronic structure change through the spin-charge coupling effect. We can quantify the field-induced color change with the integrated intensity

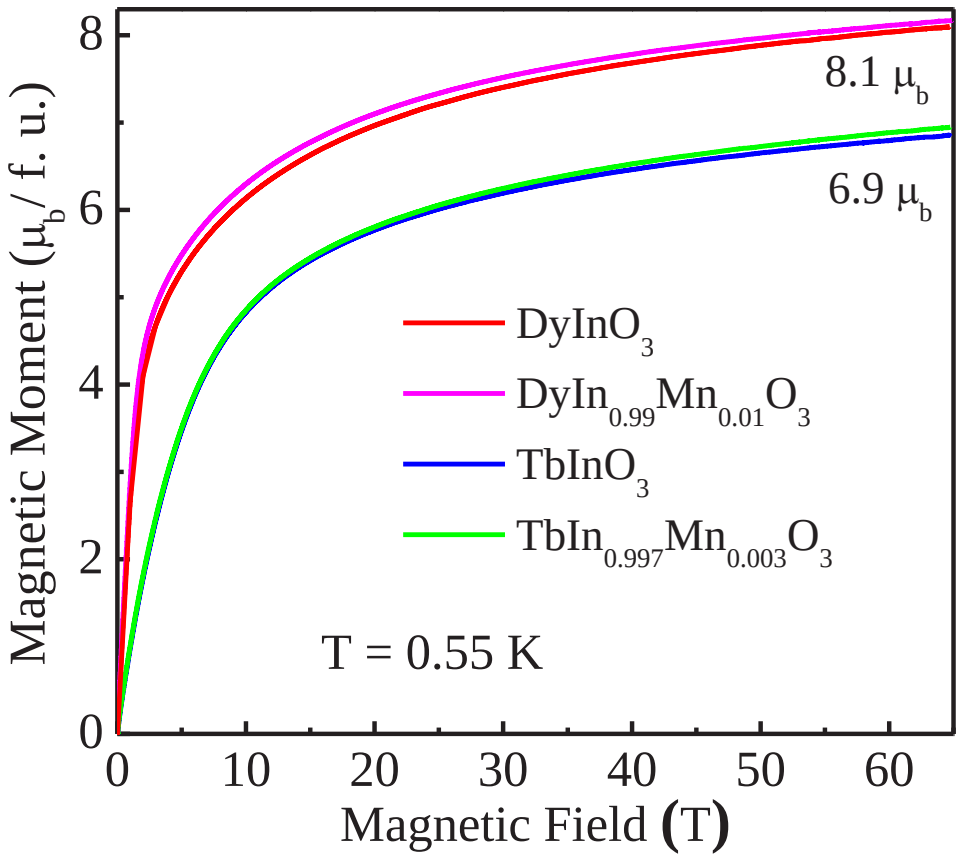

Figure 7.1: (Color online) (a) Isothermal magnetization of $DyInO_3$, $DyIn_{0.99}Mn_{0.01}O_3$, $TbInO_3$, and $TbIn_{0.997}Mn_{0.003}O_3$ as a function of magnetic field at 0.55 K.

$I(B) = \int_{\omega 1}^{\omega 2} \Delta\alpha(\omega, B)d\omega$, where $\omega 1$ and $\omega 2$ are the frequencies of integration. This quantity represents the change in the excitation intensity in the field. Overall, $I(B)$ increases with field, and the field-induced change is decreased at higher temperatures due to thermal disorder effects [as shown in Fig. 7.2(b)]. We find that $I(B)$ trend is well described by the magnetization energy $C \int M(B)dB$, where $M(B)$ is the experimental magnetization and C is a constant. This finding indicates that Zeeman energy is the driving force for the field-induced color change.

Chemical doping is an effective way of tailing magnetic and color properties. [111] When substituting magnetic Mn^{3+} into the $TbInO_3$, the color goes from orange to green. This is because the Mn^{2+} *d-d* excitations appear in the visible range, as shown

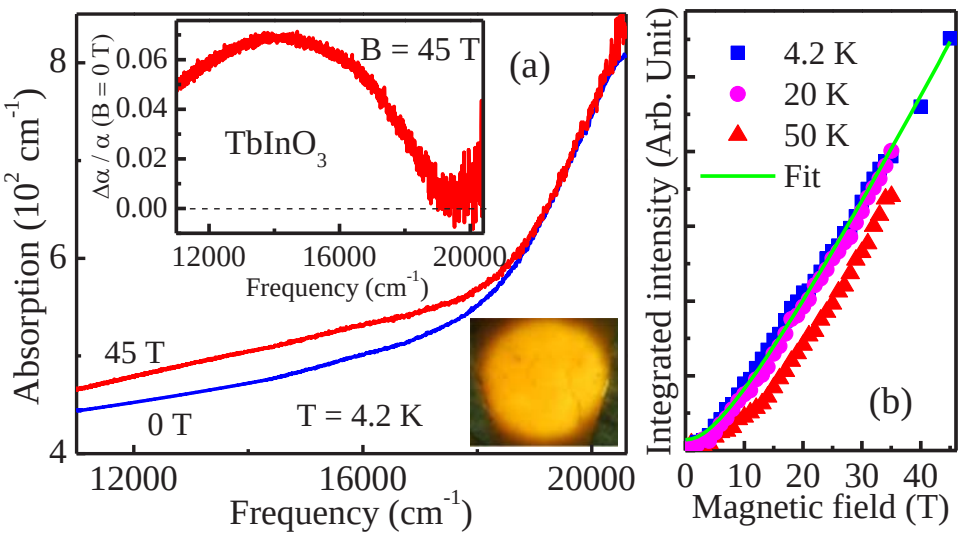

Figure 7.2: (Color online) (a) Absorption coefficient, α(E), of $TbInO_3$ in the field of 0 and 45 T at 4.2 K. Top inset: Absorption difference spectra $[\frac{\Delta\alpha(B)}{\alpha(0\ T)}=\frac{\alpha(45\ T)-\alpha(0\ T)}{\alpha(0\ T)}]$. Bottom inset: Transmittance image of a polished $\sim$100 μm sample. (b) Integrated intensity in the range of excitation edge (12000 - 17000 cm^{-1}) as a function of magnetic field at selected temperatures: 4.2, 20 and 50 K. The integrated magnetization $C_1 \int M(B)dB$ fits well with the integrated intensity trend, where $M(B)$ is the magnetization and C_1 is a constant.

in Figure 7.3(a). These broad transitions at $\sim$15900 and 17200 cm^{-1} are assigned as on-site excitations from d_{xy}/d$_{x^2-y^2}$ and d_{yz}/d$_{zx}$ to $d_{3z^2-r^2}$. [101]Fig. 7.3(a) inset displays the field-induced absorption difference spectra. The two peaks with opposite signs are attributed to the field-induced shift of the *d*-*d* excitations to lower energy. The shift in the on site transitions can be quantified by the absolute value of the integrated intensity ($|I(B)|$). Figure 7.3(b) shows $|I(B)|$ increases with field. The overall shape is less well fitted by the magnetization energy, which indicates that doped magnetic ions introduce magnetic disorder to the spin-charge coupling effect. This result is in consistent with that from *ac* susceptibility measurements. [199] The field-induced shift is reduced at higher temperatures due to thermal disorder effect.

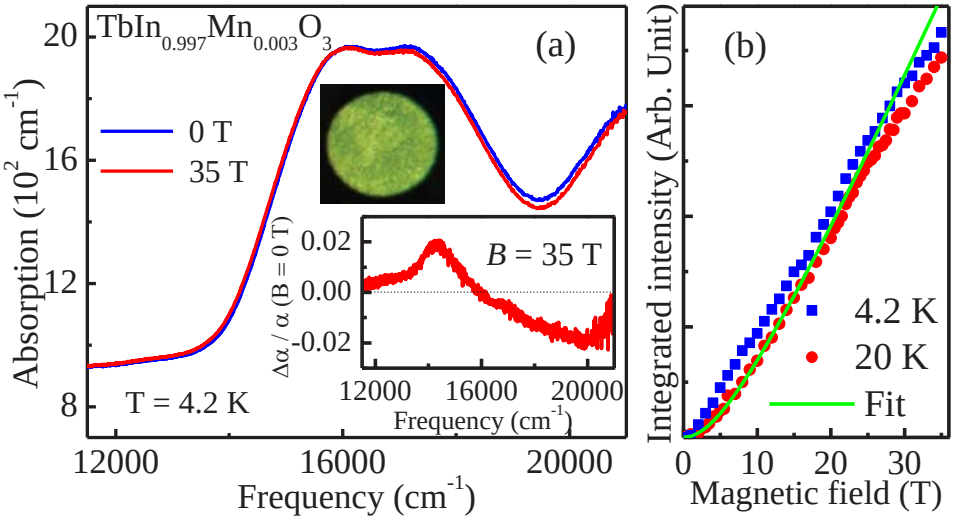

Figure 7.3: (Color online) (a) Absorption coefficient, α(E), of $TbIn_{0.997}Mn_{0.003}O_3$ in fields of 0 and 35 T at 4.2 K. Top inset: Transmittance image of a polished ~33 μm sample. Bottom inset: Absorption difference spectra $[\frac{\Delta\alpha(B)}{\alpha(0\ T)}=\frac{\alpha(35\ T)-\alpha(0\ T)}{\alpha(0\ T)}]$. (b) Absolute value of integrated intensity in the range of excitation edge (12000 - 16000 cm^{-1}) as a function of magnetic field at selected temperatures: 4.2 and 20 K. The integrated magnetization $C_2 \int M(B)dB$ fits less well with the integrated intensity trend compared to the result of $TbInO_3$, where $M(B)$ is the magnetization and C_2 is a constant.

7.3 Dy^{3+} crystal field excitations shift in magnetic field

The optical and magnetic properties of $DyInO_3$ arise from $4f$ electrons in the Dy^{3+} centers and their interaction. Figure 7.4(a) displays the magneto-optical response of $DyInO_3$. The overall absorption in the visible range is low, which results in the white color of the material. A great deal of fine structure is observed. These features are well known Dy^{3+} crystal field transitions from ground state $^6H_{15/2}$ to excited states. [201] With applied magnetic field, these $4f$ excitations shift to higher energy [Fig. 7.4(a) inset]. A close up view of selected $4f$ excitations is shown in Fig. 7.4(b). We assigned the two multiplet clusters as $^6H_{15/2} \rightarrow {}^6F_{3/2}$ and $^6H_{15/2} \rightarrow {}^6F_{1/2}$ excitations. [201] The site group controls the symmetry properties of crystal field excitation levels. Group

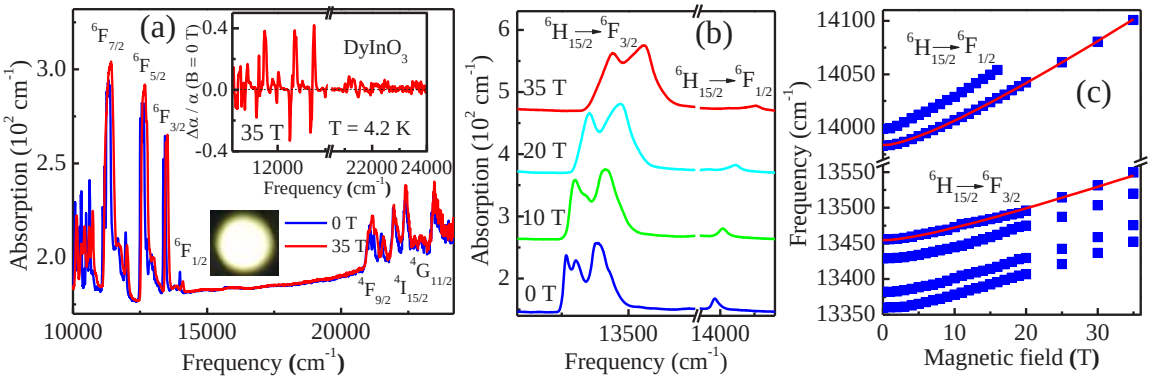

Figure 7.4: (Color online) (a) Absorption coefficient, α(E), of $DyInO_3$ in magnetic fields of 0 and 35 T at 4.2 K. Top inset: Absorption difference spectra $[\frac{\Delta\alpha(B)}{\alpha(0\ T)}=\frac{\alpha(35\ T)-\alpha(0\ T)}{\alpha(0\ T)}]$. Bottom inset: Transmittance image of a polished $\sim$300 μm sample. (b) Close-up view of the the f electron excitations ${}^6H_{15/2} \rightarrow {}^6F_{3/2}$ and ${}^6H_{15/2} \rightarrow {}^6F_{1/2}$ at selected fields. (c) Peak position vs. magnetic field for the f manifold excitations. The red lines are the theoretical fit using $C_3 \int M(B)dB + \gamma$, where C_3 is a constant and γ is the zero field energy of the excitation.

theory predicts that the ${}^6F_{3/2}$ level is split into two components because of spin-orbit coupling and the trigonal field symmetry around Dy^{3+} centers. [202] In $DyInO_3$, two different Dy^{3+} centers occupy positions with C_{3v} and C_3 site symmetry, respectively. [202] The slightly different crystal field at these two sites causes each level to split into 2 features. Therefore, a symmetry analysis predicts total four lines in the ${}^6H_{15/2} \rightarrow$ ${}^6F_{3/2}$ excitation and two in ${}^6H_{15/2} \rightarrow$ ${}^6F_{1/2}$ excitation, in excellent agreement with our spectroscopic results.

The zeeman effect is an incisive probe of the magnetic response of Dy^{3+} $4f$ electrons. With increasing magnetic field, the excitations shift to higher energy. It is a combination of Zeeman effects from both ground and excited states. Moreover, the intensity of features arising from C_3 site decreases. These $4f$ electron excitations behaviors in the field are summarized in Fig. 7.4(c). Overall, the peak positions blue shift with field, and the trend fits well with the magnetization energy $C_3 \int M(B)dB + \gamma$, where C_3 and γ are fitting constants and β is the zero field energy of the excitation. This result demonstrates that the rare earth excitation shift in magnetic field is driven

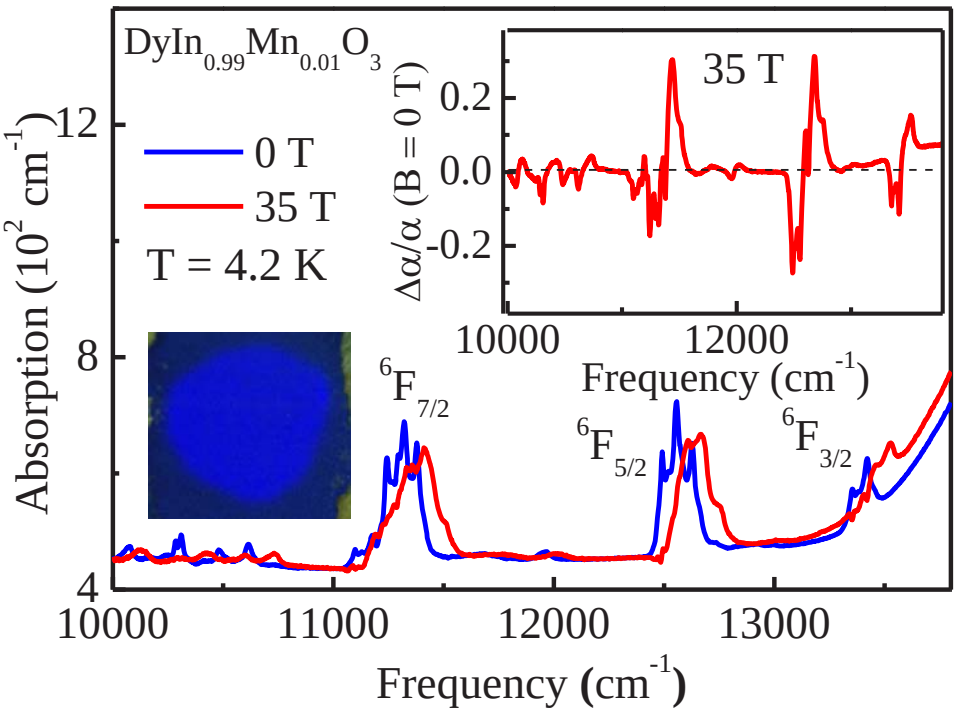

Figure 7.5: (Color online) (a) Absorption coefficient, α(E), of $DyIn_{0.99}Mn_{0.01}O_3$ in fields of 0 and 35 T at 4.2 K. Top inset: Absorption difference spectra $[\frac{\Delta\alpha(B)}{\alpha(0\ T)}=\frac{\alpha(35\ T)-\alpha(0\ T)}{\alpha(0\ T)}]$. Bottom inset: Transmittance image of a polished ~100 μm sample. The Mn is too heavy to resolve the color band.

by the Zeeman interaction. β is larger for the $^6H_{15/2}\rightarrow\ ^6F_{1/2}$ excitation because of a smaller M_J quantum number in the $^6F_{1/2}$ level. Assuming the Zeeman splitting in the excited states is neglectable, we can obtain the energy shift of these excitations by a simplified Brillouin function: $\Delta E=\mu B tanh(\frac{\mu B}{K_B T})$. [7] Using μ=8.1 μ_B, the relation fits the magnetization energy very well, indicating the peak position shift is dominated by the Zeeman effect of the ground state.

To investigate how the substituted magnetic ions impact on the $4f$ electron excitations, we doped Mn^{3+} into $DyInO_3$, and the d-d excitations from Mn^{3+} make the color blue. The behavior of crystal field excitations in $DyIn_{0.99}Mn_{0.01}O_3$ is the same as that in the parent compound, as shown in Fig. 7.5. This result indicates that the lightly doped Mn^{3+} has no effect on the $4f$ electrons and d-f electron interaction is very small.

The magneto-optical results in $GdInO_3$ are very similar as those in $DyInO_3$ and not shown here. In addition to the spin-orbit coupling induced optical properties change, other strategies including spin-flop, magnetic ordering transition can also induce electronic structure change through the mechanisms of *d*-*d* excitation intensity change and band gap shift. [14, 199]

Chapter 8

Conclusions

In this dissertation I present spectroscopic investigations of several different types of complex oxides through a series of field- and temperature-driven transformations. Our target materials are selected for the fundamental scientific problems including the optical gap tuning, lattice and charge dynamics, spin-charge coupling, and the magnetochromic effect.

The first class of problems focused on ferroelectric $\rightarrow$ paraelectric phase transition, controllable band gap, and spiral order $\rightarrow$ homogeneous state transition in $BiFeO_3$. In order to elucidate the nature of the ferroelectric phase transition, we investigated the optical properties of in $BiFeO_3$ as a function of particle size. The systematic red shifting of the A_1(TO1) vibrational mode with decreasing size strongly supports its assignment as the soft mode driving the ferroelectric transition. Moreover, this A1 mode is underdamped, suggesting a first order nature. Several E symmetry modes are strongly damped in spectrum of the 16 nm particles, indicative of a size-induced approach to the cubic paraelectric phase in small particles. The consequences of strain induced by finite size effects and compressive strength introduced by substrate are of fundamental importance to understand the chemical bonding and hybridization. It is know that the efficiency of $BiFeO_3$ based devices is limited due by the $\sim$2.7 eV band

gap. It is red shifted ∼0.3 eV in the nanoscale particles and blue shifted ∼0.4 eV in the tetragonal film, proving that nanoscale $BiFeO_3$ is promising for flexible ferroelectric photovoltaic devices. [10, 105]

To investigate the spiral order → homogeneous state transition in chemically-substituted $BiFeO_3$, we used magnetic field-induced changes in the underlying magnon sideband as a probe of spin spiral behavior. The B–T–x diagram reveals precisely how the critical field decreases with rare earth substitution, a trend that destabilizes the antiferromagnetic spiral phase. The magneto-optical contrast demonstrates that spiral magnetic order is quenched when x∼0.20. The Ginzburg-Landau free energy allows us to understand this trend as the combined effect of larger anisotropy constant, longer spiral wavelength, and increased susceptibility. Nd^{3+} is shown to be more effective in quenching the spin spiral compared with La^{3+}. These findings demonstrate that chemical substitution can help control field-induced magnetic ordering transitions, opening up a variety of possibilities for spintronic and the development of magnetic ferroelectrics. [111]

A second class of problems is related to how to identify large spin-charge coupling effect. We began with several materials design strategies including collective transitions, spin-orbit coupling, doped magnetic chromophore ions. One of our main findings is the discovery of magnetochromism in one of the worlds oldest and most iconic antiferromagnetic materials, α-Fe_2O_3. Oscillator strength changes in d-d excitation range show a first order transition at critical field. These on site excitations are in the visible range and responsible for the reddish color of α-Fe_2O_3. Therefore, this system absorbs fewer photons in the red color range and appears more red in high magnetic field. This chameleonic effect arises because the Fe^{3+} on-site excitations are intrinsically coupled to magnetic ordering. The softening of magnon sideband at critical field indicate larger direct exchange [28] and smaller superexchange in the high field phase. The exciton

pattern reveals $C2$ monoclinic symmetry in the high field phase with consideration of Dzyaloshinskii-Moriya effect. [78, 79] The discovery of magnetochromism involving collective transition in this model system motivates our group's continuing study of charge-spin coupling in iron-based solids, and nano-scale structure to simultaneously reduce the critical field and amplify the magnetic response. [8, 14, 203, 204]

Spin-charge interaction underpins much of the rich physics in multifunctional oxides and provide a mechanism for cross-coupling in external field. We reveal magnetic field-induced blue shifts of the band gap in $Ni_3V_2O_8$. The change is more effective than those driven by temperature, anticipating a more greenish appearance in the fully polarized state. This color change is verified with direct photographic images. Electronic structure calculation results indicate that the magneto-optical result emanates from charge density differences around the Ni and O centers in high field. These findings reveal that key electronic energy scales like the charge gap can be tuned to a surprising extent with external stimuli. [205]

To test the spin-orbit coupling effects and the role of introducing doped magnetic chromophore on the spin-charge coupling, we measure the magnetic and magneto-optical properties of $R\mathrm{In}_{1-x}\mathrm{Mn}_x\mathrm{O}_3$. Magnetization results show the saturation moments of $TbInO_3$ and $DyInO_3$ at 65 T are $\sim 6.9\mu$B/Tb3+ and $\sim 8.1\mu$B/Dy3+. The spectroscopic results show a large spin-charge coupling effect in $TbInO_3$. Moreover, the f electron excitations in $DyInO_3$ change dramatically in the field, a result of the Zeeman effect. When doped with Mn ions, the magnetic response that change with field is increased, and Mn d-d excitations emerge in the visible range. These findings improve the fundamental understanding of the impact of rare earth element on large spin-charge coupling. [199]

Taken together, these comprehensive findings advance our knowledge of the interplay between charge and magnetism with external magnetic field, identity collective

transitions like spin-flop and magnetic phase transition which are excellent strategies for the development of next-generation color change materials. Moreover, they motivate fundamental research on other complex oxides under extreme conditions and away from the static limit. In the future, other strategies for achieving large spin-charge coupling should be tested, including collective transitions like ferroelectric phase transition, lattice structure change, and surface strain effect in finite size particles.

Bibliography

[1] C. Krey, S. Legl, S. R. Dunsiger, M. Meven, J. S. Gardner, J. M. Roper, and C. Pfleiderer, Phys. Rev. Lett. **108**, 257204 (2012).

[2] M. L. Foo, Y. Wang, S. Watauchi, H. W. Zandbergen, T. He, R. J. Cava, and N. P. Ong, Phys. Rev. Lett. **92**, 247001 (2004).

[3] T. Goto, T. Kimura, G. Lawes, A. P. Ramirez, and Y. Tokura1, Phys. Rev. Lett. **92**, 257201 (2004).

[4] M. H. Phan, N. A. Frey, M. Angst, J. de Groot, B. C. Sales, D. G. Mandrus, and H. Srikanth, Solid State Commun. **150**, 341 (2010).

[5] P. Zubko, S. Gariglio, M. Gabay, P. Ghosez, and J.-M. Triscone, Annu. Rev. Condens. Matter Phys. **2**, 141 (2011).

[6] L. I. Vergara, J. Cao, N. Rogado, Y. Q. Wang, R. P. Chaudhury, R. J. Cava, B. Lorenz, and J. L. Musfeldt, Phys. Rev. B **80**, 052303 (2009).

[7] N. W. Ashcroft, and N. D. Mermin, Solid state physics (Brooks Cole, 1976).

[8] X. S. Xu, T. V. Brinzari, S. Lee, Y. H. Chu, L. W. Martin, A. Kumar, S. McGill, R. C. Rai, R. Ramesh, V. Gopalan, S. -W. Cheong, and J. L. Musfeldt, Phys. Rev. B **79**, 134425 (2009).

[9] T. V. Brinzari, P. Chen, Q. -C. Sun, J. Liu, L. -C. Tung, Y. J. Wang, J. Singleton, J. A. Schlueter, J. L. Manson, M. -H. Whangbo, A. P. Litvinchuk, and J. L. Musfeldt, Phys. Rev. Lett. **110**, 237202 (2013).

[10] P. Chen, X.S. Xu, C. Koenigsmann,A. C. Santulli, S. S. Wong, and J. L. Musfeldt, Nano Lett. **10**, 4526 (2010).

[11] P. G. Russell, D. S. McClure and J. W. Stout, Phys. Rev. Lett. **16**, 176 (1966).

[12] V. V. Eremenko, Yu. G. Litvinenko, and V. I. Myatlik, JETP Lett. **12**, 47 (1970).

[13] V. V. Eremenko and E. G. Petrov, Adv. Phys. **26**, 31 (1977).

[14] P. Chen, N. Lee, S. McGill, S. -W. Cheong, and J. L. Musfeldt, Phys. Rev. B **85**, 174413 (2012).

[15] J. H. Lee, P. e. Naumov, I. H. Chung, S. C. Lee, J. Phys. Chem. A **115**, 10087 (2011).

[16] A. G. Gavriliuk, V. V. Struzhkin, I. S. Lyubutin, S. G. Ovchinnikov, M. Y. Hu, and P. Chow, Phys. Rev. B **77**, 155112 (2008).

[17] A. E. Smith, H. Mizoguchi, K. Delaney, N. A. Spaldin, A. W. Sleight, M.A. Subramanian, J. Am. Chem. Soc. **131**, 17084 (2009).

[18] G. Le Bras, D. Colson, A. Forget, N. Genand-Riondet, R. Tourbot, and P. Bonville, Phys. Rev. B **80**, 134417 (2009).

[19] S. J. Pearton, C. R. Abernathy, M. E. Overberg, G. T. Thaler, D. P. Norton, N. Theoderopoulou, A. F. Hebard, Y. D. Park, F. Ren, J. Kim, and L. A. Boatner, J. Appl. Phys. **93**, 1 (2003)

[20] Ü. Özgür, Ya. I. Alivov, C. Liu, A. Teke, M. A. Reshchikov, S. Doğan, V. Avrutin, S.-J. Cho, and H. Morkoç, J. Appl. Phys. **98**, 041301 (2005).

[21] K. Uchida, N. Miura, J. Kitamura, H. Kukimoto, Phys. Rev. B **53**, 4809 (1996).

[22] S. H. Jhang, M. Margan ska, Y. Skourski, D. Preusche, M. Grifoni, J. Wosnitza, and C. Strunk, Phys. Rev. Lett. **106**, 096802 (2011).

[23] P. Chen, B. S. Holinsworth, K. R. OŃeal, T. V. Brinzari, N. Rogado, Y. Q. Wang, S. McGill, R. J. Cava, B. Lorenz and J. L. Musfeldt, submitted.

[24] R. J. Zeches, M. D. Rossell, J. X. Zhang, A. J. Hatt, Q. He, C.-H. Yang, A. Kumar, C. H. Wang, A. Melville, C. Adamo, G. Sheng, Y.-H. Chu, J. F. Ihlefeld, R. Erni, C. Ederer, V. Gopalan, L. Q. Chen, D. G. Schlom, N. A. Spaldin, L. W. Martin, and R. Ramesh, Science **326**, 977 (2009).

[25] K. Y. Yun, D. Ricinschi, T. Kanashima, M. Noda, and M. Okuyama, Jpn. J. Appl. Phys., Part 2 **43**, L647 (2004).

[26] D. Ricinschi, K. -Y. Yun and M. Okuyama, J. Phys.: Condens. Matter **18**, L97 (2006).

[27] J. B. Neaton, C. Ederer, U. V. Waghmare, N. A. Spaldin, and K. M. Rabe, Phys. Rev. B **71**, 014113 (2005).

[28] E. J. Samuelsen and G. Shirane, Phys. Status Solidi **42**, 241 (1970).

[29] S. Foner, Y. Shapira, Phys. Lett. **29A**, 276 (1969).

[30] Y. Shapira, Phys. Rev. **184**, 589 (1969).

[31] J. Wang, J. B. Neaton, H. Zheng, V. Nagarajan, S. B. Ogale, B. Liu, D. Viehland, V. Vaithyanathan, D. G. Schlom, U. V. Waghmare, N. A. Spaldin, K. M. Rabe, M. Wuttig, and R. Ramesh, Science **299**, 1719 (2003).

[32] S. W. Cheong and M. Mostovoy, Nat. Mater. **6**, 13 (2007).

[33] M. Angst, R. P. Hermann, A. D. Christianson, M. D. Lumsden, C. Lee, M.-H. Whangbo, J.-W. Kim, P. J. Ryan, S. E. N. E. Nagler, W. Tian, R. Jin, B. C. Sales, and D. Mandrus, Phys. Rev. Lett. **101**, 227601 (2008).

[34] G. Lawes, M. Kenzelmann, N. Rogado, K. H. Kim, G. A. Jorge, R. J. Cava, A. Aharony, O. Entin-Wohlman, A. B. Harris, T. Yildirim, Q. Z. Huang, S. Park, C. Broholm, and A. P. Ramirez, Phys. Rev. Lett. **93**, 247201 (2004).

[35] N. A. Spaldin, M. Fiebig, Science **309**, 391 (2005).

[36] M. Fiebig, J. Phys. D **38**, R123 (2005).

[37] J. P. Rivera, Ferroelectrics **161**, 147 (1993).

[38] B. B. Krichevtsov, V. V. Pavlov, and R. V. Pisarev, JETP Lett. **49**, 535 (1989).

[39] G. T. Rado, J. M. Ferrari, and W. G. Maisch, Phys. Rev. B **29**, 4041 (1984).

[40] I. E. Dzyaloshinskii, JETP **10** 628, (1959).

[41] D. N. Astrov, JETP **11** 708, (1960).

[42] R. Seshadri and N. A. Hill, Chem. Mater. **13**, 2892 (2001).

[43] L. Balents, Nature (London) **464**, 199 (2010).

[44] V. Tsurkan, S. Zherlitsyn, S. Yasin, V. Felea, Y. Skourski, J. Deisenhofer, H.-A. Krug von Nidda, J. Wosnitza, and A. Loidl, Phys. Rev. Lett. **110**, 115502 (2013).

[45] M. Saito, R. Higashinaka, and Y. Maeno, Phys. Rev. B **72**, 144422 (2005).

[46] N. A. Hill, J. Phys. Chem. B **104**, 6694 (2000).

[47] G. Catalan and J. F. Scott, Adv. Mater. **21**, 2463 (2009)

[48] A. P. Ramirez, Annu. Rev. Mater. Sci. **24**, 453 (1994).

[49] R. P. S. M. Lobo, R. L. Moreira, D. Lebeugle, and D. Colson, Phys. Rev. B **76**, 172105 (2007).

[50] P. W. Baumeister, Phys. Rev. **121**, 359 (1961).

[51] R. M. Macfarlane and J. W. Allen, Phys. Rev. B **4**, 3054 (1971).

[52] S. R. Basu, L. W. Martin, Y. H. Chu, M. Gajek, R. Ramesh, R. C. Rai, X. Xu, and J. L. Musfeldt, Appl. Phys. Lett. **92**, 091905 (2008).

[53] O. G. Holmes, and D. S. McClure, J. Chem. Phys. **26**, 1686 (1957).

[54] L. A. Marusak, R. Messier, and W. B. White, J. Phys. and Chem. Solids **41**, 981 (1980).

[55] J. Frenkel, Phys. Rev. **37**, 17 (1931).

[56] H. Matsumoto, K. Saito, M. Hasuo, S. Kono, and N. Nagasawa, Solid State Commun. **97**, 125 (1996)

[57] P. W. Anderson, Phys. Rev. **86**, 694 (1952).

[58] R. L. Greene, D. D. Sell, W. M. Yen, and A. L. Schawlow, Phys. Rev. Lett. **15**, 656 (1965).

[59] P. Fischer, M. Polomska, I. Sosnowska, and M. Szymanskig, J. Phys. C: Sol. Stat. Phys. **13**, 1931 (1980).

[60] D. Lebeugle, D. Colson, A. Forget, M. Viret, P. Bonville, J. F. Marucco, S. Fusil, Phys. Rev. B **76**, 024116 (2007).

[61] V. V. Shvartsman, W. Kleemann, R. Haumont, J. Kreisel, Appl. Phys. Lett. **90**, 172115 (2007).

[62] I. Sosnowska, T. Peterlin-Neumaier, and E. Steichele, J. Phys. C:Solid State Phys. **15**, 4835 (1982).

[63] D. Lebeugle, D. Colson, A. Forget, M. Viret, A. M. Bataille, A. Gukasov, Phys. Rev. Lett. **100**, 227602 (2008).

[64] A. M. Kadomtseva, A. K. Zvezdin, Y. F. Popov, A. P. Pyatakov, and G. P. Vorob'ev, Jetp Lett. **79**, 571 (2004).

[65] The homogeneous phase is a collinear phase, but spin is canted due to the Dzyaloshinski-Moriya effect, resulting in weak ferromagnetism.

[66] M. Ramazanoglu, W. Ratcliff, H. T. Yi, A. A. Sirenko, S. -W. Cheong, and V. Kiryukhin, Phys. Rev. Lett. **107**, 067203 (2011).

[67] A. Kadomtseva, Yu. Popov, G. Vorob'ev, and A. Zvezdin, Physica B **211**, 327 (1995).

[68] S. A. T. Redfern, C. Wang, J.W. Hong, G. Catalan, J. F. Scott, J. Phys.: Cond. Mat. **20**, 452205 (2008).

[69] A. Kumar, R. C. Rai, N. J. Podraza, S. Denev, M. Ramirez, Y. H. Chu, L. W. Martin, J. Ihlefeld, T. Heeg, J. Schubert, D. G. Schlom, J. Orenstein, R. Ramesh, R. W. Collins, J. L. Musfeldt and V. Gopalan, Appl. Phys. Lett. 92, 121915 (2008)

[70] R. Palai, R. S. Katiyar, H. Schmid, P. Tissot, S. J. Clark, J. Robertson, S. A. T. Redfern, G. Catalan, J. F. Scott, Phys. Rev. B **77**, 014110 (2008).

[71] S. A. T. Redfern, J. N. Walsh, S. M. Clark, G. Catalan, and J. F. Scott, arXiv:0901.3748v2. (2009).

[72] A. G. Gavriliuk, I. S. Lyubutin, and V. V. Struzhkin, JETP Lett. **86**, 532-536 (2007).

[73] U. Nagel, R. S. Fishman, T. Katuwal, H. Engelkamp, D. Talbayev, H. T. Yi, S.-W. Cheong, and T. Room, Phys. Rev. Lett. **110**, 257201 (2013).

[74] L. Pauling and S. B. Hendricks, J. Am. Chem. Soc. **47**, 781 (1925).

[75] F. J. Morin, Phys. Rev. **78**, 819 (1950).

[76] T. Kaneko and S. ABE, J. Phys. Soc. Japan **20**, 2001 (1965).

[77] C. G. Shull, W. A. Strauser, and E. O. Wollan, Phys. Rev. **83**, 333 (1951).

[78] I. Dzyaloshinsky, J. Phys. Chem. Solids **4**, 241 (1958).

[79] T. Moriya, Phys. Rev. **120**, 91 (1960).

[80] L. W. Finger and R. M. Hazen, J. Appl. Phys. **51**, 5362 (1980).

[81] Q. A. Pankhurst, C. E. Johnson, and M. F. Thomas, J. Phys. C **19**, 7081 (1986).

[82] R. D. Zysler, D. Fiorani, A. M. Testa, L. Suber, E. Agostinelli, and M. Godinho, Phys. Rev. B **68**, 212408 (2003).

[83] R. H. Kodama, J. Magn. Magn. Mater. **200**, 359 (1999).

[84] S. Azuma, M. Sato, Y. Fujimaki, S. Uchida, Y. Tanabe, and E. Hanamura, Phys. Rev. B **71**, 014429 (2005).

[85] T. R. Hart, S. B. Adams, and H. Temkin, In 3rd Int. Conf. Light Scatfeting, p. 259. Brazil (1975).

[86] M. Kenzelmann, A. B. Harris, A. Aharony, O. Entin-Wohlman, T. Yildirim, Q. Huang, S. Park, G. Lawes, C. Broholm, N. Rogado, R. J. Cava, K. H. Kim, G. Jorge and A. P. Ramirez, Phys. Rev. B **74**, 014429 (2006).

[87] E. E. Sauerbrei, R. Faggiani, and C. Calvo, Acta Crystallogr. B **29**, 2304 (1973).

[88] G. Lawes, A. B. Harris, T. Kimura, N. Rogado, R. J. Cava, A. Aharony, O. Entin-Wohlman, T. Yildrim, M. Kenzelmann, C. Broholm, and A. P. Ramirez, Magnetically Driven Ferroelectric Order in $Ni_3V_2O_8$, Phys. Rev. Lett. 95, 087205 (2005).

[89] J. F. Wang, M. Tokunaga, Z. Z. He, J. I. Yamaura, A. Matsuo, K. Kindo, Phys. Rev. B **84**, 220407(R) (2011).

[90] T. Lancaster, S. J. Blundell, P. J. Baker, D. Prabhakaran,W. Hayes, and F. L. Pratt, Phys. Rev. B **75**, 064427 (2007).

[91] R. C. Rai, J. Cao, S. Brown, J. L. Musfeldt, D. Kasinathan, D. J. Singh, G. Lawes, N. Rogado, R. J. Cava, and X. Wei, Phys. Rev. B **74**, 235101 (2006).

[92] W. Low, Phys. Rev. **109**, 247 (1958).

[93] G. Lawes, J. Nanophotonics **2**, 020306 (2008).

[94] H. L. Yakel, W. C. Koehler, E. F. Bertant and E. F. Forrat, Acta Cryst. **16**, 957 (1963).

[95] C. W. F. T. Pistorius and G. J. Kruger, J. inorg, nucl. Chem. **38**, 1471, (1976).

[96] D. G. Tomuta, S. Ramakrishnan, G. J. Nieuwenhuys, and J. A. Mydosh, J. Phys.: Condens. Matter **13**, 4543 (2001).

[97] S. Harikrishnan, S. Rößler, C. M. N. Kumar, H. L. Bhat, U. K. Rößler, S. Wirth, F. Steglich, and S. Elizabeth, J. Phys.: Condens. Matter **21**, 096002 (2009).

[98] J.-H. Lee, P. Murugavel, H. Ryu, D. Lee, J. Y. Jo, J. W. Kim, H. J. Kim, K. H. Kim, Y. Jo, M.-H. Jung, Y. H. Oh, Y.-W. Kim, J.-G. Yoon, J.-S. Chung, and T. W. Noh, Adv. Mater. (Weinheim, Ger.) **18**, 3125 (2006).

[99] B. B. Van Aken, T. T. M. Palstra, A. Filippetti, N. A. Spaldin, Nat. Mater. **3**, 164 (2004).

[100] T. Kimura, T. Goto, H. Shintani, K. Ishizaka, T. Arima, Y. Tokura, Nature **426**, 55 (2003).

[101] W. S. Choi, S. J. Moon, S. S. A. Seo, D. Lee, J. H. Lee, P. Murugavel, T. W. Noh, and Y. S. Lee, Phys. Rev. B **78**, 054440 (2008).

[102] F. Wooten, *Optical Properties of Solids* (Academic Press, New York, 1972).

[103] M. Tinkham, *in Far infrared properties of solids* (Plenum, New York, 1970).

[104] J. D. Jackson, *Classical Electrodynamics* (Wiley, New York, 1975).

[105] P. Chen, N. J. Podraza, X. S. Xu, A. Melville, E. Vlahos, V. Gopalan, R. Ramesh, D. G. Schlom, and J. L. Musfeldt, Appl. Phys. Lett. **96**, 131907 (2010).

[106] Ellipsometric spectra (in Δ, ψ) were extracted at four angles of incidence, Θ = 50 °, 60 °, 70 °, and 80 °, using a variable-angle dual rotating-compensator multichannel spectroscopic ellipsometer [107] over a spectral range from 0.75 to 5.15 eV. $\alpha(E)$ was also determined from spectroscopic ellipsometry analysis and compared with the complementary data obtained from optical transmittance. The dielectric function spectra ($\varepsilon = \varepsilon_1 + i\varepsilon_2$) and microstructural parameters (bulk layer thickness d_b, surface roughness thickness d_s) were extracted using a least squares regression analysis and an unweighted error function to fit the experimental ellipsometric spectra to an optical model consisting of a

semi-infinite orientation-dependent $YAlO_3$ substrate/bulk $BiFeO_3$ film/surface roughness/air ambient structure, where free parameters correspond to the bulk and surface roughness thicknesses of the $BiFeO_3$ film and a parameterization of the $BiFeO_3$ dielectric function.

[107] C. Chen, I. An, G. M. Ferreira, N. J. Podraza, J. A. Zapien, and R. W. Collins, Thin Solid Films **455**, 14 (2004).

[108] J. I. Pankove, *Optical Processes in Semiconductors* (Dover, New York, 1971).

[109] T. J. Park, G. C. Papaefthymiou, A. J. Viescas, A. R. Moodenbaugh, and S. S. Wong, Nano Lett. **7**, 766 (2007).

[110] D. Wolf, P. Keblinski, S. R. Philpot, J. Eggebrecht, J. Chem. Phys. **110**, 8254 (1999).

[111] P. Chen, Ö. Günaydın-Şen, W. J. Ren, Z. Qin, T. V. Brinzari, S. McGill, S. -W. Cheong, and J. L. Musfeldt, Phys. Rev. B **86**, 014407 (2012).

[112] E. J. Samuelsen, physica **43**, 353 (1969).

[113] R. P. Chaudhury, F. Yen, C. R. dela Cruz, B. Lorenz, Y. Q.Wang, Y. Y. Sun, and C. W. Chu, Phys. Rev. B **75**, 012407 (2007).

[114] P. Giannozzi, S. Baroni, N. Bonini, M. Calandra, R. Car, C. Cavazzoni, D. Ceresoli, G. L. Chiarotti, M. Cococcioni, I. Dabo et al., J. Phys. Condens. Matter **21**, 395502 (2009). http://www.quantum-espresso.org.

[115] D. Vanderbilt, Phys. Rev. B **41**, 7892 (1990).

[116] M. Cococcioni and S. de Gironcoli, Phys. Rev. B **71**, 035105 (2005).

[117] N. Marzari, D. Vanderbilt, A. De Vita, and M. C. Payne, Phys. Rev. Lett. **82**, 3296 (1999).

[118] H. Monkhorst and J. Pack, Phys. Rev. B **13**, 5188 (1976).

[119] P. A. Goddard, J. Singleton, P. Sengupta, R. D. McDonald, T. Lancaster, S. J. Blundell, F. L. Pratt, S. Cox, N. Harrison, J. L. Manson, and J. A. Schlueter, New J. Phys. **10**, 083025 (2008).

[120] P. Hermet, M. Goffinet, J. Kreisel, and Ph. Ghosez, Phys. Rev. B **75**, 220102(R) (2007).

[121] S. Kamba, D. Nuzhnyy, M. Savinov, J. Sebek, J. Petzelt, J. Prokleska, R. Haumont, and J. Kreisel, Phys. Rev. B **75**, 024403 (2007).

[122] The observed E(TO1) and E(TO2) mode frequencies are ∼25% lower than the calculated values whereas A_1(TO4) mode frequency is ∼12% higher which may due to the anharmonicity effects [120]. E(TO4) and A_1(TO2) are not identified in our experiment result which is the consequence of their strong overlap with E(TO3) and E(TO5) modes.

[123] Zone center and zone boundary k = (111) modes in the single cubic unit cell are equivalent to zone center modes in the 10-atom unit cell which is doubled along the [111] direction.

[124] F. Kubel, and H. Schmid, Acta Crystallogr. B **46**, 698 (1990).

[125] A. Bednarkiewicz, M. Maczka, W. Strek, J. Hanuza, and M. Karbowiak, Chem. Phys. Lett. **418**, 75 (2006).

[126] Relative intensity is defined as the fractional area of the whole spectrum needed to minimize the error bar associated with the nanoparticle size distribution and the experimental method.

[127] S. M. Selbach, T. Tybell, M.-A. Einarsrud, and T. Grande, Chem. Mater. **19**, 6478 (2007).

[128] M. T. Dove, Am. Mineral. **82**, 213 (1997).

[129] R. Haumont, J. Kreisel, P. Bouvier, and F. Hippert, Phys. Rev. B **73**, 132101 (2006).

[130] U. T. Höchli, and J. F. Scott, Phys. Rev. Lett. **26**, 1627 (1971).

[131] L. P. Kadanoff, W. Gütze, D. Hamblen, R. Hecht, E. A. S. Lewis, U.V. Palciauskas, M. Rayl, J. Swift, D. Aspnes, and J. Kane, Rev. Mod. Phys. **39**, 395 (1967).

[132] K. Ishikawa, K. Yoshikawa, and N. Okada, Phys. Rev. B **37**, 5852 (1988).

[133] S. Chattopadhyay, P. Ayyub, V. R. Palkar, M. Multani, Phys. ReV. B **52**, 13177 (1995).

[134] W. L. Zhong, B. Jiang, P. L. Zhang, J. M. Ma, H. M. Cheng, Z. H. Yang, and L. X. Li, J. Phys.: Condens. Matter **5**, 2619 (1993).

[135] K. Uchino, E. Sadanaga, and T. Hirose, J. Am. Ceram. Soc. **72**, 1555 (1989).

[136] G. Burns, and B. A. Scott, Phys. Rev. B **7**, 3088 (1973).

[137] J. Harada, J. D. Axe, and G. Shirane, Phys. Rev. B **4**, 155 (1973).

[138] P. A. Fleury, J. F. Scott, and J. M. Worlock, Phys. Rev. Lett. **21**, 16 (1968).

[139] G. Burns, and B. A. Scott, Phys. Rev. Lett. **25**, 167 (1970).

[140] R. E. Cohen, and H. Krakauer, Phys. Rev. B **42**, 6416 (1990).

[141] A. G. Gavriliuk, V.V. Struzhkin, I. S. Lyubutin, and I. A. Troyan, JETP Lett. **86**, 197 (2007).

[142] In a traditional oscillator fit, the center frequency and trends in the center frequency are always more reliable than the line width or intensity (and trends in these quantities). Partial superposition of features impacts the latter as well.

[143] H. M. Tütüncü and G. P. Srivastava, Phys. Rev. B, **78**, 235209 (2008).

[144] J. F. Ihlefeld, N. J. Podraza, Z. K. Liu, R. C. Rai, X. Xu, T. Heeg, Y. B. Chen, J. Li, R. W. Collins, J. L. Musfeldt, X. Q. Pan, J. Schubert, R. Ramesh and D. G. Schlom, Appl. Phys. Lett. **92**, 142908 (2008).

[145] R. V. Pisarev, A. S. Moskvin, A. M. Kalashnikova, and Th. Rasing, Phys. Rev. B **79**, 235128 (2009).

[146] M. B. Smith, K. Page, T. Siegrist, P. L. Redmond, E. C. Walter, R. Seshadri, L. E. Brus, M. L. Steigerwald, *J. Am. Chem. Soc.* **130**, 6955 (2008).

[147] F. Gao, Y. Yuan, K. F. Wang, X. Y. Chen, F. Chen, and J.-M. Liu, Appl. Phys. Lett. **89**, 102506 (2006).

[148] A. D. Yoffe, Adv. Phys **42**, 173 (1993).

[149] Penetration depth is $2/\alpha$, where α is absorption coefficient. $\alpha \simeq 3 \cdot 10^5 cm^{-1}$ for $BiFeO_3$, so the maximum penetration depth is $\sim$67 nm.

[150] T. Choi, S. Lee, Y. J. Choi, V. Kiryukhin, and S.-W. Cheong, Science **324**, 63 (2009).

[151] S. Y. Yang, L. W. Martin, S. J. Byrnes, T. E. Conry, S. R. Basu, D. Paran, L. Teichertz, J. Ihlefeld, C. Adamo, A. Melville, Y. -H. Chu, C. -H. Yang, J. L.

Musfeldt, D. G. Schlom, J. W. Ager III, and R. Ramesh, Appl. Phys. Lett. **95**, 062909 (2009).

[152] R. Balda, M. Sanz, A. Mendioroz, J. Fernández, L. S. Griscom, and J.-L. Adam, Phys. Rev. B **64**, 144101 (2001).

[153] L. L. Lohr, Coord. Chem. Rev. **8**, 241 (1972).

[154] Since Nd^{3+} replaces the Bi^{3+} centers in these solid solutions, the local structure for low levels of rare earth incorporation is octahedral [80]. At very high subsitutition levels, the local field is expected to approach the 8-fold square antiprismatic environment of the $NdFeO_3$ end member.

[155] X. S. Xu, T. V. Brinzari, S. McGill, H. D. Zhou, C. R. Wiebe, and J. L. Musfeldt, Phys. Rev. Lett. **103**, 267402 (2009).

[156] G. L. Yuan, S. W. Or, J. M. Liu, and Z. G. Liu, Appl. Phys. Lett. **89**, 052905 (2006).

[157] D. D. Sell, R. L. Greene, and R. M. White, Phys. Rev. **158**, 489 (1967).

[158] They do, however have a signature in second harmonic generation spectra.

[159] Y. Tanabe, T. Moriya, and S. Sugano, Phys. Rev. Lett. **15**, 1023 (1965).

[160] This is a challenge for optical properties work as well as for bulk magnetization measurements, since rare earth excitations can interfere with the interpretation of the latter. [155]

[161] J. Bartolome, E. Palacios, M. D. Kuzmin, F.Bartolome, I. Sosnowska, and R. Przenios, Phys. Rev. B **55**, 1143 (1997).

[162] Yu. F. Popov, A. K. Zvezdin, G. P. Vorob'ev, A. M. Kadomtseva, V. A. Murashev, and D. N. Rakov, JETP Lett. **57**, 69 (1993).

[163] Magnetic anisotropy is responsible for easy and hard magnetization axes in $BiFeO_3$, and as a result, the transition field is different when magnetic field is applied in different orientation [64, 162].

[164] M. K. Singh, R. S. Katiyar, and J. F. Scott, J. Phys. Condens. Matter **20**, 4 (2008).

[165] J. F. Scott, M. K. Singh, and R. S. Katiyar, J. Phys. Condens. Matter **20**, 322203 (2008).

[166] B. Ruette, S. Zvyagin, A. P. Pyatakov, A. Bush, J. F. Li, V. I. Belotelov, A. K. Zvezdin, and D. Viehland, Phys. Rev. B **69**, 064114 (2004).

[167] I. Sosnowska, W. Schäfer, W. Kockelmann, K. H. Andersen, and I. O. Troyanchuk, Appl. Phys. A: Mater. Sci. Process. **74**, s1040 (2002).

[168] $B_{C,ave}$ curve can be fitted with exponential decay function as: $21.2e^{-17.3x}$, indicating the critical field vanishes rapidly with chemical substitution.

[169] J. Lu, A. Günther, F. Schrettle, F. Mayr, S. Krohns, P. Lunkenheimer, A. Pimenov, V. D. Travkin, A. A. Mukhin, A. Loidl, Eur. Phys. J. B **75**, 451 (2010).

[170] J. C. Phillips, Phys. Rev. **104**, 1263 (1956).

[171] R. E. Mills, R. P. Kenan, and F. J. Milford, Phys. Rev. **145**, 704 (1966).

[172] This assignment relies on the similar intensity of excitons in α and σ polarizations and magnetic field results.

[173] A. I. Galuza, A. B. Beznosov, and V. V. Eremenko, Low Temp. Phys. **24**, 726 (1998).

[174] K. Aoyagi, K. Tsushima, and S. Sugano, Solid State Commun. **7**, 229 (1969).

[175] J. P. van der Ziel, Phys. Rev. Lett. **18**, 237 (1967).

[176] The intensity of MS1 increases as that of M1σ when rotating the polarizer from the π to σ direction.

[177] J. W. Halley and I. Silvera, Phys. Rev. Lett. **15**, 654 (1965).

[178] M. Lax and J. J. Hopfield, Phys. Rev. **124**, 115 (1961).

[179] J. W. Allen, R. M. Macfarlane, and R. L. White, Phys. Rev. **179**, 523 (1969).

[180] Our data reveals that temperature and magnetic field effects in α-Fe_2O_3 are quite different. The color change through the temperature-driven spin-flop transition [54] is entangled with phonon-assisted trends that grow with temperature. Moreover, the signature of the spin flop transition is small compared with the rising phonon-assisted background, and it has an opposite trend, making changes difficult to discern. Finally, exciton and magnon sideband peaks can not be observed above 150 K. As we show here, these peaks are incredibly sensitive to variations in magnetic order. This makes optical properties work through the field-driven spin flop transition the preferred strategy for investigating ordering-induced color change and mechanistic issues.

[181] C. V. Stager, J. Appl. Phys. **34**, 1232 (1963).

[182] An additional peak should split from E2α but is not observed, probably because it is superimposed with E1α.

[183] C. Hermann, Z. Kristallogr. **89**, 32 (1934).

[184] Ni(c) has $C2h$ site symmetry, whereas distortion breaks the inversion center on Ni(s) reducing it to $C2$. This symmetry breaking activates the formally Laporte

forbidden excitations. The weak ${}^3A_{2g} \rightarrow {}^1E_g$ shoulder is also spin forbidden but becomes allowed due to spin-orbit and exchange interactions that hybridize states.

[185] J. Laverock, B. Chen, A. R. H. Preston, K. E. Smith, N. R. Wilson, G. Balakrishnan, P.-A. Glas, and J.-H. Guo, Phys. Rev. B **87**, 125 (2013).

[186] We determined the optical gap using the leading edge of the charge transfer excitation, therefore, the absolute gap value may be somewhat underestimated. The field-induced effect will not be impacted by gap determination.

[187] An insufficient integration range in Kramers-Kronig analysis may be responsible for the previously underestimated optical band gap

[188] A. Dixit, P. Chen, J. L. Musfeldt, G. Lawes (Unpublished).

[189] D. Qian, L. Wray, D. Hsieh, D. Wu, J. L. Luo, N. L. Wang, A. Kuprin, A. Fedorov, R. J. Cava, L. Viciu, and M. Z. Hasan, Phys. Rev. Lett. **96**, 046407 (2006).

[190] The fitting constants are obviously different above and below the 37 T critical field.

[191] The fit shows that magnetoelectric coupling is also proportional to magnetization energy.

[192] The response broadens with temperature over the full field range as expected.

[193] G. Racah, Physical Review **62**, 438, (1942).

[194] L. F. Mattheiss, Phys. Rev. B **6**, 306 (1972).

[195] Both σ-GGA and σ-GGA+U approaches give quite similar charge density, density of states and band structure results. Hubbard U plays its role by enlarging the band gap.

[196] The charge densities difference around Ni(s) doesn't show a precise, characteristic d orbital shape due to slight octahedral distortion.

[197] Ö. Ğunaydin-Sen, P. Chen, J. Fosso-Tande, T. L. Allen, J. Cherian, T. Tokumoto, P. M. Lahti, S. McGill, R. J. Harrison, and J. L. Musfeldt, J. Chem. Phys. **138**, 204716 (2013).

[198] P. Kharel, C. Sudakar, A. Dixit, A. B. Harris, R. Naik and G. Lawes, Europhys. Lett. **86**, 17007 (2009).

[199] P. Chen, B. S. Holinsworth, K. R. ONeal, N. Lee, C. V. Topping, S. McGill, S. W. Cheong, J. Singleton, E. S. Choi, and J. L. Musfeldt, unpublished.

[200] A. Walsh, J. L. F. Da Silva, S.-H. Wei, C. Korber, A. Klein, L. F. J. Piper, A. DeMasi, K. E. Smith, G. Panaccione, P. Torelli, D. J. Payne, A. Bourlange, and R. G. Egdell, Phys. Rev. Lett. **100**, 167402 (2008).

[201] J. D. Axe and G. H. Dieke, J. Chem. Phys. **37**, 2364 (1962).

[202] M. Divis, J. Holsa, M. Lastusaari, A. P. Litvinchuk, and V. Nekvasil, J. Alloys Compd. **451**, 662 (2008).

[203] X. S. Xu, M. Angst, T. V. Brinzari, R. P. Hermann, J. L. Musfeldt, A. D. Christianson, D. Mandrus, B. C. Sales, S. McGill, J.-W. Kim, and Z. Islam, Phys. Rev. Lett. **101**, 227602 (2008).

[204] W. F. J. Fontijn *et al.*, J. Appl. Phys. **85**, 5100 (1999).

[205] P. Chen, B. S. Holinsworth, K. R. O'Neal, T. V. Brinzari, N. Rogado, Y. Q. Wang, S. McGill, R. J. Cava, B. Lorenz and J. L. Musfeldt, submitted.

[206] R. Loudon, Adv. Phys. **17**, 243 (1968).

[207] M. Blanchard, M. Lazzeri, F. Mauri, E. Balan, American Mineralogist **93**, 1019 (2008).

[208] J. Zaanen, G. A. Sawatzky, and J. W. Allen, Phys. Rev. Lett. **55**, 418 (1985).

Appendix

Appendix A

Supplemental Material for α-Fe_2O_3

A.1 Symmetry analysis of excitons

Within the single ion approximation, the site group controls the symmetry properties of excitons [206]. In α-Fe_2O_3, the Fe^{3+} centers occupy positions with C_3 site symmetry. The zone center excitons therefore have A, A + C_1 or A + C_2 symmetry. This is due to the combined effects of spin-orbit coupling, exchange interaction, and the trigonal field. Next we need to consider what happens to these features under the constraints of the crystal space group. Under the $R\bar{3}c$ space group, excitons with A symmetry transform into $\Gamma_1^+ + \Gamma_1^- + \Gamma_2^+ + \Gamma_2^-$ levels, and excitons with C_1 and C_2 symmetry transform as $\Gamma_3^+ + \Gamma_3^-$. These transformations are summarized in Table A.1.1. Based on the frequency shift and polarized results, the features centered at 9930, 10104 and 10289 cm^{-1} (Fig. 5.1b) have irregular shape and are possibly due to the coupling of E1 with phonons [207]. The excitations at 10645 cm^{-1}, 10787 and 10990 cm^{-1} are the phonon sideband of MS1 whereas the feature at 11100 cm^{-1} is probably two magnons coupled with M1σ (Fig. 1b of the main text). The possible exciton and magnon symmetries in the Brillouin zone are shown in the Fig. A.1.1 [206].

Applied magnetic field drives the spin flop transition which gives rise to new mag-

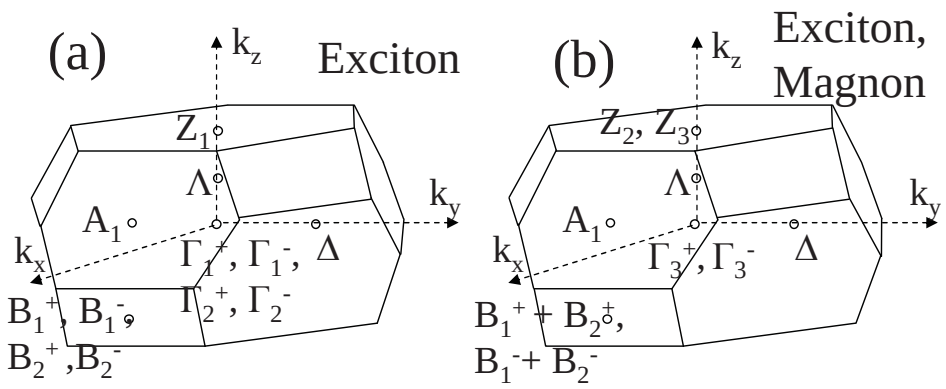

Figure A.1.1: (a, b) Irreducible representations of the exciton and magnon in the Brillouin zone of α-Fe_2O_3. (after Ref. [14])

netic order. Conserved spin collinearity, a result deduced from the observation of increased magnon sideband intensity in magnetic field, has two important consequences. First, the high field phase should display the same translation group as the zero field phase. Second, certain symmetry operations, specifically inversion center and $C2$ rotational axis, must survive. These findings are consistent with Dzyaloshinsky's early work [78]. Subgroup analysis reveals several high field symmetry candidates. These include $P1$, $P\bar{1}$, $C2$, Cc, $C2/c$, $R3$, $R\bar{3}$, $R32$, and $R3c$. Only the $C2/c$ monoclinic structure contains the necessary inversion center and $C2$ rotational axis. We conclude that the field-induced magnetic ordering in α-Fe_2O_3 is monoclinic with $C2/c$ symmetry - at least to first order.

We know, however, that Dzyaloshinskii–Moriya interactions lift the inversion center [78, 79]. Experimental evidence for this formal symmetry breaking is the very slight

Table A.1.1: Relation of site group representations to exciton symmetries.

Single-ion transition	C_3 transition operator symmetry	$R\bar{3}c$ exciton symmetry
Between like states	A	$\Gamma_1^+ + \Gamma_1^- + \Gamma_2^+ + \Gamma_2^-$
Between unlike states	C_1	$\Gamma_3^+ + \Gamma_3^-$
	C_2	$\Gamma_3^+ + \Gamma_3^-$

spin canting in the high field phase. This canting is on the order of 10^{-4} degrees and is schematically diagrammed in Fig. 5.4(b). The formal symmetry breaking and associated loss of the inversion center requires that we revise the first-order estimate of magnetic symmetry discussed in the previous paragraph. Although the inversion center is lost due to spin canting, the $C2$ operation survives. Among the subgroup candidates, only the $C2$ monoclinic structure contains the necessary $C2$ rotational axis. We therefore conclude that the formal symmetry of the field-induced ordered phase of α-Fe_2O_3 is $C2$. As expected, inclusion of the higher order (spin canting) effect lowers the symmetry from $C2/c \rightarrow C2$. Above the critical field, all singly degenerate symmetry excitons in the $R\bar{3}c$ structure survive. Only the doubly degenerate (E symmetry) excitons split into two singlets. This symmetry breaking gives rise to the new exciton pattern in the high field, as shown in the spectroscopic data and in the correlation Table A.1.2.

Table A.1.2: Correlation table for the Γ point of $R\bar{3}c$, $C2/c$ and $C2$.

$R\bar{3}c$	Γ_1^+	Γ_2^+	Γ_3^+	Γ_1^-	Γ_2^-	Γ_3^-
$C2/c$	Γ_1^+	Γ_2^+	$\Gamma_1^+ + \Gamma_2^+$	Γ_1^-	Γ_2^-	$\Gamma_1^- + \Gamma_2^-$
$C2$	Γ_1	Γ_2	$\Gamma_1 + \Gamma_2$	Γ_1	Γ_2	$\Gamma_1 + \Gamma_2$

A.2 Symmetry analysis of the magnon sideband

Using group theory analysis, we can also determine the selection rules of the magnon sideband, and these predictions can be tested against the observed optical spectra. To analyze the magnon sideband symmetry across the Brillioun zone, we used the selection rules of Lax *et al.* [178] and obtained the following irreducible representations:
$\Gamma_1^+ \times \Gamma_3^+ = \Gamma_2^+ \times \Gamma_3^+ = \Gamma_1^- \times \Gamma_3^- = \Gamma_2^- \times \Gamma_3^- = \Gamma_3^+$

$$\Gamma_1^+ \times \Gamma_3^- = \Gamma_2^+ \times \Gamma_3^- = \Gamma_1^- \times \Gamma_3^+ = \Gamma_2^- \times \Gamma_3^+ = \Gamma_3^-$$

$$Z_1 \times Z_2 = Z_1 \times Z_3 = \Gamma_3^+ + \Gamma_3^-$$

$$A_1 \times A_1 = \Gamma_1^+ + \Gamma_1^- + \Gamma_2^+ + \Gamma_2^- + 2\Gamma_3^+ + 2\Gamma_3^-$$

$$B_1^+ \times B_1^+ = B_1^- \times B_1^- = B_2^+ \times B_2^+ = B_2^- \times B_2^- = \Gamma_1^+ + \Gamma_3^+$$

$$B_1^+ \times B_1^- = B_2^+ \times B_2^- = \Gamma_1^- + \Gamma_3^-$$

$$B_1^+ \times B_2^+ = B_1^- \times B_2^- = \Gamma_2^+ + \Gamma_3^+$$

$$B_1^+ \times B_2^- = B_1^- \times B_2^+ = \Gamma_2^- + \Gamma_3^-.$$

For electric dipole process, we find that zone center and all zone boundary points are allowed in the σ-polarization (Γ_3^-), whereas only A and B points contribute to the π-polarization (Γ_2^-). These results indicate that the absorption coefficient of the σ-polarized magnon sideband can be expressed as weighted joint density of states (exciton + magnon), whereas the π-polarized sideband is $\overrightarrow{k}$ dependent which results in a different shape, as shown in Fig. 5.1b. Magnon sideband formation obviously relies on strong coupling between the exciton and magnon, revealing the interplay between charge and magnetism in α-Fe_2O_3.

A.3 Density of states calculation

The magnon sideband density of states $\rho_{e-m}(\omega)$ is defined as [51]

$$\rho_{e-m}(\omega) = \sum_{\overrightarrow{k},u,v} \delta[\omega - \omega_e(-\overrightarrow{k}, u) - \omega_m(\overrightarrow{k}, v)], \tag{A.3.1}$$

where ω_e is the exciton frequency, ω_m is the magnon frequency, δ is Dirac delta function, and u and v represent exciton and magnon branches, respectively. In order to compare the magnon sideband features in the spectra with predictions from this model, we calculated ρ_{e-m} using the magnon dispersion provided by Samuelsen [112]. This involved

2×10^7 sampling points evenly distributed throughout the Brillouin zone. As an approximation, we neglected the exciton dispersion. To determine the optimal exchange interaction parameters, we fit $\rho_{e-m}(\omega)$ to the σ-polarized spectrum by the least squares method: $S = \sum_{i=1}^{n}(\alpha_i(\omega) - f_i)^2$, where $\alpha_i(\omega)$ is the measured absorption coefficient, and f_i is the calculated density of states. We minimized S with 0.1 K step iterations for each interaction constant. A comparison of the calculated results and measured spectra at 0 T and 35 T is shown in Fig. A.3.1. The interaction constants obtained from fitting the spectrum at 0 T are in reasonable agreement with the exchange constants from neutron scattering measurements [28], which provides a useful consistency check on this multi-variable optimization process. These same exchange constants were used to calculate the magnon density of states (inset, Fig 5.1c). The results agree very well with the measured absorption spectrum and explain the directionally-dependent magnon sideband shape (Fig 5.1c).

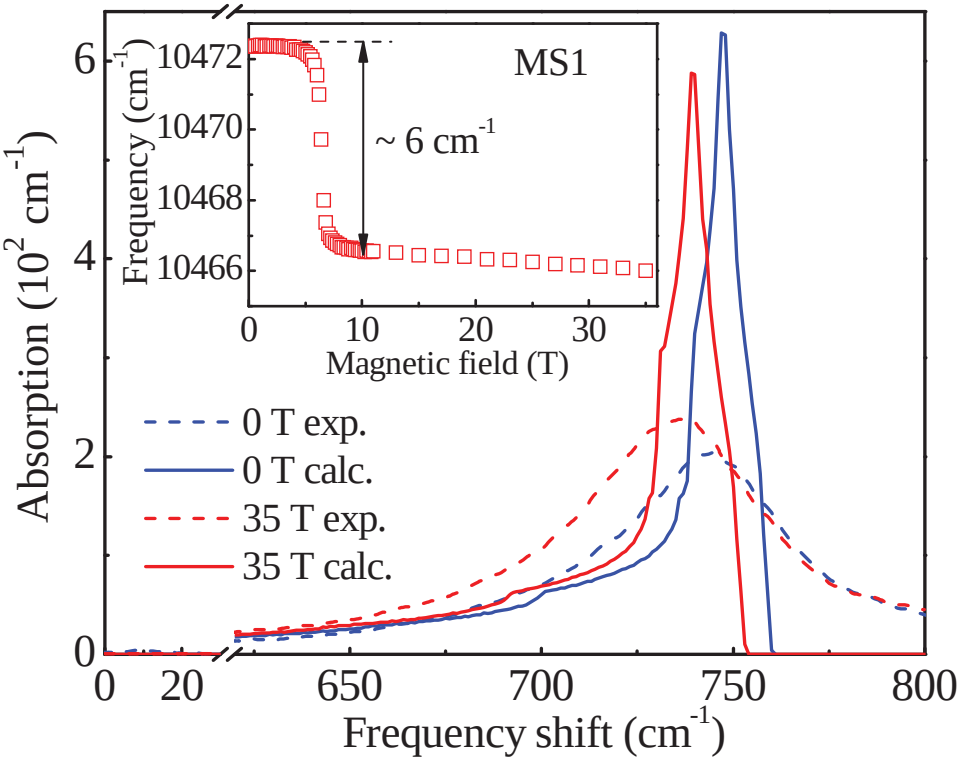

Figure A.3.1: (Color online) Comparison of the σ-polarized magnon sideband absorption spectra at 0 and 35 T (the *d*-*d* excitation background has been subtracted) with the calculated density of states. Interaction constants J_1 = 7.6 K, J_2 = 2.0 K, J_3 = -27.7 K, and J_4 = -22.2 K are used for fitting the spectrum at 0 T, and J_1 = 8.7 K, J_2 = 2.2 K, J_3 = -27.3 K, and J_4 = -22.1 K fit the spectrum best at 35 T. Inset: The magnon sideband position red shifts with magnetic field. (after Ref. [14])

Appendix B

Supplemental Material for $Ni_3V_2O_8$

B.1 Density of states (DOSs)

We calculated the density of states in antiferromagnetic and ferromagnetic (FM) spin states, as shown in Fig. B.0.1. The overall DOSs in the AFM state are similar as those obtained from the LDA+U method for U=5 eV [91]. They are also in good agreement with x-ray scattering measurements illustrating that both Ni and V d states are buried in the O p DOSs [185]. In the valence band, the overlapping DOSs indicate bonding between the Ni 3d and O 2p states [185]. There is little interaction between the V and O orbitals. On approach to the band edge, O 2p states dominate with minor contributions from Ni d_{xy}, $d_{3z^2-r^2}$ states. This result suggests that the band gap in $Ni_3V_2O_8$ is mainly charge-transfer type with partial Mott-Hubbard character [91, 185, 208]. In the conduction band, the V 3d states join the hybridization. When the spins are aligned along one direction and magnetic structure becomes FM, the energy of the minority total density of states shifts to lower energy. Moreover, for the total DOSs in the majority channel, the amount of those on top of the valence band is reduced, and it shifts to higher energy in the conduction band. As a consequence, the band gap increases slightly in the FM state, consistent with our experimental results.

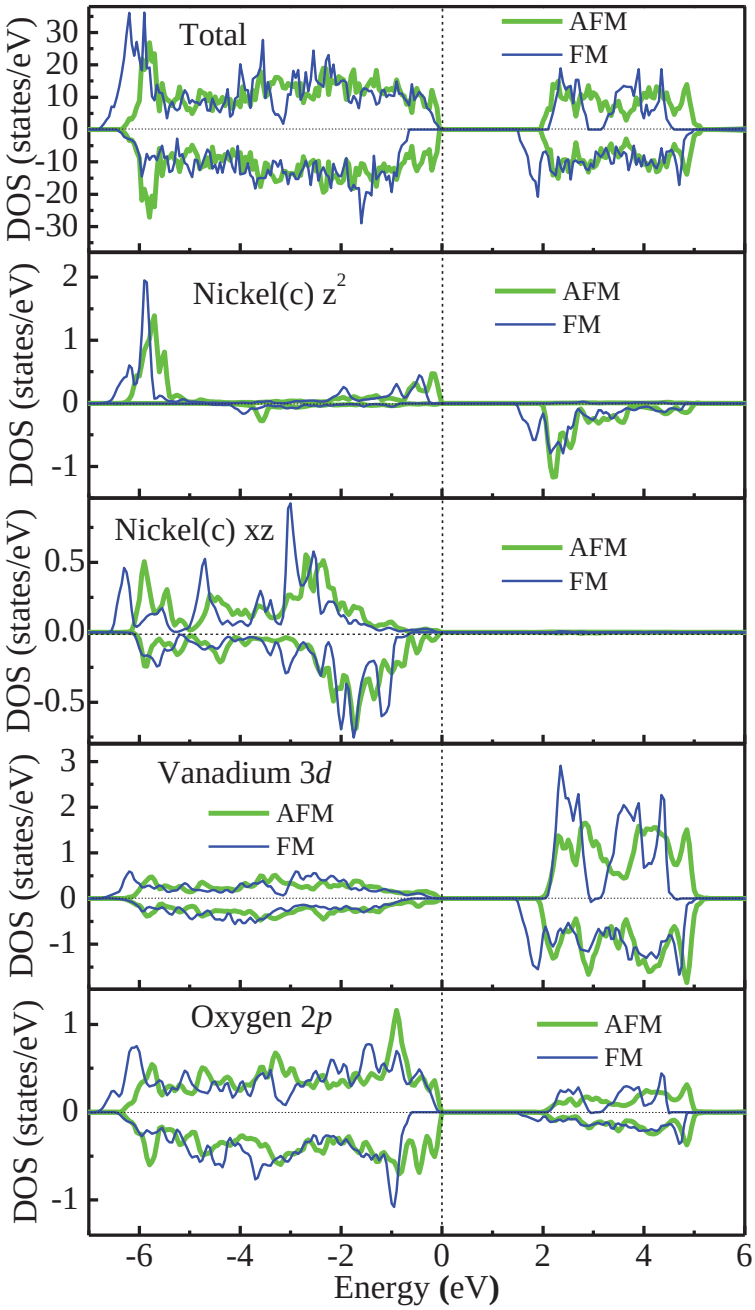

Figure B.0.1: Total and orbital-resolved densities of states (DOSs) of Ni(c), V and O ions for $Ni_3V_2O_8$ in AFM and FM spin states calculated within σ-GGA+U (Us are 4.0 and 4.2 eV for Ni(c) and Ni(s) ions, respectively). Majority and minority states are up- and down-going, respectively.

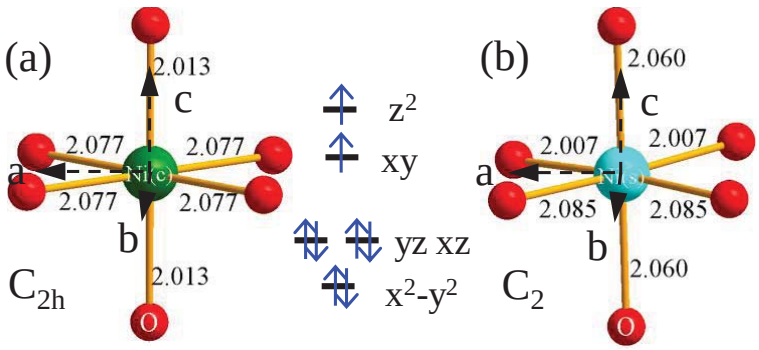

Figure B.1.1: The local structure of the (a) cross-tie NiO_6 and (b) distorted spine NiO_6 octahedron [87]. The local coordinate system is also indicated. The central diagram illustrates the electron configuration of Ni^{2+} (d^8).

B.2 Spine and cross-tie Ni^{2+} centers

Ni(c) has $C2h$ site symmetry, whereas distortion formally breaks the inversion center on Ni(s), reducing it to $C2$, as shown in Fig. B.1.1. The charge density is sensitive to these local environments. Because of the hybridized orbitals around the Ni(s) centers, the charge density difference around Ni(s) in the two spin states doesn't show the characteristic shape of a d orbital. Those around Ni(c) centers are typical. In contrast, the partial DOSs of Ni(s) are very similar to those of Ni(c), foreshadowing the similar optical response of these two different Ni^{2+} centers [Fig. 6.2]. Resonant inelastic x-ray scattering experiments and crystal field multiplet theory also show that the crystal field around the crosstie and spine sites is similar [185].

Vita

Peng Chen was born in Yichang City, Hubei Province, China. He attended University of Science and Technology of China in Anhui between 1997 and 2005, where he received B.S. degrees majoring in Chemistry and Computer Science, and M.S. in Software Engineering. After four years of working in the Keenmicro Financial System Inc. and KangPei Medical Biotechnology (Shanghai) Co. Ltd., Chen joined the research group of Dr. Janice L. Musfeldt in the spring 2009 pursuing his Ph.D. degree in the University of Tennessee. His research focuses on the spectroscopic investigations of complex oxides. Peng Chen received a Doctor of Philosophy Degree in Chemistry from the University of Tennessee in Fall 2013.